Marta Alexandra Fernandes Silva

Licenciatura em Biotecnologia

Characterization of novel heme-containing sensor proteins from *Geobacter sulfurreducens*

Dissertação para obtenção do Grau de Doutor em
Bioquímica, ramo Biofísica

Orientador: Prof. Carlos A. Salgueiro, Professor Auxiliar,
Faculdade de Ciências e Tecnologia, Universidade Nova de Lisboa

Presidente:	Prof. Doutor Jorge Orestes Lasbarrères Cerdeira
Arguentes:	Doutor Douglas Vinson Laurents
	Doutor Filipe dos Santos Folgosa
Vogais:	Doutor Vítor Manuel Bordona de Sousa Paixão
	Prof. Doutor Carlos Alberto Salgueiro

FACULDADE DE CIÊNCIAS E TECNOLOGIA
UNIVERSIDADE NOVA DE LISBOA

Outubro 2014

Universidade Nova de Lisboa

Marta Alexandra Fernandes Silva

Licenciatura em Biotecnologia

Characterization of novel heme-containing sensor proteins from *Geobacter sulfurreducens*

Dissertação para obtenção do Grau de Doutor em
Bioquímica, ramo Biofísica

Orientador: Prof. Carlos A. Salgueiro, Professor Auxiliar,
Faculdade de Ciências e Tecnologia, Universidade Nova de Lisboa

FACULDADE DE CIÊNCIAS E TECNOLOGIA
UNIVERSIDADE NOVA DE LISBOA

Outubro 2014

Characterization of novel heme-containing chemotaxis sensor proteins from *Geobacter sulfurreducens*

AGRADECIMENTOS

Apesar das dificuldades inerentes a todos os trabalhos científicos, sem o apoio de diversas pessoas este teria sido impraticável. Nesse sentido não posso deixar de agradecer à equipa que me acompanhou durante este percurso que metaforicamente irei comparar a uma maratona.

Em primeiro lugar, quero agradecer ao meu orientador Prof. Doutor Carlos Salgueiro por ter confiado nas minhas capacidades numa altura em que ninguém acreditou. Correu incansável e continuamente ao meu lado desde o início e orientou-me da melhor maneira que encontrou. Agradeço a sua dedicação, disponibilidade, amizade e por vezes paciência nas inúmeras e infindáveis discussões que assumo por vezes serem exasperantes. Na minha opinião, o resultado final compensou em larga escala as adversidades. Aprendi a correr mesmo quando o corpo e a mente se encontram debilitados.

Quero agradecer à Prof. Doutora Teresa Catarino, por me ter recebido por diversas vezes no seu laboratório no Instituto de Tecnologia Quimica e Biológica (ITQB), por me ter orientado e iniciado nos estudos cinéticos e por ter cuidado da logística necessária durante a minha estadia no ITQB. A sua simpatia, as suas sugestões e debates científicos foram fundamentais para o desenvolvimento deste trabalho. Obrigado pelo tempo e conhecimento que partilhou comigo.

Agradeço também ao Prof. Doutor David L. Turner pelo seu contributo e confiança no estudos termodinâmicos e cinéticos.

Ao Doutor Cláudio M. Gomes agradeço a orientação, ajuda e transmissão de conhecimento no “folding” das proteínas. O seu dinamismo e confiança são admiráveis e entusiasmantes. Á Tânia Lucas, agradeço a disponibilidade e acompanhamento nesta maratona. A excelente forma que ambos apresentam é inspiradora.

Agradeço à Prof. Doutora Isabel Couto não só pela enorme ajuda científica, mas principalmente pela amizade, disponibilidade e por todos os bons conselhos. A iniciação científica que me proporcionou foi uma excepcional mais valia para me manter nesta corrida.

Agradeço à Prof. Doutora Marianne Schiffer, ao Doutor P. Raj Pokkuluri e ao Doutor. Yuri Y. Londer do Argonne National Laboratory pela disponibilização das proteínas e dos plasmídeos e às discussões científicas.

Agradeço à Prof. Doutora Marta Bruix, por me ter recebido no seu laboratório no Instituto de Química-Física “Rocasolano”, Consejo Superior de Investigaciones Científicas em Madrid e por ter estimulado o gosto pelo mundo do RMN. A sua sabedoria e entusiasmo são contagiantes e motivadores.

Agredeço a todos os que passaram pelo Laboratório 611 e que tornaram esta corrida dinâmica, divertida e principalmente com partilhas preciosas e inestimáveis. Agradeço em especial à Raquel Valente e ao Tiago Pereira por terem enfrentado comigo, sempre com entusiamo e dedicação, as adversidades na obtenção de dados. Agradeço à Ana Fernandes, pela ajuda nos crescimentos e purificações, à Leonor Morgado por me iniciar no trabalho anaeróbio e RMN, à Joana Dantas pela disponibilidade e apoio nas inúmeras “situações” que precisaram de resolução e ao Filipe Folgosa pelos valiosos conselhos e praticabilidade com que ultrapassa os problemas. Ao Eduardo Calçada e à Telma Santos agradeço o contributo em alguns apontamentos gráficos e à boa disposição e positivismo que os rodeia. Sem vocês seria tudo mais complicado.

Agradeço aos colegas do Departamento de Química, que me acompanharam nestes anos, que contribuíram de alguma forma na realização deste trabalho, quer na utilização de um equipamento ou no empréstimo de um reagente, ou apenas pelas discussões de corredor.

Quero deixar um agradecimento especial para a minha familia, racional e irracional. Aos meus Pais e Irmão, agradeço o carinho incondicional, preocupação e amparo. Com eles aprendi a andar, a correr, a permanecer teimosamente no meu caminho até chegar à meta proposta.

Ao Pedro e à Alexandra, obrigada por estarem sempre comigo. Mesmo quando o caminho se torna escuro vocês têm a capacidade de o iluminar. São a razão pela qual não desisto mesmo que as lesões sejam mais que as forças.

Agradeço à Rede Nacional de RMN financiada pela Fundação para a Ciência e Tecnologia através do Projecto "NMR-Net Centro Nacional de Ressonância Magnética Nuclear: Desde a Estrutura e Dinâmica Moleculares à Função Proteica, Fisiológica Celular e Metabolómica" (RECI/BBB-BQB/0230/2012), pelo acesso aos espectrómetros de RMN. Agradeço a disponibilidade do Prof. Doutor Eurico Cabrita e do Aldino Viegas, durante a utilização dos equipamentos.

Por último, gostaria de agradecer à Fundação para a Ciência e a Tecnologia pelo financiamento através da Bolsa de Doutoramento SFRH/BD/61952/2009, do Projecto PTDC/BBB-BEP/0753/2012 atribuído ao Prof. Doutor Carlos Salgueiro e ao Projecto Estratégico PEst-C/EQB/LA0006/2013 concedido ao REQUIMTE Laboratório Associado, sem os quais a execução deste trabalho não seria possível.

ABSTRACT

The focus of this Thesis was the study of the sensor domains of two heme-containing methyl-accepting chemotaxis proteins (MCP) from *Geobacter sulfurreducens:* GSU0582 and GSU0935. These domains contain one *c*-type heme, form swapped dimers with a PAS-like fold and are the first examples of a new class of heme sensors.

NMR spectroscopy was used to assign the heme and polypeptide signals in both sensors, as a first step to probe conformational changes in the vicinity of the hemes. However, the presence of two conformations in solution impaired the confident assignment of the polypeptide signals.

To understand how conformational changes and swapped dimerization mechanism can effectively modulate the function of the two sensor domains and their signal transduction process, the sensor domains folding and stability were studied by circular dichroism and UV-visible spectroscopy. The results showed differences in the thermodynamic stability of the sensors, with GSU0582 displaying higher structural stability. These studies also demonstrated that the heme moiety undergoes conformational changes matching those occurring at the global protein structure and that the content of intrinsically disordered segments within these proteins (25% for GSU0935; 13% for GSU0582) correlates with the stability differences observed.

The thermodynamic and kinetic properties of the sensor domains were determined at different pH and ionic strength by visible spectroscopy and stopped-flow techniques. Despite the remarkably similar spectroscopic and structural features of the two sensor domains, the results showed that their properties are quite distinct. Sensor domain GSU0935 displayed more negative reduction potentials and smaller reduction rate constants, which were more affected by pH and ionic strength. The available structures were used to rationalize these differences.

Overall, the results described in this Thesis indicate that the two *G. sulfurreducens* MCP sensor domains are designed to function in different working potential ranges, allowing this bacterium to trigger an adequate cellular response in distinct anoxic subsurface environments.

Keywords: *Geobacter sulfurreducens*, methyl-accepting chemotaxis protein, *c*-type sensor domain, signal transduction, NMR, circular dichroism, folding, stopped-flow kinetics.

RESUMO

O trabalho desenvolvido no âmbito desta Tese incide no estudo dos domínios sensoriais de duas proteínas quimiotáxicas metil-aceitadoras (MCP) de *Geobacter sulfurreducens*: GSU0582 e GSU0935. Estes domínios contêm um hemo do tipo *c*, formam dímeros invertidos com um enrolamento do tipo PAS e são os primeiros exemplos de uma nova classe de sensores hémicos.

A espectroscopia de RMN foi usada para a atribuição dos sinais dos substituintes hémicos e das cadeias polipeptídicas de ambos os sensores como primeiro passo para estudar as alterações conformacionais na vizinhança do hemo. No entanto, a presença de duas conformações em solução prejudicou a atribuição dos sinais das cadeias polipeptídicas.

De forma a compreender como as alterações conformacionais e o mecanismo de dimerização podem regular a função destes domínios sensoriais, a sua estabilidade foi monitorizada através de espectroscopia de dicroísmo circular e UV-visível. Foi possível detectar diferenças na estabilidade dos dois sensores, sendo GSU0582 aquele que exibe uma maior estabilidade estrutural. Estes estudos demonstraram também que a região do hemo sofre alterações conformacionais consistentes com as que ocorrem na estrutura global da proteína e que o seu teor intrínseco de segmentos desordenados (25% para GSU0935; 13% para GSU0582) se correlaciona com as diferenças observadas ao nível da estabilidade.

As propriedades termodinâmicas e cinéticas dos domínios sensoriais foram determinadas a diferentes valores de pH e força iónica utilizando espectroscopia de visível e técnicas de cinética de fluxo interrompido. Apesar do elevado grau de semelhança a nível espectroscópico e estrutural dos dois domínios sensoriais, os resultados obtidos indicam que as suas propriedades são bastante distintas. O domínio sensorial GSU0935 possui potenciais de redução mais negativos e constantes de redução menores, que são mais afectados pelo pH e força iónica. As estruturas disponíveis foram usadas para racionalizar estas diferenças.

Em suma, os resultados descritos neste Tese indicam que os dois domínios sensoriais de *G. sulfurreducens* estudados são capazes de funcionar em diferentes gamas de potencial redox permitindo a esta bactéria desencadear uma resposta celular adequada em diferentes ambientes anóxicos.

Palavras-chave: *Geobacter sulfurreducens*, proteína quimiotáxica metil-aceitadora, domínio sensorial com hemos do tipo *c*, transducção de sinal, RMN, dicroísmo circular, estabilidade e estrutura de proteínas, cinética de fluxo-interrompido.

TABLE OF CONTENTS

FIGURES INDEX

1. INTRODUCTION

2. EXPERIMENTAL PROCEDURES

3. NMR FEATURES OF CHEMOTAXIS HEME SENSORS GSU0582 AND GSU0935 FROM *G. SULFURREDUCENS*

4. FOLDING MODULATES THE SWAPPED DIMERIZATION MECHANISM OF CHEMOTAXIS HEME SENSORS GSU0582 AND GSU0935 FROM *G. SULFURREDUCENS*

5. THERMODYNAMIC AND KINETIC CHARACTERIZATION OF THE CHEMOTAXIS HEME SENSORS GSU0582 AND GSU0935 FROM *G. SULFURREDUCENS*

6. ONGOING STUDIES

7. CONCLUDING REMARKS

A. APPENDIX

TABLES INDEX

1. INTRODUCTION

3. NMR FEATURES OF CHEMOTAXIS HEME SENSORS GSU0582 AND GSU0935 FROM *G. SULFURREDUCENS*

4. FOLDING MODULATES THE SWAPPED DIMERIZATION MECHANISM OF CHEMOTAXIS HEME SENSORS GSU0582 AND GSU0935 FROM *G. SULFURREDUCENS*

5. THERMODYNAMIC AND KINETIC CHARACTERIZATION OF THE CHEMOTAXIS HEME SENSORS GSU0582 AND GSU0935 FROM *G. SULFURREDUCENS*

6. ONGOINS STUDIES

A. APPENDIX

ABBREVIATIONS, SYMBOLS AND CONSTANTS

1D – one dimensional
2D – two dimensional
2xYT – 2x yeast extract-tryptone medium
5c – five-coordinated
6c – six-coordinated
AI-2 – quorum signal autoinducer-2
AMP – ampicillin
ANTAR – AmiR and NasR transcription antitermination regulators
ATP – Adenosine TriPhosphate
BLAST – Basic Local Alignment Search Tool
B. subtilis – *Bacillus subtilis*
Cache – calcium channels and chemotaxis receptor
CBD – Chromophore Binding Domain
C. crescenthus – *Caulobacter crescentus*
CCW – CounterClockWise
CD – Circular Dichroism
CHASE – cyclases/histidine kinases associated sensory extracellular
CLO – chloramphenicol
cNMP – cyclic Nucleotide-MonoPhosphate
cGMP – cyclic Guanosine MonoPhosphate
COSY – COrrelation SpectroscopY
CW – ClockWise
DBD – DNA Binding Domains
DHp – Dimerization Histidine phosphotransfer
di-GMP – cyclic diguanylate
DNA – deoxyribonucleic acid
D. vulgaris – *Desulfovibrio vulgaris*
EAL – phosphodiesterase domain that catalyzes the hydrolysis of di-GMP
E. coli – *Escherichia coli*
EDTA – EthyleneDiamine Tetraacetic Acid
ELP – Elastin-Like-Polypeptide
EPR – Electron Paramagnetic Resonance
FAD – Flavin Adenine Dinucleotide
FID – Free Induction Decay
GAF – non-catalytic cGMP-binding domain
GGDEF – guanylate cyclase domain that catalyzes synthesis of di-GMP from two GTP molecules
G. sulfurreducens – *Geobacter sulfurreducens*
G. metallireducens – *Geobacter metallireducens*
G. uraniireducens – *Geobacter uraniireducens*
GTP – Guanosine-5'-triphosphate
HAMP – domain found in Histidine kinases, Adenylate cyclases, Methyl binding proteins and Phosphatases
HD-GYP – conserved domain found in response regulator modules of various signal transduction systems
HK – Histidine Kinase
HPLC – High-Performance Liquid Chromatography
HPT – Histidine-containing PhosphoTransfer protein
Hnr – regulators of stress sigma factor RpoS
HS – High-Spin
HSQC – Heteronuclear Single-Quantum Correlation

HtrII-SrII – phototaxis sensory rhodopsin II-transducer complex
IPTG – isopropyl β-D-1-thiogalactopyranoside
IUPAC-IUB – International Union of Pure and Applied Chemistry and International Union of Biochemistry
K. pneumoniae – *Klebsiella pneumonia*
LS – Low-Spin
MAP – Mitogen-Activated Protein
MCP – Methyl-accepting Chemotaxis Proteins
MFC – Microbial Fuel Cells
M. xanthus – *Myxococcus xanthus*
NIT – Nitrate/Nitrite sensor
NMR – Nuclear Magnetic Resonance
NOE – Nuclear Overhauser Effect
NOESY – Nuclear Overhauser Enhancement SpectroscopY
ox – oxidized
PAS – Period clock protein, Aryl hydrocarbon receptor and Single-minded protein
PBP – Periplasmic solute-Binding Protein
PCD – Photosensory Core Domain
PDB – Protein Data Bank
PDC – PAS-like domain typified by PhoQ, DcuS, CitA proteins
PHY – phytochrome
pI – Isoelectric point
ppm – parts per million
REC – CheY-like phosphoacceptor
red - reduced
RNA – ribonucleic acid
r.m.s. – root-mean-square
RpoS – RNA polymerase, sigma S
RR – Respose Regulator
RRR – Response Regulator Receiver domain
SAH – S-adenosylhomocysteine
SAM – S-adenosylmethionine
S. typhimurium – *Salmonella enterica enterica* sorovar Typhimurium
SDS-PAGE – Sodium Dodecyl Sulfate PolyAcrylamide Gel Electrophoresis
S. enterica – *Salmonella enterica*
SHE – Standard Hydrogen Electrode
SMART – Simple, Modular, Architecture, Research Tool
S. meliloti – *Sinorhizobium meliloti*
TCS – Two-Component Systems
TEV – Tobacco Etch Virus
TLP – Transducer-Like Proteins
TM – TransMembrane
TOCSY – TOtal Correlation SpectroscopY
Tris – tris(hydroxymethyl)aminomethane
UV – Ultra-Violet
V. cholerae – *Vibrio cholerae*

δ – chemical shift
I – nuclear spin quantum number
S – electron spin quantum number
π/2 – pulse with a flip angle of 90º
ω – Larmor frequency or precession frequency
γ – gyromagnetic ratio
t_1 – evolution period
t_2 – detection period
B_0 – static magnetic field
B_1 – rotating magnetic field
V_t – total bed volume
K_{av} – partition coefficient
V_e – elution volume
V_0 – column void volume
θ – ellipticity
A – absorbance
N – native
U – unfolded

f – fraction

K – equilibrium constant

T – absolute temperature

ΔG^0 – standard free energy change

$\Delta G_U^{H_2O}$ – value of standard free enthalpy at zero concentration of denaturant

m – denaturant effectiveness

C_m – lower midpoint denaturant concentration

T_m – midpoint thermal unfolding or melting temperature

k_{diss} – equilibrium dissociation constant

k_{obs} – observed rate constant

E_m – midpoint redox potential

r – effective radius

Z – effective charges

k – kinetic rate constant

ε – molar absorption coefficient

λ – reorganisation energy

$\mathbf{I}$ - ionic strength

R – molar gas constant (8.314 J mol^{-1} K^{-1})

F – Faraday constant (96500 C mol^{-1})

AMINO ACID ABBREVIATIONS

Alanine	Ala	A
Arginine	Arg	R
Asparagine	Asn	N
Aspartate	Asp	D
Cysteine	Cys	C
Glutamate	Glu	E
Glutamine	Gln	Q
Glycine	Gly	G
Histidine	His	H
Isoleucine	Ile	I
Leucine	Leu	L
Lysine	Lys	K
Methionine	Met	M
Phenylalanine	Phe	F
Proline	Pro	P
Serine	Ser	S
Threonine	Thr	T
Tryptophan	Trp	W
Tyrosine	Tyr	Y
Valine	Val	V

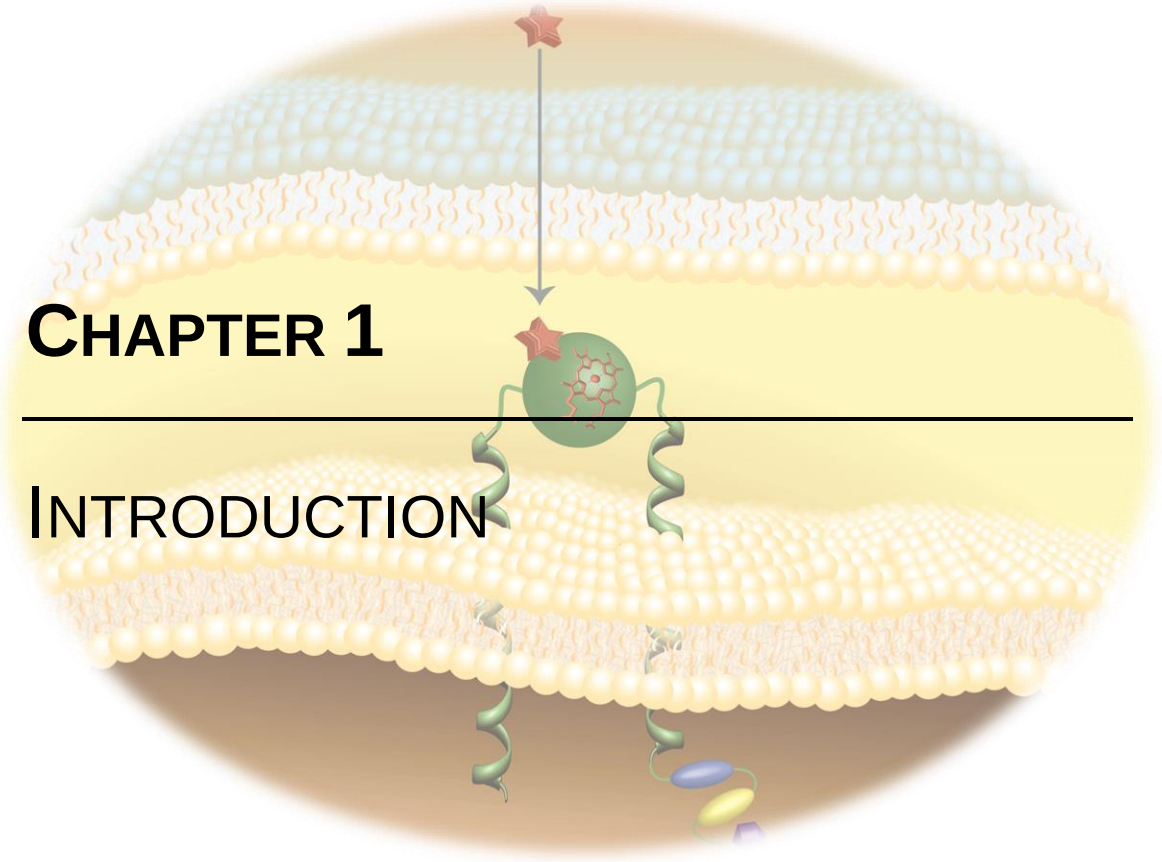

CHAPTER 1

INTRODUCTION

1. INTRODUCTION

1.1 Two-component signal transduction systems

Two-component systems (TCS) serve as a basic stimulus-response coupling mechanism to allow organisms to sense and respond to changes in many different environmental conditions including fundamental processes such as metabolism and chemotaxis [1].

The prototypical system involves a phosphotransfer reaction between a conserved histidine kinase (HK) domain, containing a kinase core, and a response regulator (RR) protein, containing a regulatory domain, which exerts a modulatory response depending upon its phosphorylation state [2, 3]. Typically, the RR is the output of the system that triggers the cellular response, and is regulated by the HK, which is the input component of the pathway. The activity of HK is modulated by the extracellular stimuli and transfers a phosphoryl group to the RR, in a reaction catalyzed by the RR. Phosphotransfer to the RR results in activation of a downstream effector domain that elicits the specific response [3].

These findings led to the propose of a phosphorylated two-component system concept for sensing a large variety of stimuli and perform a variety of functions (Figure 1.1A). The ATP-dependent phosphorylation of a conserved histidine residue of the first component and the subsequent transferring the phosphate to a conserved aspartate residue of the second component causes different responses like changing the direction of the rotation of flagella or controlling the expression of a particular gene.

The TCS are the most abundant multistep signaling pathways in Nature and despite of the inherent interest as a fundamental signaling strategy, the physiological signal that modulates their action are not precisely understood. TCS are sophisticated signaling systems marked by a highly modular design that has been adapted and integrated into a wide variety of cellular signaling circuits.

TCS are found in organisms of all domains: Bacteria, Archaea, and Eukarya, although their abundance in each domain differs substantially [3]. The *Escherichia coli* (*E. coli*) genome encodes 62 TCS, which are involved in regulating several processes such as chemotaxis, osmoregulation, metabolism and transport [4]. TCS are present in both Gram-positive and Gram-negative pathogenic bacteria, in which, in addition to regulating basic functions, they control expression of toxins and other proteins important for pathogenesis [5, 6]. In Archaea and Eukarya, two-component pathways constitute a very small number of all signaling systems. In fungi, TCS mediate environmental stress responses [7, 8] and, in pathogenic yeast, hyphal development [9-11]. In the

amoeba *Dictyostelium* and in plants, they are involved in important processes, such as osmoregulation, cell growth and differentiation [12, 13]. To date, TCS have not been identified in animals and are not encoded by the human genome [14, 15].

In prokaryotic and eukaryotic signaling systems apparently, there are significant changes in the way that the two-component proteins are used in different circumstances. Distinct arrangements of conserved domains and diverse integration of proteins into pathways provide adaptations of the basic scheme to meet the specific regulatory needs of many different signaling systems. Notably, in most prokaryotic systems, the output response is made directly by the RR, which functions as a transcription factor. In eukaryotic systems, two-component proteins are found at the beginning of signaling pathways where they interface with more conventional eukaryotic signaling strategies such as mitogen-activated protein (MAP) kinase and cyclic nucleotide cascades [16].

Similar to most signaling pathways, the architecture of the TCS is not always linear from the environment to transcription (Figure 1.1B).

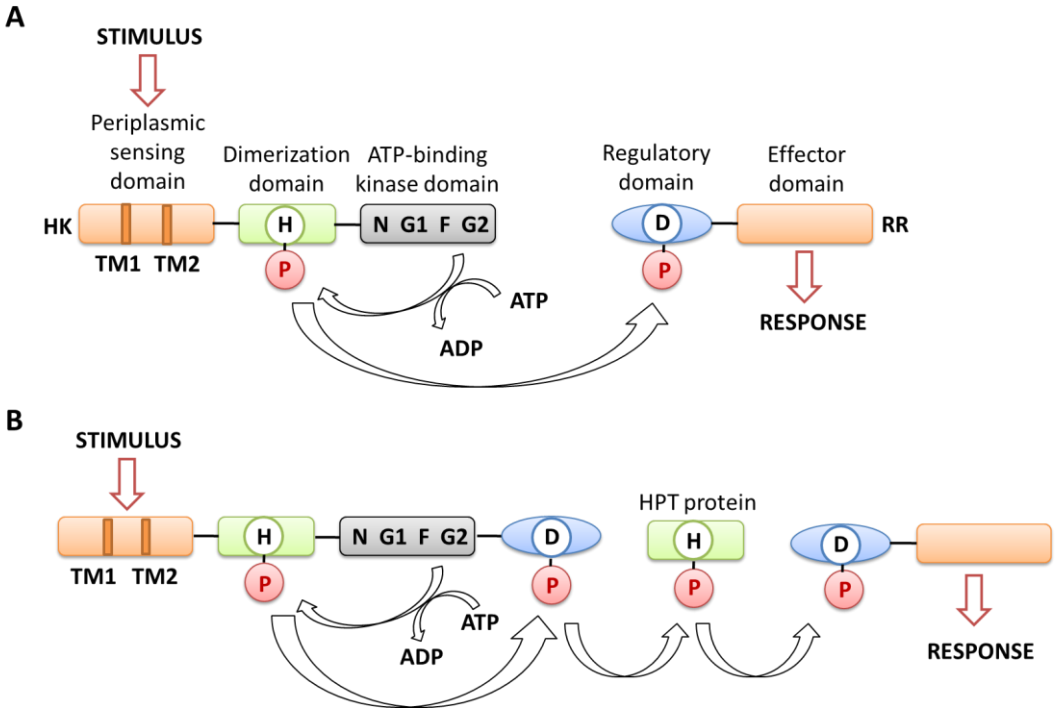

Figure 1.1 – Illustration of the fundamental phosphotransfer mechanism that forms the core of both simple and more elaborate systems. Stimuli, detected by a sensor domain, regulate HK activities. (A) Prototypical two-component pathway containing a dimeric transmembrane sensor HK and a cytoplasmic RR. A monomer of a representative HK is shown with transmembrane segments indicated by TM1 and TM2. Conserved sequence motifs N, G1, F and G2, are located in the ATP-binding domain. The HK catalyzes the ATP-dependent autophosphorylation of a conserved His residue (H) within the HK dimerization domain. The phosphoryl group (P) is then transferred to a conserved Asp residue (D) located within the conserved regulatory domain of an RR. Phosphorylation of the RR typically activates an associated (or downstream) effector domain, which ultimately elicits a specific cellular response. (B) A multi-component phosphorelay system often involve hybrid HK that has an additional RR regulatory domain at the C-terminal. This is a more complex version of the two-component phosphotransfer scheme and implicates more than one His–Asp phosphoryl transfer reaction and usually involves a His-containing phosphotransfer protein (HPT) that serves as a His-phosphorylated intermediate. Abbreviations: HK, histidine protein kinase; RR, response regulator protein. Adapted from [16].

Parallel sensory kinases affect the activity of a phosphotransferase domain within a more complex phosphorelay such as that seen for *Vibrio cholerae* (*V. cholerae*) quorum sensing [17] or for control of sporulation in *Bacillus subtilis* (*B. subtilis*) [6, 18]. Many eukaryotic signaling cascades involve protein kinases that phosphorylate both themselves and other protein substrates at specific serine, threonine or tyrosine residues thereby regulating protein activities. Several recent examples have identified response regulators containing the GGDEF domain, as PleD in *Caulobacter crescentus* (*C. crescentus*) [19] that synthesizes cyclic diguanylate (di-GMP) from GTP (guanosine-5'-triphosphate) to regulate targets that affect differentiation and biofilm formation.

The efforts to characterized systems such as bacterial chemotaxis [20], aerobic/anaerobic regulation in *E. coli* [21, 22], the sporulation system of *B. subtilis* [23, 24], differentiation in *C. crescentus* [25-27] and *Myxococcus xanthus* (*M. xanthus*) [28, 29] have provided a basic understanding of how these systems transduce extracellular signals and elicit appropriate cellular responses. In Table 1.1 is indicated a selection of some TCS with their corresponding function and signal molecule.

Table 1.1 – Selection of some two-component systems with their corresponding function and signal molecule in some examples of different microorganism. The unknown signal molecules are indicated by question marks. Adapted from [30] and [31].

System	Microorganism	Function	Signal molecule
ArcB/ArcA	*Escherichia coli*	Sensing of oxygen and redox states	Quinones reflecting the redox state
NarX/NarL	*Escherichia coli*	Nitrate and nitrite respiration	Nitrate, nitrite
CitA/CitB	*Klebsiella pneumonia*	Transport and anaerobic metabolism of citrate	Citrate
FixL/FixJ	*Bradyrhizobium japonicum*	Nitrogen fixation	O_2, CO, NO
LovK/LovR	*Caulobacter crescentus*	Bacterial cell attachment	Blue light
TodS/TodT	*Pseudomonas putida*	Degradation of benzene derivatives	Monoaromatic compounds
NtrB/NtrC	*Escherichia coli*	Nitrogen utilization	2-ketoglutarase, glutamine
KdpD/KdpE	*Escherichia coli*	K^+ supply	K^+
VanS/VanR	*Streptomyces coelicolor*	Antibiotics resistance	Vancomycin
EnvZ/Ompr	*Escherichia coli*	Osmosensing	?
KinB/Spo0F	*Bacillus subtilis*	Sporulation	?, ATP as cosignal?
BvgS/BvgA	*Bordetella pertussis*	Virulence	Temperature, sulfate ions, nicotinic acid
LuxQ/LuxO	*Vibrio harveyi*	Quorum sensing	AI-2

(continued)

System	Microorganism	Function	Signal molecule
DesR/DesK	*Bacillus subtilis*	Lipid modification	Temperature
DosS/T/DosR	*Mycobacterium tuberculosis*	Redox sensor/ hypoxia sensor	O_2, CO, NO
PhoQ/PhoP	*Salmonella enterica*	Virulence	Extracytoplasmic levels of Mg^{2+} and Ca^{2+}
DcuS/DcusR	*Escherichia coli*	Regulation of the anaerobic fumarate	C_4-dicarboxylates
NreB/NreC	*Staphylococcus carnosus*	Dissimilatory nitrate/nitrite reduction	O_2
MmoS/MmoQ	*Methylococcus capsulatus*	Controlling gene expression	Copper
NifL/NifA	*Azotobacter vinelandii*	Nitrogen fixation	O_2
DctB/DctD	*Sinorhizobium meliloti*	Controlling gene expression	C_4-dicarboxylates

1.1.1 A specialized two-component system: chemotaxis

Bacterial chemotaxis is the reason for the movement towards regions that contain either higher concentrations of beneficial compounds or lower concentrations of toxic chemicals. The bacterial chemotaxis machinery was first identified in *E. coli* and *Salmonella enterica* subspecies I, serovar Typhimurium (*S. typhimurium*) for the regulation of their flagellar-based motility. The *E. coli* chemotaxis pathway is so sensitive that it is able to sense a change in similar molecules [32, 33].

Most sequenced bacterial genomes include homologues of genes that are known to encode components of flagella and chemosensory pathways indicating that motility is widespread and probably provides a selective advantage, especially in non-homogeneous, nutrient-limiting environments. However, all bacteria in which motility has been studied seem to be chemotaxis (although two sequenced Archaea, *Aquifex aeolicus* and *Methanocaldococcus jannaschii*, with putative flagellar genes have no obvious chemosensory genes [34]). So, the ability to move is not, by itself, essential and it must be predisposed by the growth of certain bacteria in specific environments.

Several decades of research have questioned the rules of signal transduction for the chemotaxis paradigmatic system that reflects a highly modified TCS (Figure 1.2).

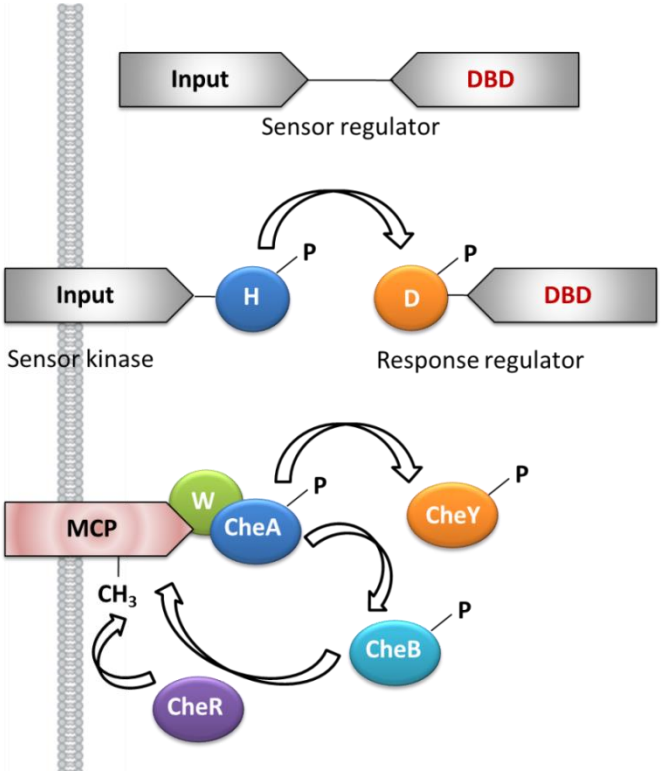

Figure 1.2 – One-component, two-component and chemosensory signal transduction in bacteria. The figure illustrates the prototypical one-component system (top), a two-component system (middle) and the specialized chemotaxis system (bottom). Represented are histidine kinase domains (H; CheA), aspartyl receiver domains (D), CheW coupling proteins (W), methyl-accepting chemotaxis protein (MCP), CheY response regulator and flagellar rotation controller, CheB methylesterase, the CheR methyltransferase and DNA binding domains (DBD). Adapted from [35].

Inputs for chemotaxis systems are transduced by the dedicated transmembrane chemoreceptor sensor proteins [methyl-accepting chemotaxis proteins (MCP) or transducer-like proteins (TLP)], which have a cytoplasmic domain, rather than by a fused sensory domain of a histidine protein kinase as is found for most systems that regulate transcription.

1.1.2 Methyl-accepting chemotaxis proteins

In 1967, Julius Adler and Margaret Dahl found that the *E. coli* B275 strain required L-methionine to grow and perform chemotaxis [36]. Thirty-nine years ago, using radioactive methionine, this research group discovered that the methyl group of methionine is incorporated into a novel protein located in the cytoplasmic membrane, the methyl-accepting chemotaxis protein [37]. In short, MCP was found to be the receptor for bacterial chemotaxis. This represented the first time that a sensory chemoreceptor was ever chemically identified. This MCP became known as MCPI (or as the serine receptor or Tsr). Another cytoplasmic membrane protein, the MCP-like receptor Aer for oxygen taxis (aerotaxis), was discovered showing that glutamic acid 5-methyl ester is the

methylated site of the MCP. This MCP-like receptor mediates aerotactic responses by monitoring redox changes in the electron transport chain undergoing a sensory adaptation through a poorly-understood, methylation-independent mechanism [38-41].

MCP are the predominant chemoreceptors in bacteria and have been found in many Archaea. The best-studied is the Tar chemoreceptor from *E. coli*, which has four MCP (Tar, Tsr, Tap and Trg) and a fifth MCP-like protein (Aer). Roger Alexander and Igor Zhulin detected 2125 MCP sequences in 152 genomes of Bacteria and Archaea [42]. Barbara A. Methé *et al.* found multiple (~70) homologs of chemotaxis genes in the *Geobacter sulfurreducens* (*G. sulfurreducens*) genome, 34 MCP genes and six major *che* gene clusters [43].

The prototypical MCP are transmembrane receptors that contain a periplasmic ligand binding domain and a cytosolic signaling domain (Figure 1.3). In general, MCP has two transmembrane-spanning domains that create a periplasmic (or extracellular) loop functioning as a ligand binding domain and a cytoplasmic component comprising the broadly conserved helical signaling domain, methylation helices for adaptation and the highly conserved domain that regulates the kinase activity [44-46]. However, large subsets of receptors that are completely cytoplasmic and detect soluble cytoplasmic signals have been identified [47] including the well-characterized *B. subtilis* aerotactic sensor HemAT. The conformation of the cytoplasmic portion of the receptor is an extended α-helical coiled coil. For transmembrane receptors, a stimulus or ligand-binding event is transduced by a piston like motion across the cytoplasmic membrane and converted to helical rotation within the cytoplasmic portion of the receptor [48].

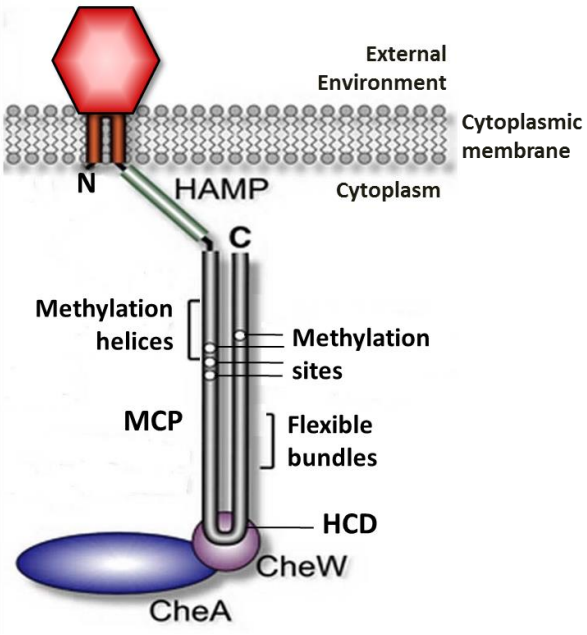

Figure 1.3 – Schematic diagram of the MCP chemoreceptors described for *Geobacter* species. Hypothetical sites of methylation are indicated by white dots. Receptors length varies accordingly to the repetition number of seven consecutive amino acids residues present within the methylation sites. (HCD) highly conserved domain. Adapted from [35].

The middle components of the chemotaxis mechanism that bridge the stimulus and the flagella switch, are the Che proteins (Table 1.2). These are coded by the *che* genes, and carry out "excitation" and "adaptation" steps. The *che* genes have been found universally among bacteria. By responding to the MCP interaction with an attractant or repellent, CheA, CheW, CheY and CheZ transmit the flagella response. Then, CheB and CheR carry out adaptation to the attractant or repellent by methylating MCP or demethylating it.

Table 1.2 – Classification and function of the middle components of the chemotaxis mechanism.

Protein Name	Class Protein	Role in Chemotaxis
MCP	Chemoreceptor	Receptor for chemotaxis stimulus.
CheA	Histidine protein kinase	Autophosphorylates in response to MCP. Phosphorylates CheY and CheB.
CheW	Adaptor protein	Required for formation of MCP-CheA-CheW complex.
CheY	Response regulator	Binds FliM when phosphorylated to alter flagellar rotation. Multiple CheY may act as phosphate sinks.
CheB	Response regulator, methylesterase	Remove methyl groups from MCP. Activated upon phosphorylation.
CheR	Methyltransferase	Constitutively methylates MCP.
CheZ	Phosphatase	Stimulates dephosphorylation of CheY, leading to signal termination.
CheV	CheW-CheY fusion	May function as a phosphate sink, leading to signal termination. Alternatively, may function in adaptation.
FliM	Motor switch protein	Alters flagellar rotation in response to CheY~P binding.

The receptor MCP is coupled by an adaptor protein CheW (or CheV) to a CheA histidine kinase and two RR (CheB and CheY) compete for binding to CheA. CheY is a specialized single-domain, flagellar motor-binding protein that regulates the response, whereas CheB, has two domains, one of which functions as a methylesterase and controls the adaptation of the MCP and the other functions as response regulator [49, 50]. CheA and CheY represent a modified TCS and, in particular, CheA displays an alternative domain organization relative to that of the prototypical sensor kinase of other TCS [51]. Rotation of the MCP chemoreceptor C-terminal transduces the signal to the highly conserved signaling domain at the tip of the receptor that contacts both CheW and CheA to regulate phosphorylation of the kinase [52, 53]. CheA~P subsequently transfers phosphoryl groups to CheY, producing CheY~P, which then diffuses from the receptor/kinase complex to its target, the flagellar motor, to promote a reversal in the direction of motor rotation [54, 55]. The second target for CheA~P is the CheB methylesterase. The activated methylesterase, CheB~P, demethylates specific and highly conserved segments located in the helices (Glx-Glx-X-X-Ala-Ser/Thr, where Glx can be a glutamine or a glutamate residue), producing a second

conformational change that counters the initial change induced by ligand binding and therefore brings about adaptation for a ligand-bound receptor complex. In *E. coli* chemotaxis, an auxiliary protein, the phosphatase CheZ, oligomerizes with the phosphorylated CheY (CheY~P) and increase the spontaneous dephosphorylation rate of CheY~P allowing the rapid signal termination [56].

The ability of cells to respond to small changes in the concentration of a large number of chemical stimuli depends on the repertoire and specific affinities of the chemoreceptors. A decreased concentration of attractant results in decreased attractant binding to the MCP, which stimulates CheA trans-autophosphorylation. This results in an increase in the CheY~P concentration. CheY~P then binds to the flagellar motor and causes it to switch to clockwise rotation, which results in cell tumbling and direction change. CheB is also phosphorylated by CheA~P, which results in an increased methylesterase activity and an increased demethylation of the MCP. Demethylated MCP has a reduced ability to induce CheA autophosphorylation (even in the presence of a low concentration of attractant), so the rate of CheA autophosphorylation and therefore the rate of rotation switch return to the pre-stimulus level. The system has now adapted and is primed to sense any subsequent increases or decreases in ligand binding (Figure 1.4). On the other hand, an increased concentration of attractant inhibits the autophosphorylation of CheA, which reduces the concentration of CheY~P and therefore the frequency of motor switching. This causes the bacterium to swim in this positive direction for longer. CheB phosphorylation and therefore activity is also reduced, which allows the constitutive methyltransferase CheR to increase the methylation of the MCP. Highly methylated MCP are efficient in the stimulation of the CheA autophosphorylation, even in the continued presence of a chemoattractant, so this returns CheA autophosphorylation to the pre-stimulus level and the bacterium to a normal frequency of direction changing (Figure 1.4).

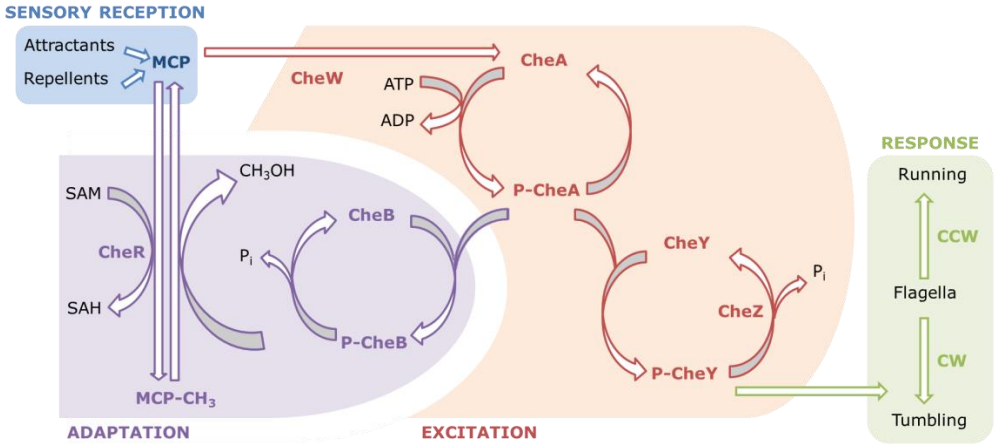

Figure 1.4 – Mechanism of chemotaxis in *E. coli*. Repellents promote the phosphorylation of CheA and consequently the phosphorylation of CheY, which brings about tumbling. Attractants block the phosphorylation of CheA and of CheY, so tumbling is not promoted, and instead, running predominates. These processes are

called excitation. Then adaptation follows: repellents cause demethylation of the methylated MCP and attractants cause its methylation. CCW, counterclockwise rotation; CW, clockwise rotation; SAH, S-adenosylhomocysteine; SAM, S-adenosylmethionine. Adapted from [57].

1.1.3 Effector domains: diversity of sensing domains

The great diversity of attached or independent effector domains creates an almost limitless variety of output responses that can be controlled through RR [58]. In prokaryotes, RR are usually the last components of signaling pathways, directly effecting the responses, while in eukaryotic TCS, RR are often intermediates, interfacing with proteins linked to common eukaryotic strategies such as MAP kinase cascades or cyclic nucleotide second messengers [59]. As noted above, ~17% of prokaryotic RR exist as stand-alone CheY-like conserved receiver domains. Most of the remaining RR contain domains can be categorized into a relatively small set of nucleic acid binding, enzymatic and protein/ligand binding domains. The majority of RR contain DNA binding effector domains dominated by a small number of structural subfamilies. These include the OmpR/PhoB winged-helix domain (30%) [60], the NarL/FixJ four-helix helix-turn-helix domain (17%) [61], the NtrC/DctD AAA+ ATPase domain fused to a factor of inversion (Fis)-type helix-turn-helix domain (10%) [62] and the recently characterized LytTR domain with an unusual, predominantly β fold (3%) [63]. RNA binding domains are found in only ~1% of RR and are mostly of the ANTAR (AmiR and NasR transcription antitermination regulators) family, functioning as antitermination factors [64]. Enzymatic domains are found in ~13% of RRs. Most of these RR (6% of all RR) are involved in regulation of cyclic diguanylate (di-GMP) [65]. Enzymatic domains include GGDEF diguanylate cyclase domains (guanylate cyclase domain that catalyzes synthesis of di-GMP from two GTP molecules) and/or phosphodiesterase domains of the EAL (phosphodiesterase domain that catalyzes the hydrolysis of di-GMP) or HD-GYP, a conserved domain found in response regulator modules of various signal transduction systems. The remaining enzymatic subfamilies, in order of prevalence, are chemotaxis methylesterase CheB domains; HK domains, which are often coupled with additional PAS (Period clock protein, Aryl hydrocarbon receptor and Single-minded protein) and/or GAF (non-catalytic cGMP-binding domain) domains. Many additional enzymatic domains in RR occur infrequently. A small and diverse group of effector domains that mediate interactions with other proteins or ligands occur in 3% of RR. Approximately half of these RR correspond to chemotaxis CheV-like proteins containing CheW domains. Additional subfamilies include tetratricopeptide repeat, Hnr-like regulators of stress sigma factor RpoS (RNA polymerase, sigma S), HPT (histidine containing phosphotransfer), PAS, GAF, and cyclic nucleotide-monophosphate (cNMP) binding domains. Structures are available for representative members of most of these effector domains.

The modular kinase core domains are coupled to an overwhelmingly diverse array of sensory domains, enabling organisms to sense a wide variety of stimuli, including small molecules, light,

turgor pressure, cell envelope stress, redox potential and electrochemical gradients. The individual sensing domains are highly variable in sequence and this is particularly evident for domains that are flanked by transmembrane domains and localized outside the cytoplasm [6].

Stimuli are sensed by these domains either directly or indirectly through protein-protein interactions with auxiliary signal transduction proteins. How the individual domains that comprise the sensor complex function to augment or attenuate the signal output in response to ligand binding has not been determined even for relatively simple systems. It seems clear that the multiplicity of domains in the sensor complex allows multiple signal output and may permit metabolic, cell cycle and other cellular processes promoting the sensor histidine kinase activity and ultimately the cell response. It is reasonable to suppose that the diversity of signals detected by the sensing domains required the evolution of a large number of distinct folds. Few common topologies have been observed in sensory domains and these systems are classified into three major groups on the basis of these membrane topologies [66] (Figure 1.5).

The first group features a cytoplasmic sensory domain responsible for sensing diffused and internal stimuli. The second group has multiple (2 to 20) membrane-spanning helices but does not contain an apparent extracellular domain. The stimuli sensed by these histidine kinases are believed to be membrane-associated. The largest group is represented by the classical histidine kinase, characterized by an extracytoplasmic sensory domain placed between two TM helices. The extracytoplasmic sensory domain includes various domain families with the extracellular stimuli transduced across the membrane to regulate the kinase/phosphatase activities. Some systems may combine multiple features of these topologies, integrating signals from different input domains, extracellular or cytoplasmic, for a concerted response to complex environments.

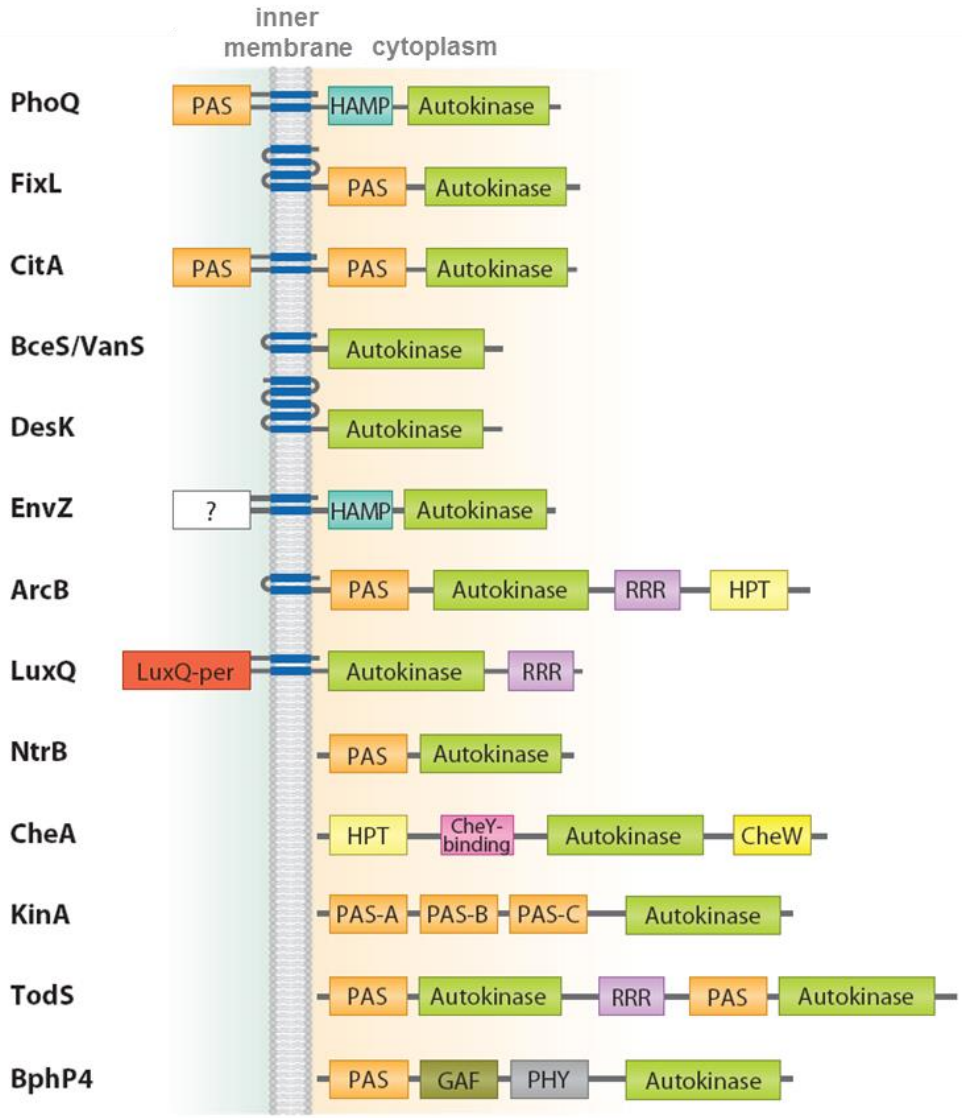

Figure 1.5 – Domain organization and topology of selected sensor kinases based on domain annotation by SMART complemented with structural information. Abbreviations: PAS, PER-ARNT-SIM; HAMP, domain found in histidine kinases, adenylyl cyclases, methyl binding proteins and phosphatases; RRR, response regulator receiver domain; HPT, histidine containing phosphotransfer; GAF domain (sensory domain first characterized in cGMP-dependent phosphodiesterase, adenylyl cyclases and *E. coli* FhlA); PHY, phytochrome. The unknown domain is indicated by question mark. Reproduced from [30].

1.1.3.1 Cytoplasmic sensor domains

Many histidine kinase receptors are entirely cytoplasmic. In the case of membrane-anchored histidine kinases, cytoplasmic sensor domains may be found either at the N-terminal before the first transmembrane segment, or after the last transmembrane segment before the C-terminal kinase domain. Studies have revealed that many cytoplasmic sensor domains adopt a PAS fold. PAS

domains are typically between 100-120 amino acids in length [67-69]. The core of a PAS domain is a five stranded β-sheet and interspersed within this core are α-helices that provide ligand/signal specificity [67, 70]. The position of α-helices can vary depending on the cellular location; specifically, cytoplasmic PAS domains have α-2β-4α-3β topology (Figure 1.6A) and extracytoplasmic PAS domains (named PAS-like - see section 1.1.3.3) have 3α-2β-1/2α-3β-α topology (Figure 1.6B) [70-73].

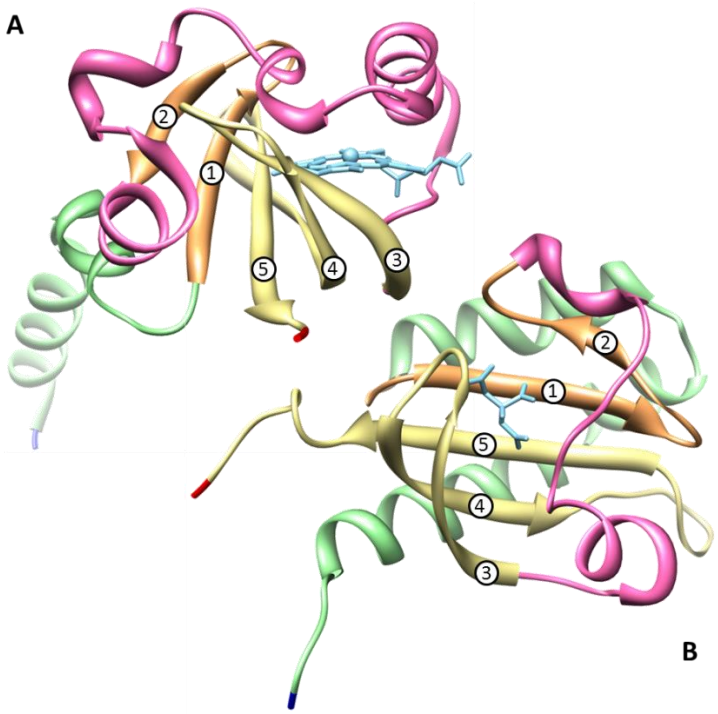

Figure 1.6 – Representative three-dimensional structures of PAS (A) and PAS-like (B) domains. The first corresponds to *Sinorhizobium meliloti* (*S. meliloti* formely *Rhizobium meliloti*) oxygen sensor FixL protein (PDB: 1D06) and the second to the ligand-binding domain of the *Klebsiella pneumoniae* sensor kinase CitA protein (PDB: 1P0Z). For both structures, the core β strands are labeled from 1 to 5. Schematic models were generated by CHIMERA [74]. Each region is colored as follows: the amino end with dark blue, the leading α-helix region with green, the first two β-strands with orange, the inter-domain α-helix region with pink, the last three β-strands with yellow, and the C-terminal with red. The heme and citrate molecules are shown in light blue stick models. Adapted from [75].

Examples of cytoplasmatic PAS include the *Bradyrhizobium japonicum* and *Sinorhizobium meliloti* (*S. meliloti*) FixL sensor domains, which were among the first structures of histidine kinase sensor domains determined and they continue to be subject to ongoing study [76-84]. FixL senses oxygen through heme, the NreB sensor detects oxygen through an iron–sulfur ($[4Fe\text{-}4S]^{2+}$) cluster [85], and the LovK photosensor domain forms a flavin adduct upon absorption of blue light [86]. In the case of the MmoS redox-sensor (Figure 1.7), two tandem PAS domains (PAS_1 and PAS_2) are found in the sensor domain with a FAD (flavin adenine dinucleotide) cofactor bound to the N-terminal PAS domain [87]. In the extensively studied ArcB redox-sensor, a putative cytoplasmic

PAS sensor domain contains redox-active cysteine residues and is regulated by changes in redox states of quinone and menaquinone pools [88, 89].

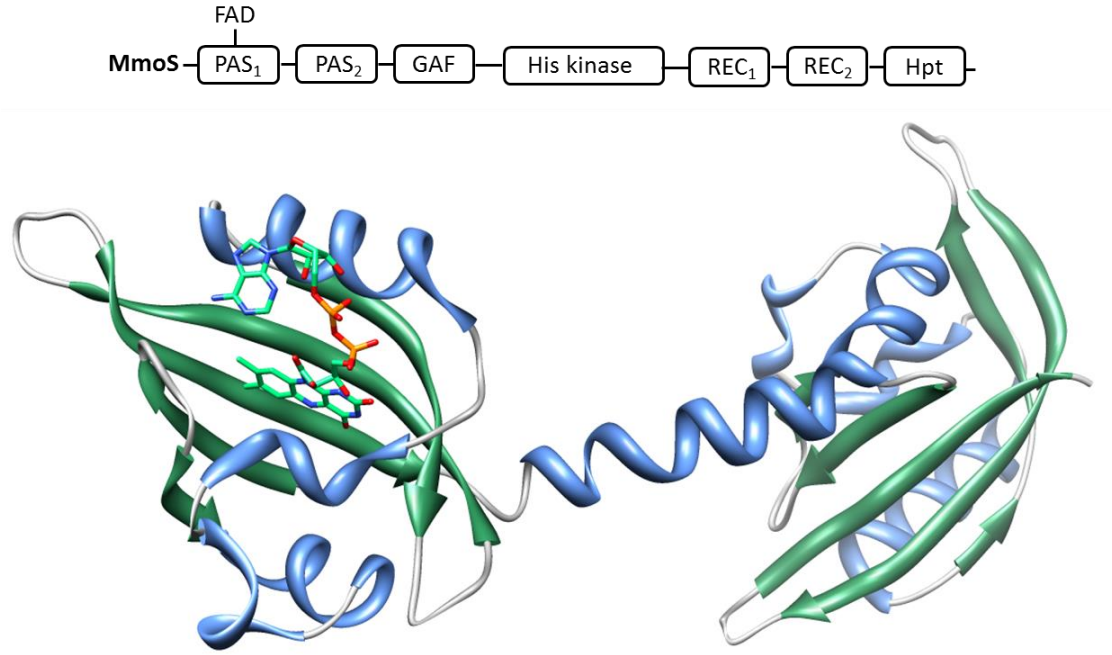

Figure 1.7 – Structure and ligand binding in flavin adenine dinucleotide (FAD)-binding PAS redox sensor domains of the *Methylococcus capsulatus* MmoS (PDB: 3EWK). The domain architecture and ribbon of the MmoS PAS_1 domain bound to FAD. β-strands are rendered in light green, α-helices in blue. Atoms of the flavin cofactor bound to the PAS_1 domain are colored by element: carbon, green; nitrogen, blue; oxygen, red. Adapted from [31].

A second structural family of cytoplasmic sensor domains features a GAF fold [90]. GAF sensor domains consist of a six stranded anti-parallel β-sheet core, related in structure to PAS domains and are often found coupled in the cytoplasmic histidine kinase sensors. Both PAS and GAF domains have rather high sequence variability and structures plasticity, making them versatile signaling domains not only for stimuli recognition but also for signal transduction, owing their propensity for protein-protein interactions.

A third family of cytoplasmic sensor domains is found in phytochromes, soluble histidine kinase photoreceptors found in bacteria, fungi, and plants. Structural studies of the *Pseudomonas aeruginosa* bacteriophytochrome photosensory core domain (PaBphP-PCD) reveals a tripartite PCD that contains a PAS, GAF, and phytochrome (PHY) domain arranged along an extended α–helix [91, 92]. Similar to the PAS and GAF domains, the PHY domain also contains a five-stranded anti-parallel β-sheet scaffold. Together the PAS and GAF domains form a chromophore binding domain (CBD) that is covalently linked to a bilin chromophore which photoconverts between red- and far-red absorbing states. Additional structural studies include the entire photosensory core domain (PCD) of *Synechocystis* 6803 Cph1 [93], CBD of *Dienococcus radiodurans* DrBphP-CBD [94] and *Rhodopseudomonas palustris* RpBphP-CBD [95].

1.1.3.2 Membrane-embedded sensor domains

Histidine kinase receptors that contain multiple transmembrane segments often lack obvious extracellular domains and in subsets of such cases, the sensory region may lie within the transmembrane segments. Biochemical and structural studies of the DesK temperature sensor show that the transmembrane regions are required for a thermal response [96, 97]. In the membrane-embedded SenS redox sensor, regulation requires binding of the secreted octameric heme-binding protein HbpS to its N-terminal transmembrane region [98]. In addition, evidence suggests that the plant Etr1 histidine kinase detects ethylene within the hydrophobic N-terminal transmembrane region [99] and the AgrC quorum sensor detects an autoinducing peptide via two short extracellular loops in proximity to the transmembrane region [100, 101]. Although no structures exist for the transmembrane regions of histidine kinase receptors, the structure of the phototaxis sensory rhodopsin II-transducer complex (HtrII-SrII) [102], in which the transducer protein forms a four-helix bundle in the membrane, provides insight into the transmembrane helical arrangement of histidine kinases.

1.1.3.3 Extracytoplasmic sensor domains

Owing to the great sequence variability of extracytoplasmic sensing domains, only a limited number were recognized as a periplasmic sensor domains, such as the periplasmic solute-binding PBP domain, Cache (Calcium channels and Chemotaxis receptor), a series of CHASE (Cyclases/Histidine kinases Associated Sensory Extracellular) and NIT (Nitrate/Nitrite sensor) domains.

Until 2003, the only periplasmic ligand-binding domain structure solved was the chemotaxis receptor Tar, which formed a four-helix bundle structure [103]. More recently, three structural classes of extracellular sensor domain were established: (i) mixed alpha-beta folds, (ii) all-alpha folds and (iii) sensor domains that show a similar fold to periplasmic binding proteins. Sequence analysis reveals a potential additional class of all-beta sensors for which no determined structures exist. Several periplasmic ligand-binding structures have become available, those of *S. typhimurium* PhoQ [104], the quorum sensor LuxQ of *Vibrio harvei* [105, 106] related CitA and DcuS-sensing domains, citrate and fumarate sensors of *E.coli* and *K. pneumoniae*, respectively [107, 108]. An interesting feature of these structures is their similar fold compared to that of the common cytoplasmic PAS sensing domains, and for these reason are referred to PDC or PAS-like domains [73]. On the other hand, the PDC sensors only share a central β-sheet scaffold with PAS domains. In addition, they contain additional N-terminal, C-terminal and transverse helices. PDC sensors defines a larger discrete domain and their extreme sequence diversities suggest independent

parallel evolution from PAS domains [109]. Structures of PDC domains are typified by the PhoQ, DcuS and CitA proteins in Figure 1.8.

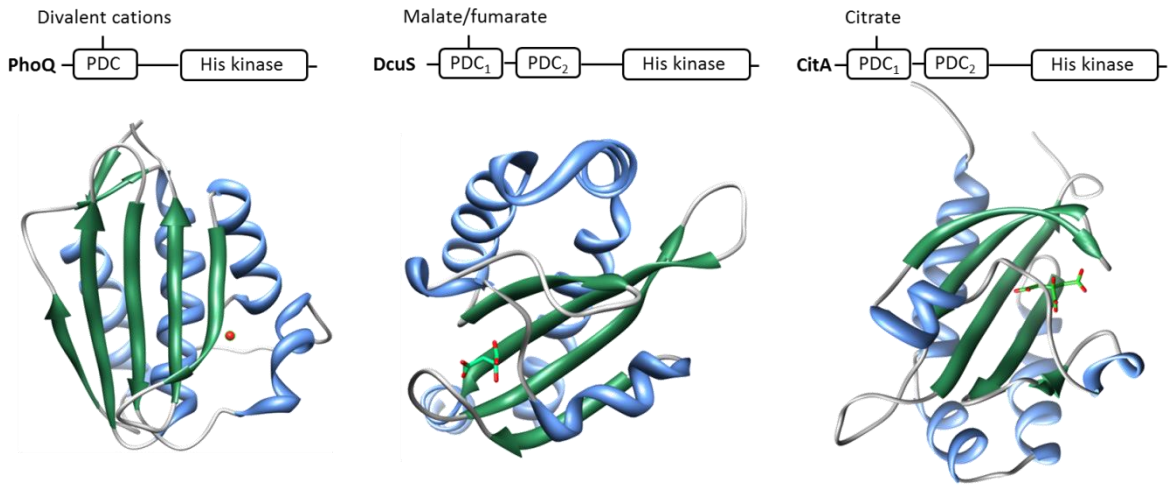

Figure 1.8 – Structure and ligand binding in the PDC domains of the PhoQ (PDB: 1ID0), DcuS (PDB: 3BY8) and CitA (PDB: 1P0Z) sensor histidine kinases. The domain architecture and ribbon of *Salmonella enterica* PhoQ PDC domain, *E. coli* DcuS PDC_1 domain and *K. pneumoniae* CitA PDC_1 domain are shown as well as the bound Mg^{2+}, atoms of the malate cofactor ions and citrate ion, respectively. β-strands are represented in green and α-helices in blue. Magnesium ion is colored in red. Atoms of the malate cofactor and citrate bound to the PAS domain are colored by element: carbon, green; oxygen, red. Adapted from [31].

Additions to the collection of PDC sensor domain structures include the oligosaccharide sensor AbfS [110] and the PhoR periplasmic domain [71]. The activities of some sensors are regulated by auxiliary proteins, which can be the primary ligand-binding protein. Structures of proteins that regulate their associated sensor kinase have become available, including LuxP which regulates above-mentioned LuxQ, the periplasmic membrane-tethered proteins YycH and YycI of *B. subtilis* known to regulate the essential YycG sensor kinase [111, 112] and the cytoplasmic proteins pXO1-118 and pXO2–61 of *Bacillus anthracis* which regulates the sporulation [113]. The dicarboxylate transport system in the *Rhizobiaceae* (and other) species is regulated by the DctB sensor kinase which senses C_4-dicarboxylic acids. DctB is membrane integrative sensor histidine kinase and shares the basic signal transduction scheme with other periplasmic sensor histidine kinases which detect periplasmic stimuli with N-terminal sensory domains transmitting the signals to cytoplasmic C-terminal kinase/phosphatase domains via transmembrane segments and the cytoplasmic helices [3].

From predicted MCP found in the genomes of *Geobacter metallireducens* (*G. metallireducens*), *G. sulfurreducens* and *Geobacter uraniireducens* (*G. uraniireducens*), ninety percent have two TM helices. Most of these, 80%, have periplasmic domains with approximately 150-200 amino acid residues, which are similar in size to the periplasmic domains of the *E. coli* MCP Tsr [114]. While the structures of most of these MCP are not known, the sensory domains of two *G. sulfurreducens* methyl-accepting chemotaxis proteins (GSU0935 and GSU0582) are PAS-

like domains with *c*-type heme groups [115] (Figure 1.9). Interestingly, this places redox-active sensing domains in the periplasm. By contrast, the MCP with small periplasmic domains are more likely to detect signals via associations with other proteins, as in the case of DifA of *M. Xanthus* [116, 117], or detect intracellular signals when the MCP have no TM segments [118]. DifA is an MCP homolog with two putative transmembrane domains which lacks an apparent periplasmic domain and is therefore probably unable to promote direct ligand binding, as with classical bacterial chemoreceptors [119].

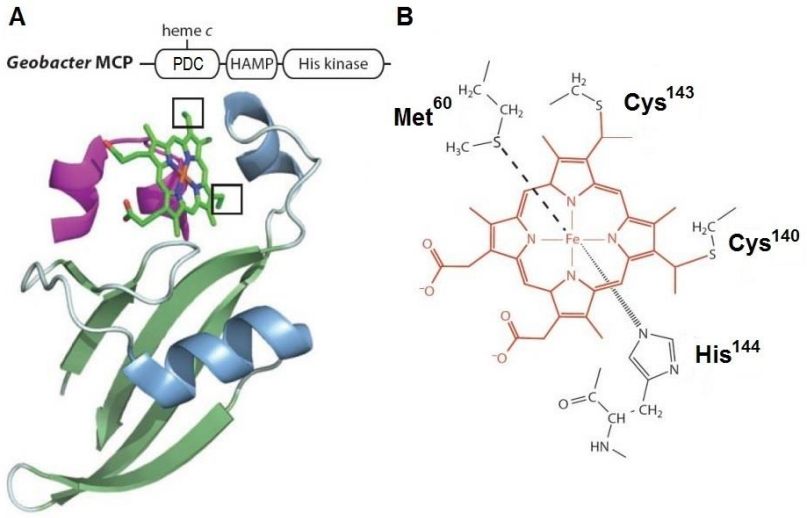

Figure 1.9 – (A) Structure of the heme pocket region of *G. sulfurreducens* methyl-accepting chemotaxis protein GSU0935 sensor domain and (B) schematic representation of heme group (red) with its binding residues (black). β-strands are rendered in light green, α-helices in blue and the heme-binding site of the monomer in purple . Atoms of the heme cofactor bound to the sensor domain are colored by element: carbon, green; nitrogen, blue; oxygen, red; iron, orange. Adapted from [31].

1.2 Signaling Mechanisms

It is widely accepted that histidine kinases exist as homodimers, and that signal transduction exists in the context of a dimer. One might blindly expect all sensor domains to form dimers in solution however, many sensor domains (NarX, DcuS, DctB, CitA) are largely monomeric [73, 120-122]. In cases where self-association has been measured (TorS and DcuS) [121, 123] high protein concentrations are needed to observe dimerization. Light scattering experiments have also shown that propensity for dimerization in solution may depend on the signaling state (LuxPQ sensor complex), and that changes in affinity at the interface may have functional relevance [106]. Therefore, unlike the regulatory mechanisms of many eukaryotic receptor families, signaling does not occur through signal mediated dimerization of kinase domains. Rather, it is believed that perception of *stimuli* causes alteration of protein-protein interactions within the preformed histidine

kinase dimer surface and that these perturbations are relayed to the kinase core domains. The recent structural evidence suggests that communication between sensor and transmitter domains in histidine kinase signaling is mediated by subtle structural changes along the dimer interface and that there may be related aspects of symmetry and asymmetry.

In recent years, structural details for several systems with known ligands have been clarified, revealing diverse ligand binding modes and the overall folds of both extracytoplasmic and cytoplasmic sensory domains. A few classes of similar folds seem to be shared despite low sequence homology and common features in TM signaling mechanisms are beginning to emerge.

Functional chimeric proteins of Tar and various systems, as EnvZ and NarX, have been successfully constructed with interchanged periplasmic sensory domains to explore the potential shared TM signaling mechanism [124, 125]. Ligand binding at the dimer interface results in a symmetrical piston-like displacement of two N-terminal helices towards the TM region and presumably, these piston-like movements are transmitted through the TM helices and reach the cytoplasmic domains, although the exact conformational changes that occur there remain unknown.

The quorum sensing LuxQ from *Vibrio harveyi* indirectly senses the quorum signal autoinducer-2 (AI-2) through interactions with the periplasmic AI-2 binding protein LuxP. Structures of $(LuxPQ_p)_2$ complexes with or without the ligand AI-2 indicate little difference in the conformations of the tandem PAS-like folds of the LuxQ periplasmic domains ($LuxQ_p$) [106]. Instead, ligand binding causes the formation of an asymmetrical dimer, and the asymmetrical positioning of individual proteins is thought to be transduced into the cytoplasm, disrupting the symmetrical dimer of kinase core domains and thereby shutting off kinase activity. Unlike the indirect sensing mechanism of LuxQ, *E. coli* and *Salmonella enterica* (*S. enterica*) PhoQ proteins directly sense divalent cations, as Mg^{2+}, and antimicrobial peptides while the sensory domains of *Klebsiella pneumonia* (*K. pneumoniae*) CitA, *S. meliloti* DctB, *V. cholerae* DctB, and *E. coli* DcuS bind to small metabolic molecules of citrate or C_4-dicarboxylates such as succinate, fumarate, and malate.

Isolated PDC domains have low intrinsic affinity for dimerization, and the plasticity of the PAS-like fold gives rise to different orientations of dimer subunits in different crystal lattices, making it difficult to distinguish the physiologically relevant quaternary structure. On the other hand, these different dimeric arrangements might also reflect different signaling states captured in different experiments that are worth further investigation, as seen in structures of *E. coli* and *S. enterica* PhoQ proteins or *K. pneumoniae* CitA [104, 107, 120, 126, 127]. Moreover, some PDC structures suggest a common feature of the close proximity of the N and C-terminal for these periplasmic sensory domains [120, 126, 127], which places the TM helices at positions compatible with a four-helix bundle similar to those of Tar and NarX. Intriguingly, citrate binding to CitA results in a contraction of the sensory domain, consistent with a piston-type movement of TM helices [120]. The highly flexible HAMP domain is usually located at the C-terminal to the last TM segment and plays an important role in relaying signals from TM regions to the kinase core. The NMR solution structure of a HAMP domain from a hyperthermophile showed a dimeric architecture and a parallel four-

helical coiled-coil with each monomer contributing two parallel helices connected by a long loop [48]. Furthermore, the coiled-coils adopted unusual knobs-to-knobs packing, deviating from the conventional knobs-to-holes packing that can be achieved by helix rotation. Hence, a rotary mechanism has been suggested for the signaling of HAMP domains; however, it is not known whether this helical rotation mechanism is generally conserved for all proteins containing HAMP domains or how the TM signaling events, sometimes piston-like movements, are converted to helix rotation in HAMP domains. Structures of individual cytoplasmic sensory domains have also been determined for a few systems, such as the PAS domains from both *B. subtilis* KinA [128] and the heme based oxygen sensor FixL in *S. meliloti* [79, 81], the GAF domains of the O_2/NO sensors DevS/DosT from *Mycobacterium* [129, 130] and the chromophore-binding bacteriophytochromes containing PAS, GAF and PHY domains [91, 93]. Binding of ligands and cofactors causes conformational changes in specific regions of these similar structures, yet it remains unknown how these changes are coupled to kinase activity until the spatial arrangements of the kinase and sensory domains are characterized. Certainly, without the barrier of the plasma membrane, signaling can be executed through signal-mediated direct contacts with the kinase as well as quaternary structural changes owing to the general plasticity of these domains. A structure of the full photosensory core domain from *Pseudomonas aeruginosa* bacteriophytochrome provides an interesting insight into the spatial organization of multiple sensory domains [91]. A long continuous helix directly connects the GAF and PHY domains and forms a parallel dimer with individual domains resembling gall-like extrusions from the central helical stem. Long coiled-coils immediately preceding the kinase domain typically extend into the four helix bundle of the DHp domain (dimerization histidine phosphotransfer). Such long helices are commonly found in various prokaryotic signaling proteins. Termed the signaling helix, this motif joins a wide variety of signaling domains such as PAS, GAF, HAMP, TM helices, DHp, REC (CheY-like phosphoacceptor), GGDEF, EAL and Ser/Thr/Tyr kinases [131].

1.3 Heme-based sensors

Heme proteins are one of the most versatile groups of proteins in Nature and they are involved in many different types of reactions such as electron transfer, oxygen transport and storage, reduction of peroxides or sensing. Though the basic structure of heme is identical among these heme proteins, the presence or absence and the nature of the axial ligands to the iron atom and the effect of the polypeptide chain of the protein on its surroundings, all contribute to this diversity of properties.

Given the great biological importance of O_2 and the fact that most organisms rapidly adapt to its fluctuations, the most common application of heme-based sensors is expected to be O_2 sensing.

The currently known heme-based sensors are grouped into four families accordingly to their heme-binding domains: heme-PAS, CooA, globin-coupled sensor and heme-NO-binding [132-135].

The heme-PAS domain family members are extraordinarily versatile and relatively well studied. Members are already known that respond specifically to O_2 or CO and whose heme-binding domains couple these dissimilar but widespread activities [132, 136-141]. These sensors demonstrably transduce signals and mediate adaptive responses by diverse strategies, including chemical modification of proteins, control of second-messenger levels and regulation of macromolecular interactions.

1.3.1 *b*-type heme sensors

As mentioned above, FixL is a heme-based oxygen sensor which controls the relative expression of proteins that function under microaerobic or anaerobic conditions [142-145] and contains one *b*-type heme group [137]. A related class of *b*-type heme-binding PAS domain is encoded by the *E. coli* direct oxygen sensor DosP (EcDOS) [138]. This sensor functions as an oxygen-regulated phosphodiesterase and catalyzes the cleavage of cyclic di-GMP into the linear dinucleotide pGpG [146, 147]. FixL-PAS and DosP-PAS_1 share a common site of heme ligation via a conserved histidine residue (Figure 1.10). The conservation of this ligation site suggests a common evolutionary origin for this gas-sensing PAS domain.

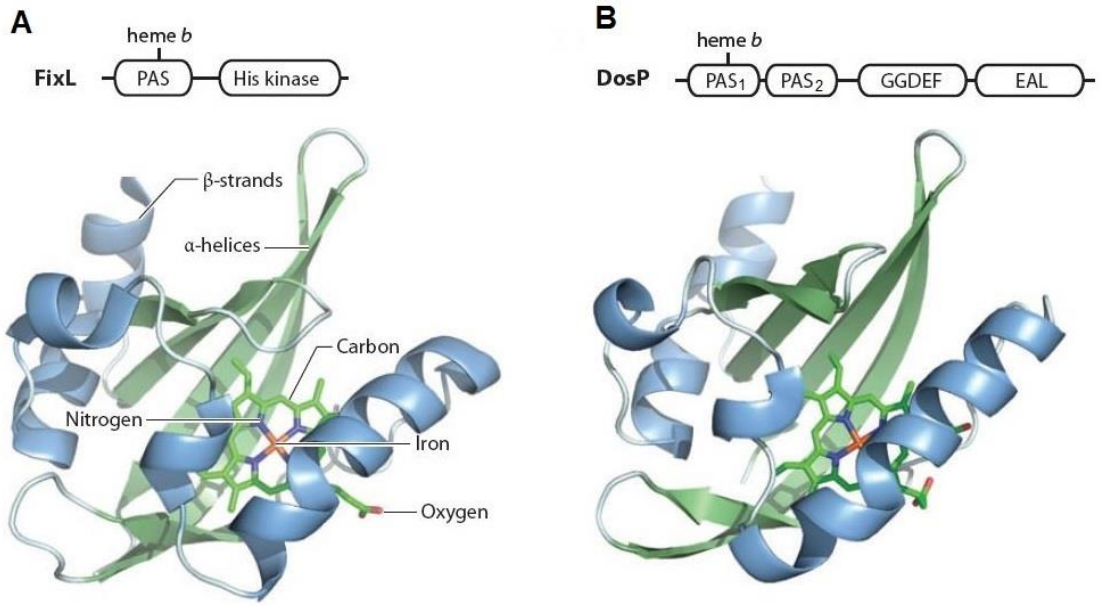

Figure 1.10 – Structure of the FixL (A) and DosP (B) PAS sensor domains. β-strands are rendered in light green, α-helices in blue. Atoms of the heme bound to the PAS domain are colored by element: carbon, green; nitrogen, blue; oxygen, red; iron, orange. Adapted from [31].

Another example of sensor domains containing a *b*-type heme group are those of GAF domain (GAF-A) of *Mycobacterium tuberculosis* DosS [148] and DosT [130]. These sensor domains specifically detect changes in the redox state of a bound iron or in binding of oxygen, respectively.

1.3.2 *c*-type heme sensors

The identification of PAS domains that bind *c*-type heme was first described in chemoreceptor proteins of *Desulfovibrio vulgaris* (*D. vulgaris*) Hildenborough (DcrA) [149] and *G. sulfurreducens* [150]. DcrA chemotaxis signal transducer protein contains a heme *c* in its periplasmic domain (DcrAN) for sensing redox and oxygen and is the first example of a heme-based sensor protein containing a *c*-type heme reported in the literature. However, DcrA has a PAS domain in its cytoplasmic domain, which does not contain any cofactor. It is natural to assume that the cytoplasmic PAS domain of DcrA may work for the output of the signal sensed by heme *c* at periplasmic space.

Although a cellular function has not been assigned to *G. sulfurreducens* GSU0582 and GSU0935, the crystal structures of the periplasmic heme *c*-binding PAS-like domains have been determined [115]. The structures showed that these sensor domains formed swapped dimers and that the heme *c* is covalently bound via a conserved bi-cysteine ligation site outside of the PAS-like domain core (Figure 1.9).

1.4 The multiple chemosensory systems in *Geobacter* bacteria

Geobacter spp. are Gram-negative δ-Proteobacteria with great respiratory diversity (Table 1.3). *Geobacter* spp. are predominant in soils and sedimentary environments and are facultative anaerobes capable of oxidize organic compounds completely to CO_2 by using metal ions, such as Fe(III), Mn(IV) and U(VI), or electrodes as terminal electron acceptors [151]. Many of the electron acceptors for *Geobacter* species are insoluble under environmental conditions. Because of their ability to transfer extracellular electrons and reduce organic materials and metals, *Geobacter* are considered an attractive species with several practical applications in the bioremediation of radioactive and toxic metals in contaminated subsurface environments and in bioenergy generation, converting organic compounds to electricity in microbial fuel cells (MFC) [152-154].

Table 1.3 – Respiratory versatility of representative *Geobacter* species. Adapted from [155].

Name	Source	Electron donors oxidized with Fe(III) [a]	Fe forms reduced [b]	Other electron acceptors [a, c]
Geobacter metallireducens	Aquatic sediments	Ac, Bz, Bze, BtOH, Buty, Bzo, BzOH, p-Cr, EtOH, p-HBz, p-HBzOH, IsoB, IsoV, Ph, Prop, PrOH, Pyr, Tol, Val	PCIO, Fe(III)-Cit	Mn(IV), Tc(VII)*, U(VI), AQDS, humics, nitrate
Geobacter sulfurreducens	Contaminated ditch	Ac, H_2	PCIO, Fe(III)-Cit, Fe(III)-P	Tc(VII)*, Co(III), U(VI), AQDS, S°, Fum, Mal, O_2
Geobacter bemidjiensis	Fe(III)-reducing subsurface sediment	Ac, Bzo, BtOH, Buty, EtOH, Fum, H_2, IsoB, Lac, Mal, Prop, Pyr, Succ, Val	Fe(III)-Cit,Fe(III)-NTA, Fe(III)-P, PCIO	AQDS, Fum, Mal, Mn(IV)
Geobacter lovleyi	Freshwater sediment	Ac, Bze, Bzo, Buty, Cit, EtOH, For, Glu, Lac, MeOH, Prop, Succ, Tol, YE	Fe(III)-Cit, PCIO	PCE, TCE, nitrate, Fum, Mal, S°, U(VI), Mn(IV)
Geobacter uraniireducens	Uranium-contaminated subsurface sediment	Ac, EtOH, Lac, Pyr	Fe(III)-NTA, Fe(III)-P, PCIO, smectite	AQDS, Fum, Mal, Mn(IV), U(VI)*

[a] Abbreviations for electron donors and acceptors: acetate (Ac), 9,10-anthraquinone-2,6-disulfonate (AQDS), benzaldehyde (Bz), benzene (Bze), benzoate(Bzo), benzylalcohol (BzOH), butanol (BtOH), butyrate(Buty), citrate (Cit), p-cresol (p-Cr), elemental sulfur (S^o), ethanol (EtOH), formate (For), fumarate (Fum), glucose (Glu), p-hydroxybenzaldehyde (p-HBz), p-hydroxybenzylalcohol (p-HBzOH), hydrogen (H_2), isobutyrate (IsoB), isovalerate (IsoV), lactate(Lac), malate (Mal), methanol (MeOH), manganese oxide (Mn(IV)), phenol (Ph), propanol (PrOH), propionate (Prop), pyruvate (Pyr), succinate (Succ), tetrachloroethylene (PCE), trichloroethylene (TCE), toluene (Tol), trichloroacetic acid (TCA), valerate (Val), xylose (Xyl), yeast extract (YE).
[b] Fe(III) forms: Poorly crystalline iron oxide (PCIO), ferric citrate (Fe(III)-cit), ferric nitrilotriacetic acid (Fe(III)-NTA), ferric pyrophosphate (Fe(III)-P).
[c,*] Organism has the ability to reduce the metal but not determined whether energy to support growth is conserved from reduction of this metal.

Several mechanisms for electron transfer from the cell interior to the electron acceptors outside the cell have been proposed. Related species such as *Shewanella* and *Geothrix* use either chelators as the terminal electron acceptor (metal oxides), or electron-shuttling compounds that transfer electrons from the cell surface to the insoluble acceptors [156]. However, *Geobacter* species use a different mechanism of electron transfer, in which the cells make direct contact with insoluble electron acceptors [157]. Cell motility and other processes that involve the synthesis of extracellular structures to mediate electron transfer are critical for *Geobacter* species survival in the environment. When grown with insoluble metal oxides, *G. metallireducens* can produce flagella and pili [158]. Moreover, it is postulated that flagellar-based motility and chemotaxis bring *G. metallireducens* cells to the metal oxide surfaces more efficiently, and that pili promote attachment and/or transfer electron [158]. In *G. sulfurreducens*, it has been demonstrated that the cells make direct contact with insoluble oxides via nanowires, pili that are electrically conductive and are essential for oxide reduction [157]. Evidences suggest that this mechanism is more widespread

than first thought [159]. The diverse functions of chemosensory systems in other bacteria suggest intriguing roles for the *Geobacter* chemotaxis and chemotaxis-like pathways.

Geobacter species can also be involved in microbial electrosynthesis converting carbon dioxide to other useful organic products, as acid acetic and butanol [160]. This technology represents an alternative form of photosynthesis using carbon dioxide and water combined to produce organic compounds with the release of oxygen. When driven with solar technology microbial electrosynthesis is an artificial form of photosynthesis that offers the possibility of converting sunlight and carbon dioxide to desirable organic compounds more efficiently and sustainable than biomass-based processes [161, 162]. *Geobacter* species have proven to be an excellent model for the development of genome-scale analysis of natural environments, bioremediation and bioenergy applications [163, 164].

Consistent with the complexity of the habitats in which *Geobacter* spp. are found, these organisms have a large number of chemosensory systems and a large repertoire of MCP chemoreceptors. Recent analysis of sequenced *Geobacter* genomes (*G. sulfurreducens* PCA, *G. metallireducens*, *G. uraniireducens*, *G. lovleyi*, *G. bemidjiensis*, *G. sp.* FRC-32, *G. sp.* M21, *G. sp.* M18 and *G. sulfurreducens* KN400) revealed an abundance of *che* gene homologs and multiple chemotaxis systems [114] (Table 1.4).

Table 1.4 – Number of chemotaxis and che genes obtained from the analysis of *Geobacter* species available genomes. Adapted from [114]**.**

Strain	**Chemotaxis genes**	**MCP**	***cheA***	***cheB***	***cheR***	***cheW***	***cheY***	***cheC***	***cheD***	***cheX***	***cheV***
***G. sulfurreducens* PCA**	79	35	4	4	4	10	10	1	3	4	1
***G. sulfurreducens* KN400**	77	34	4	4	4	8	11	1	3	4	1
G. metallireducens	68	19	5[1]	8[2]	8[2]	8	11[1]	1	3	3	1
G. uraniireducens	73	27	7	6	9	10	6	1	2	1	1
G. lovleyi	68	29	6	5[2]	7[2]	7	7	2	1	1	2
G. bemidjiensis	90	35	8	7	8	11	11	1	3	3	1
FRC-32	75	27	7	8[2]	11[2]	10	6	-	1	1	1
M21	94	37	9	7	10	12	7	2	3	3	1
M18	97	32	10	10	11	14	9	2	2	3	1

[1]The number of *cheA* and *cheY* genes in the *Geobacter sp.* genomes includes a contribution from *cheAY* fusion.
[2]The number of *cheB* and *cheR* genes in the *Geobacter sp.* genomes includes a contribution from *cheBR* fusion.

G. sulfurreducens PCA was the first *Geobacter* sp. for which the genome was fully sequenced [43] and the genetic system available [165]. This species has many MCP (Table 1.4) however only two of these proteins contain a heme *c*-binding motif: GSU0582 and GSU0935.

1.4.1 Topology of heme methyl-accepting chemotaxis proteins in *G. sulfurreducens*

The predicted topology sequence alignment of the MCP heme sensors GSU0582 and GSU0935 indicates that they have a periplasmic domain containing a heme *c*, connected via transmembrane helix to the cytoplasmic domain, which consists of a HAMP domain followed by a methyl-accepting chemotaxis protein domain (Figure 1.11).

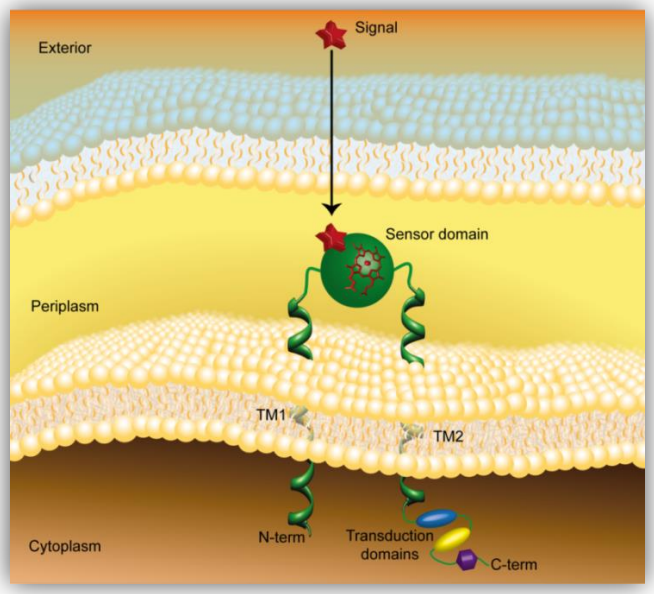

Figure 1.11 – Model of a methyl-accepting chemotaxis protein containing a periplasmic heme sensor domain that is anchored to the inner membrane by two transmembrane helices (TM1 and TM2). The second transmembrane helix connects the periplasmic domain to cytoplasmic transduction domains consisting of a HAMP domain followed by a methyl-accepting chemotaxis protein.

The ability to respond efficiently in extreme environments, such as the saturation of a specific electron acceptor, the replacement by different electron donor or even changes in the surroundings redox potential, is an essential feature of *G. sulfurreducens* bacteria which are capable to promote well-organized metabolic adjustments. The proposed action mechanism is that the sensor domain in the periplasm senses the external environment and transfers the signal through the inner membrane, activating its transducers cytoplasmic domains. This activates the second component of the system, a response regulator or proteins involved in chemotaxis and initiates the response to the original external stimulus [115] (Figure 1.12).

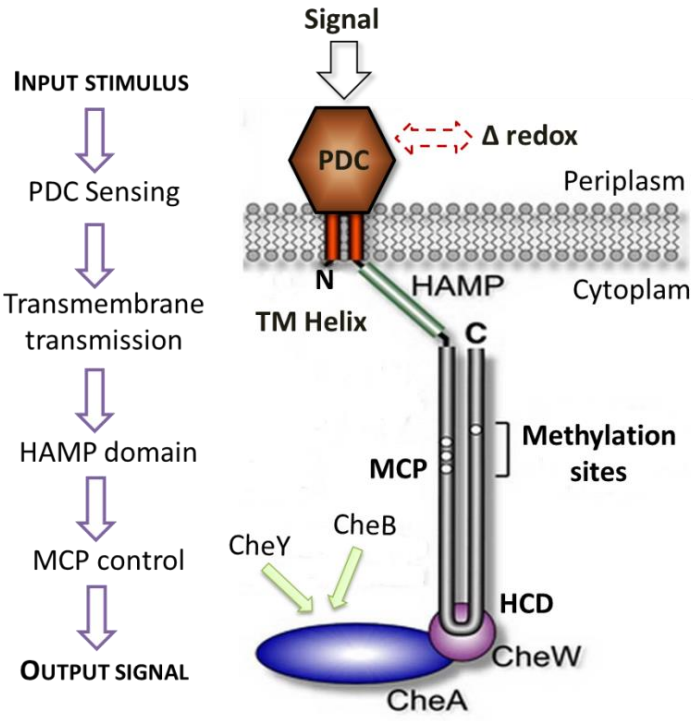

Figure 1.12 – Proposal sensing mechanism of *G. sulfurreducens* heme MCP sensors. The domain in the periplasm senses the external environment which might be related with the redox sensing and transfers the signal through the inner membrane, activating the HAMP domain and then the MCP. This last chemoreceptor transduces the signal to the highly conserved signaling domain (HCD) that contacts both CheW and CheA to regulate phosphorylation of the kinase. The response regulators involving in chemotaxis, CheY and CheB, compete for binding to CheA. CheY diffuses to the flagellar motor to control the direction of motor rotation and CheB demethylates specific and highly conserved segments located in MCP (methylation sites) controlling the adaptation for a ligand-bound receptor complex.

Sensor proteins containing periplasmic *c*-type heme provide evidence for independent evolution of a new class of heme-binding domains even though without the clarification of these chemoreceptors' function [115].

1.4.2 Structural features of heme methyl-accepting chemotaxis proteins in *G. sulfurreducens*

The sequence alignment of the GSU0582 and GSU0935 heme sensor domains indicates that they have a moderated (40%) sequence identity (Figure 1.13).

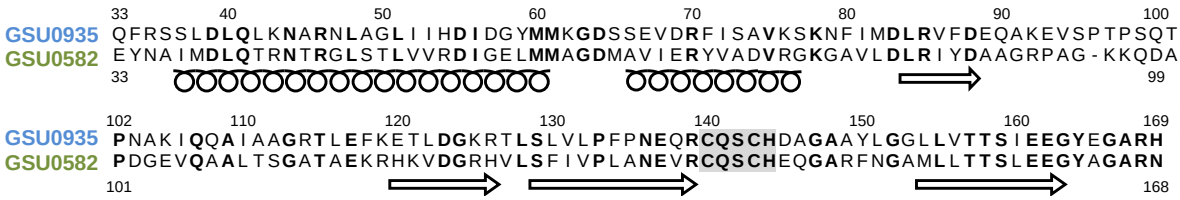

Figure 1.13 – Sequence alignment of sensor domains GSU0935 and GSU0582 from *G. sulfurreducens*. Conserved residues are shown in bold face and the heme binding motif is shown in a gray box. The alignment of the proteins was performed using the Basic Local Alignment Search Tool (BLAST) [166]. Helical segments and strand segments are indicated accordingly with the PHYRE automatic fold recognition server for secondary structure prediction [167].

Despite the moderate sequence identity of the two sensor domains, the crystal structures [115] showed that both sensors form swapped dimers from two distinct protein chains with a PAS-like fold (Figure 1.14).

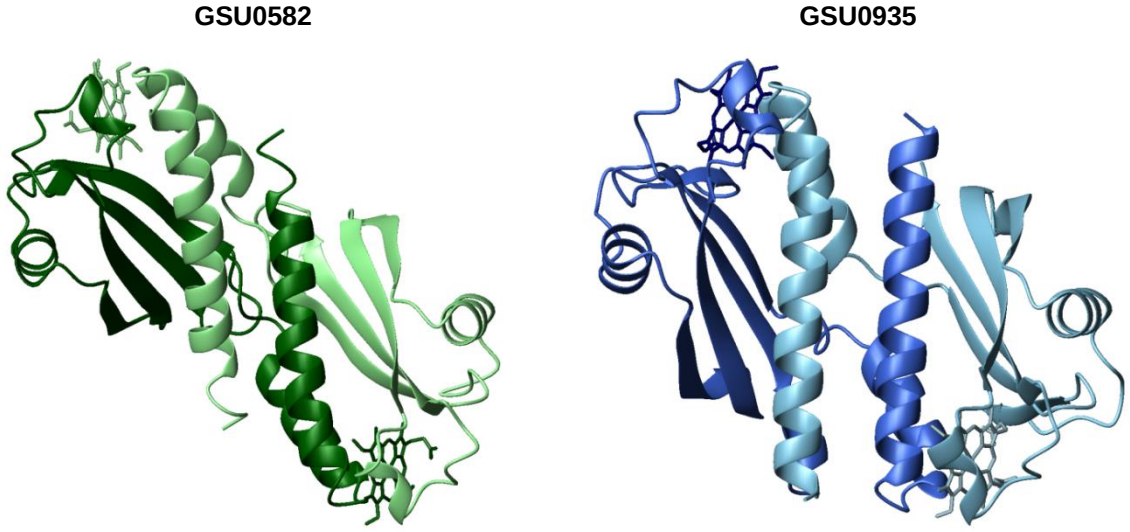

Figure 1.14 – Structure of the sensor domains GSU0582 (PDB: 3B47) and GSU0935 (PDB: 3B42) in the oxidized form. At high protein concentrations needed to obtain crystals both sensor domains form swapped dimers [115].

The swapped segment consists of two helices of about 45 residues at the N-terminal with the hemes located between the two monomers. The helices of the two monomers are antiparallel to each other and are located at the dimer interface. In GSU0582 sensor domain dimer, both hemes are high-spin with axial ligand positions occupied by His^{143} and a water molecule. In the GSU0935 sensor domain dimer, one of the hemes is also high-spin with axial ligands His^{144} and a water molecule and the other heme is low-spin, six coordinated with His^{144}-Met^{60} ligation.

Since dimers are formed at the protein concentrations used in the crystallization studies, no structural information was obtained to date for the monomeric form of these sensors domains. A

predicted monomer model was constructed using the program 3D-PSSM resulting in a sharp turn identical to what was observed in CitA structure (Figure 1.15) [115].

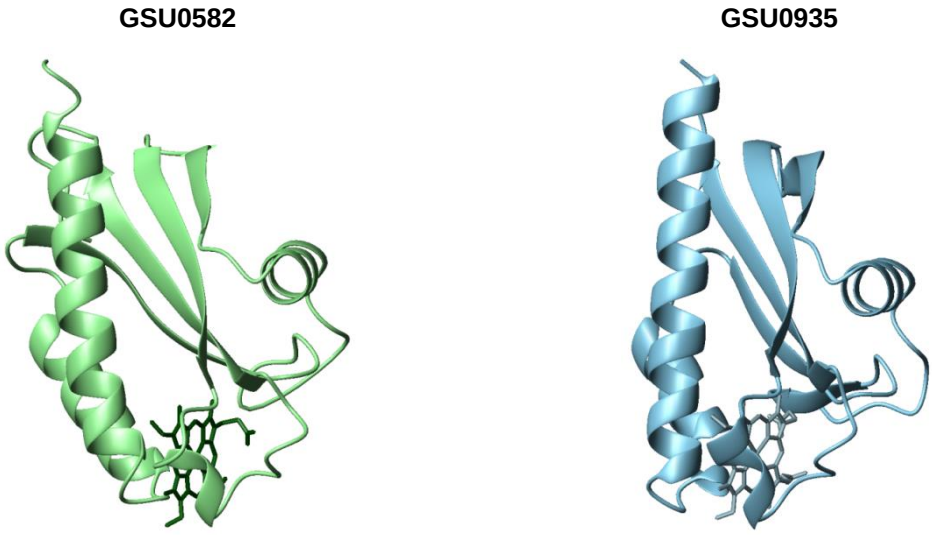

Figure 1.15 – GSU0582 and GSU0935 predicted monomer model constructed using the program 3D-PSSM. The main secondary structural elements of these molecules are two helical segments at the N-terminal followed by four-stranded antiparallel β-sheet [115].

From the comparison of the monomers and swapped dimer structures it is evident that the swapped dimerization mechanism produces severe conformational changes. Also, since the crystals were obtained in different forms and different conditions there is a chance that the dimerization process were not forced by the crystal lattice suggesting that this might be a property of these proteins [115].

The structures of these sensor domains are the first structures of PAS domains containing covalently bound heme. Optical absorption, electron paramagnetic resonance and NMR spectroscopy have revealed that the heme groups of both sensor domains are high-spin and low-spin in the oxidized and reduced forms, respectively, and that the spin state interconversion involves a heme axial ligand replacement [115].

1.4.3 Spectroscopic features of heme methyl-accepting chemotaxis proteins in *G. sulfurreducens*

The functional properties of the *G. sulfurreducens* GSU0582 and GSU0935 heme sensors were studied by spectroscopic techniques. Both *c*-type heme-containing sensors display similar spectroscopic features, as studied by UV-visible, Resonance Raman, electron paramagnetic resonance (EPR) and nuclear magnetic resonance (NMR) spectroscopic techniques [168]. These

studies showed that: (i) the heme group is high-spin in the oxidized state (S = $^5/_2$) and becomes low-spin after reduction (S = 0) upon binding of a methionine, probably Met^{60}, at the heme distal site; (ii) both sensors bind carbon monoxide (CO) in the reduced form and nitric oxide (NO) in the reduced and oxidized forms; (iii) binding of CO or NO to the reduced proteins occurs by replacing the axial ligand Met^{60}; and (iv) the binding/dissociation of CO or NO is fully reversible.

Taken together, the data from resonance Raman, molecular dynamics calculations and binding studies revealed several common features for both sensors: (i) presence of two spin populations, high-spin (HS) and low-spin (LS) in the ferric state; (ii) conversion into LS population upon reduction; (iii) CO binding to the ferrous proteins forming six-coordinated (6c) LS-CO species by replacing the distal endogenous axial ligand; (iv) NO binding to both ferric and ferrous proteins and formation of five-coordinated (5c) HS-NO and 6cLS-NO species in both redox states. In addition, in the ferrous form, the periplasmic sensors GSU0582 and GSU0935 do not show any discrimination between the two diatomic gases CO and NO. In the ferric form, however, the GSU0582 reveals much higher affinity for NO [168]. These results show that both CO and NO bind in a similar manner to the distal face of the ferrous heme by replacing the endogenous Met^{60} ligand. However, due to the intrinsic properties of each ligand, significantly different effects occur upon binding. The formation of 5cFe-NO complexes clearly demonstrates that the NO trans labializing effect is operational in both ferrous sensors. It weakens the proximal His-Fe bond in these complexes compared to Fe^{2+}-CO or Fe^{3+}-NO states. In GSU0582 and GSU0935 sensors NO only partially breaks the proximal His-Fe bond reveling that the proximal His is part of the heme *c* binding motif. In fact, being covalently bond to the heme, Cys^{143} retains the His^{144} in its proximity yielding a 5cNO structure that is very similar to the 6cNO one. Thus, it is tempting to speculate that the change of the redox state coupled to heme spin state/coordination alteration could be the putative signal transduction mechanism in the *Geobater* sensors. An intriguing possibility is presented by the 6cHis-Met/5cHis equilibrium, which relies on the breaking of Fe-Met^{60} bond. These results show that both proteins are stable in the two states and that changes due to Met coordination are significant. As in most heme proteins, the axial methionine binds strongly to the ferrous state and can be detached only in the ferric state, as confirmed by the resonance Raman data. Therefore the following mechanism can be suggested: the protein is kept blocked in the inactive/ferrous state, until a change in the environment redox potential oxidizes the protein, which releases Met^{60} and allows activation [168].

Despite the structural similarity depicted by sensors GSU0582 and GSU0935 the results obtained from the pH titrations monitored UV-visible spectroscopy indicate that both sensors are different. Unlike GSU0582, the GSU0935 sensor domain displays significant variations in the potential values over the physiological pH's (6.0-8.0). This difference must reflect variations at the heme environments in the two sensors, which modulate the affinity of the heme groups for electrons [169]. The difference in the reduction potential of these proteins may have physiological relevance,

since it could allow the bacteria to adapt to changes in the redox potential of the environment by using sensors with redox-linked ligand switches that respond to different solution potentials and trigger the adequate metabolic responses. Additional cell physiology studies are necessary to define the physiological ligand sensed by heme *c* and the regulatory function of these heme *c*-binding chemoreceptors.

The main goal of this Thesis is to contribute to improve the knowledge of the functional and structural features of *G.sulfurreducens* heme sensors proteins GSU0582 and GSU0935, which are related with poorly understood chemotaxis sensing processes. Apart from their inherent interest as fundamental signaling mechanisms, it is hoped that obtaining more insight of these systems might be useful for the development of strategic plans to use *G. sulfurreducens* bacteria to enhance the environmental remediation and energy production.

CHAPTER 2

EXPERIMENTAL PROCEDURES

2. EXPERIMENTAL PROCEDURES

This Chapter describes the experimental procedures used to express and purify the *c*-type heme sensor domains of MCP GSU0582 and GSU0935 from *G. sulfurreducens* studied under the scope of this Thesis. The experimental procedures inherent to the characterization of the sensor domains are described in detail in each corresponding Chapter.

2.1 Heterologous expression of GSU0582 and GSU0935 sensor domains

All the molecular biology experiments and development of heterologous expression and protein purification methodology were done by the collaborative group at the Argonne National Laboratory, Argonne, Illinois, USA headed by Dr. Marianne Schiffer. The DNA sequences for mature sensor domains were previously cloned and the plasmid pEC86 a kind gift from Dr. Thöny-Meyer (Zürich, Switzerland).

2.1.1 Plasmids

The production of the GSU0582 and GSU0935 sensor domains was achieved *via* co-expression (see below) of two separate vectors using the protease-deficient *E. coli* strain SF110 as host: (i) the plasmid pEC86 containing the chloramphenicol (CLO) resistance genes and the cytochrome *c* maturation gene cluster *ccmABCDEFGH* [57] and (ii) the plasmids pA02 and pA91 containing the ampicillin (AMP) resistance genes and the DNA sequences for mature sensors of GSU0582 and GSU0935, respectively. The DNA sequences for mature sensors were cloned in the expression plasmid containing the *lac* promoter, N-terminal fusions to elastin-like-polypeptide (ELP) tag followed by a cleavage site for TEV (Tobacco Etch Virus) protease, and extra residues added at the N-terminal of the domains as needed for cloning (Figure 2.1).

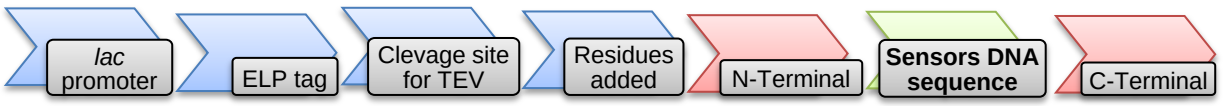

Figure 2.1 – Schematic representation of the plasmid pA02 and pA91 regions carrying genes for the antibiotic resistance, *lac* promoter, ELP tag and the cleavage site for TEV followed by residues required for cloning the gene of interest [115].

The *lac* promoter is induced when Isopropyl β-D-1-thiogalactopyranoside (IPTG) binds to the *lac* repressor. This causes an allosteric change in the repressor conformation that prevents the interaction between the repressor and the promoter allowing the transcription the *lac* genes and thereby leading to higher levels of the encoded proteins.

ELP are artificial biopolymers containing repeats of the pentapeptide sequence ValProGlyXGly, where X can be any naturally occurring amino acid except Pro [170] and are simple and versatile tools for protein purification. ELP are structurally disordered, highly solvated, and therefore soluble in aqueous solutions, but as the temperature and salt concentration are raised the polymer gradually collapses to shed bound water resulting in the formation of intramolecular contacts between nonpolar regions of the ELP [171, 172]. At a critical temperature and salt concentration the ELP undergoes a phase transition, leading to aggregation of the polypeptide within a narrow temperature range [170, 173].

TEV is a highly specific protease and functions under a wide range of conditions. Its optimal recognition sequence is GluAsnLeuTyrPheGln followed by either Ser or Gly. Cleavage occurs after the Gln residue. Some residues may be altered, but changes in the positions occupied by Glu, Tyr or Gln drastically reduce the efficiency of cleavage. The plasmid pATV67 containing the DNA sequences for TEV protease was used to produce this protein using *E. coli* strain BL21 (DE3) has host (see below).

The expressed sensor domain of GSU0582 consisted of residues Asn^{35}–Asn^{168} with Ser added at the N-terminal and the expressed sensor domain of GSU0935 had residues Arg^{35}–His^{169} with a SerAsnAla sequence added at the N-terminal.

2.1.2 Protein expression

Competent cells of protease-deficient *E. coli* strain SF110 harboring plasmid pEC86 were transformed with the expression plasmids (pA02 for GSU0582 and pA91 for GSU0935 sensor domains) and grown overnight at 37 ºC in solid 2x yeast extract–tryptone medium (2xYT) supplemented with 34 µg/mL of chloramphenicol (for pEC86 selection) and 100 µg/mL of ampicillin (for expression plasmid selection), both from NZYTech. Isolated colonies were used for growth in liquid media for protein overexpression.

Cells were aerobically grown at 30 ºC up to absorbance at 600 nm ($\boldsymbol{A}_{600}$) of 1.5–1.8 at a shaking speed of 200 rpm in 2xYT medium supplemented with CLO and AMP at the previous concentrations. At this point, protein expression was induced with IPTG at a final concentration of 33 µM and cultures allowed to grow overnight at 30 °C at a shaking speed of 160 rpm [115].

2.2 Protein purification

Proteins were purified as previously described [115, 174]. Cultures were harvested by centrifugation at 6400 *g* for 20 min at 4 ºC and lysed by osmotic shock. The cells pellet was gently resuspended in 30 mL of ice-cold lysis buffer (100 mM Tris-HCl, pH 8.0, 0.5 mM EDTA, 20% sucrose) per liter of cell culture, containing a protease inhibitor cocktail and 0.5 mg/mL lysozyme. The cell suspension was incubated at room temperature for 20 min followed by the addition of 30 mL of cold deionized water and incubation on ice for 20 min with gentle shaking. The supernatant constituting the periplasmic fraction was recovered by centrifugation at 12000 *g* at 4 ºC for 20 min. The supernatant was mixed with an equal volume of 5 M NaCl to trigger ELP precipitation and centrifuged at 20000 *g* at room temperature for 60 min. The precipitate, containing the fusion protein was dissolved in 10 mL of 50 mM Tris–HCl, pH 8.0, 0.5 mM EDTA and the solution was centrifuged at 20000 *g* for 20 min at 4 ºC to remove insoluble material. The protein quantity in the resulting supernatant was estimated using a correlation between the absorbance (A) of the Soret band of the oxidized form and protein concentration (A_{soret} = 1 corresponds to about 0.58 mg/mL). TEV protease was added in a ratio of 1 mg of TEV per 10 mg of fusion protein and cleavage reaction was incubated 48 h at 4 ºC. Samples were run in a 15% SDS-PAGE gel to confirm the completed cleavage. Then, 5 M NaCl was added to a final concentration of 2.5 M to precipitate the cleaved ELP tag. The solution was centrifuged at 20000 *g* at room temperature for 20 min and the supernatant was recovered. The supernatant was concentrated to 1 mL by ultrafiltration using Centricon YM3 units (Millipore) and the buffer exchanged to 100 mM sodium phosphate buffer solution at pH 8.0.

The next purification step was performed on an analytical-scale XK 16/70 column (GE Healthcare) packed with SuperdexTM 75 (GE Healthcare) previously equilibrated with 100 mM sodium phosphate at pH 8.0. Protein was eluted at a flow rate of 0.5 mL/min and the protein purity was evaluated by a SDS-PAGE (15%), stained with Coomassie brilliant blue (Sigma).

Purified proteins were concentrated by ultrafiltration methods using Centricon YM3 units. Protein concentration was determined from the absorbance of the Soret band of the oxidized form using the specific absorption coefficient of 188 000 $M^{-1}cm^{-1}$ determined for both sensors [168]. The yield of protein obtained after purification was typically 2 mg per liter of culture. The entire illustration of the expression and purification process of the heme sensor proteins is depicted in Figure 2.2.

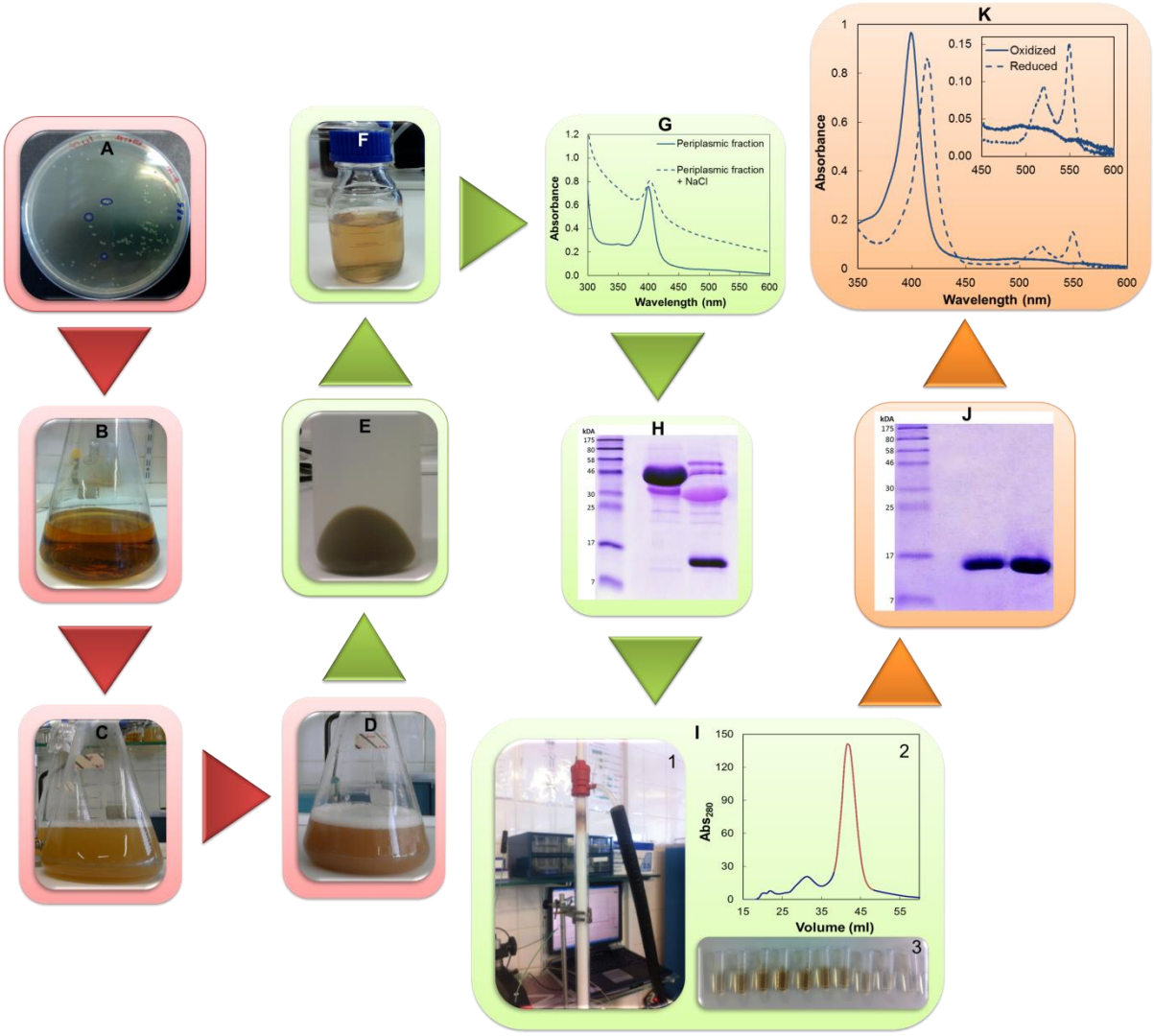

Figure 2.2 – Overview of the heme sensor expression and purification. A) Isolated colonies used for protein expression; B) Aerobic growth of cells in 1 L of 2xYT medium supplemented with 34 µg/mL of CLO and 100 µg/mL of AMP at 30 ºC; C) Cell culture after 10 h of grown and ready for induction with IPTG; D) Culture after induction and overnight grown; E) Pellets obtained after cultures harvested; F) Periplasmic fraction obtained after lysis by osmotic shock and lysozyme action. The brown color reveals the presence of the protein; G) UV-visible spectra illustrating the ELP precipitation with NaCl; H) Confirmation of the ELP cleavage by the TEV protease using electrophoresis with SDS-PAGE (15%). Lane 1: Prestained Protein Marker, Broad Range 7-175 kDa (New England Biolabs); lane 2: GSU0935 sensor domain before the TEV cleavage; lane 3: GSU0935 sensor domain after the TEV cleavage. The molecular weight of the protein markers are indicated on the left; I) Molecular exclusion column chromatography equilibrated with 100 mM sodium phosphate buffer, pH 8.0 (1); elution profile for the GSU0935 sensor domain with the fractions of interest recovered in red (2); brownish color presented by the purified protein (3); J) Purity analysis by electrophoresis with SDS-PAGE. Lane 1: as in H panel; lane 2: GSU0935 sensor domain after purification by molecular exclusion chromatography; lane 3: GSU0582 sensor domain after purification by molecular exclusion chromatography; K) UV-visible absorption spectra of GSU0935 sensor domain. The solid and dashed lines represent fully oxidized and fully reduced species, respectively. The oxidized form shows a band with a maximum at 401 nm (Soret band) and weak bands at 494 nm and 623 nm. Upon reduction with an excess of sodium dithionite, the protein shows the Soret band at 415 nm, the α band at 551 nm and the β band at 522 nm. The inset displays the spectrum between 450 nm and 650 nm plotted with an enlarge scale for clarity.

2.3 TEV protease preparation

The production of the TEV protease was accomplished using a frozen stock of *E. coli* strain BL21 (DE3) that lacks both the lon and the ompT membrane proteases. It also includes the expression plasmid pATV67, which confers resistance to AMP, and the pLysS plasmid that contain the genes encoding for the CLO resistance and T7 lysozyme. The cells are lysogenic for λ-DE3, which comprises the T7 bacteriophage gene I for T7 RNA polymerase that is expressed upon addition of IPTG inducing a high-level protein expression from T7 promoter driven expression vectors. The T7 lysozyme suppresses the activity of T7 RNA polymerase reducing the basal level protein expression from the gene of interest. This feature is important to increase the tolerance of the *E. coli* cells against the toxicity.

The *E. coli* cultures from a frozen stock were incubated overnight at 37 ºC in 2xYT solid medium supplemented with 34 µg/mL of CLO and 100 µg/mL of AMP. Isolated colonies were used for aerobically growth at 30 ºC and 200 rpm in 50 mL of liquid 2xYT, also supplemented with CLO and AMP and later transferred to 1 L of fresh media and incubated at 20 ºC and 200 rpm. After reaching $\boldsymbol{A}_{600}$ of 0.5–0.6 the cultures were induced with IPTG (final concentration of 100 µM) and allowed to grow overnight at a shaking speed of 160 rpm.

Cell were harvested, by centrifugation at 4 ºC and 2500 *g* for 20 min and ressuspended in 50 mL of 50 mM HEPES pH 7.5, 100 mM NaCl, 10% glycerol, 10 mM β-mercaptoethanol per liter of cell culture, containing 1 mg/mL lysozyme. The suspension was incubated at room temperature for 30 min and the complete cell disruption was achieved using the AVESTIN® EmulsiFlex-C5 high pressure homogenizer. During this process, a small amount of DNAse was added to ensure DNA degradation and, consequently, a cleaner sample. Cell disruption was followed by centrifugation at 4 ºC and 20000 *g* for 20 min and the supernatant filtered with 0.45 µm filter (Whatman) in order to remove insoluble particles. An equal volume of 5 M NaCl was added to the filtered supernatant solution to trigger ELP precipitation and then centrifuged at 3500 *g* at room temperature for 30 min. The pellet was gently dissolved in ice-cold lysis buffer (100 mM Tris-HCl, pH 8.0, 0.5 mM EDTA, 20% sucrose) and the suspension was centrifuged at 20000 *g* for 20 min at 4 ºC. The TEV protease quantification, in the resulting supernatant, was estimated using a correlation between the absorbance at 280 nm in the oxidized form and the protein concentration ($\boldsymbol{A}_{280}$ = 0.5 corresponds to about 0.10 mg/mL). The purified TEV was stored at -80 ºC.

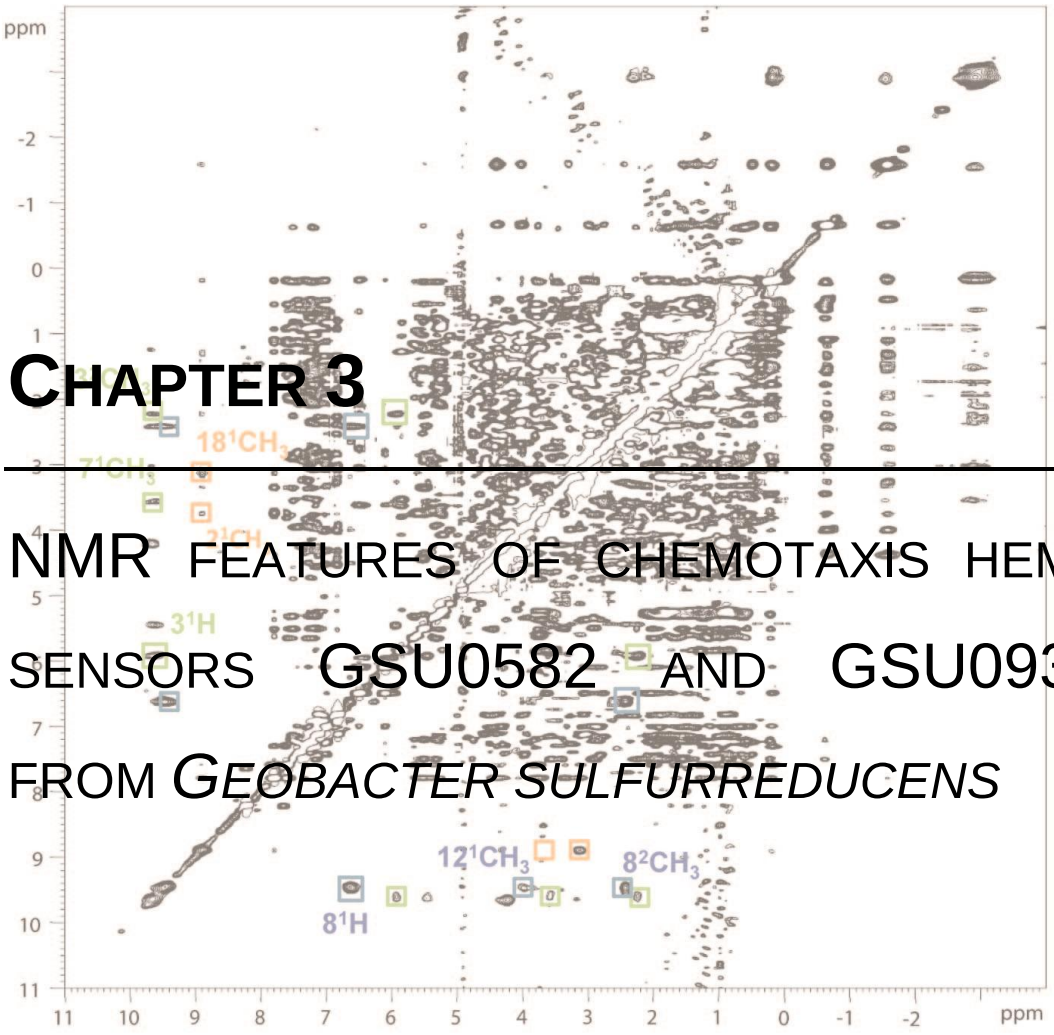

CHAPTER 3

NMR FEATURES OF CHEMOTAXIS HEME SENSORS GSU0582 AND GSU0935 FROM *GEOBACTER SULFURREDUCENS*

3. NMR FEATURES OF CHEMOTAXIS HEME SENSORS GSU0582 AND GSU0935 FROM *G. SULFURREDUCENS*

3.1 Abstract

This Chapter describes the NMR studies carried out on two chemotaxis heme sensors from *Geobacter sulfurreducens*, GSU0582 and GSU0935 with the focus on probing and identifying conformational changes in the neighborhood of the heme group of these sensors upon binding of an effector molecule. The two proteins showed equivalent NMR spectra in both oxidized and reduced forms. However, the NMR spectral features of the sensors were quite distinct in the oxidized and reduced forms. In the first, the NMR signals were extremely broad, preventing the confident assignment of the signals. In the reduced state the NMR spectral quality improved but residual broadness of the signals was still detectable, indicating the presence of two conformations in solution. Nonetheless, the heme proton NMR signals of GSU0582 and GSU0935 sensor domains were assigned using 2D-TOCSY and 2D-NOESY NMR experiments. Also, an isotopically labeled (^{13}C and ^{15}N) sample of sensor GSU0935 was obtained and used to monitor the presence of multiple forms in solution. Temperature and ionic strength dependence studies revealed favorable effects on the contribution of one conformer for the overall NMR signals but the assignment of the polypeptide signals could not be established yet.

3.2 Introduction

NMR spectroscopy becomes a fundamental tool for monitoring protein conformational changes. These changes are crucial for signal transduction mechanisms in sensory proteins. In order to map key polypeptide regions that undergo conformational changes in response to a stimulus, it is important to assign the protein signals in the NMR spectra. This includes the sequential assignment of NH backbone and side chain signals. Due to the low natural abundance of the NMR detectable nuclei ^{13}C (1.1%) and ^{15}N (0.4%), the assignment of the backbone and polypeptide NMR signals usually requires the isotopic labeling of the proteins. However, for heme sensor proteins, in addition to the contribution of the polypeptide chain signals, it is particularly important to assign the NMR signals of the heme substituents. In fact, as described in Chapter 1, specific ligand binding to the heme groups or changes in the redox potential lead to important

modifications on the spectroscopic features of GSU0582 and GSU0935 sensor domains. Therefore, conformational changes in the vicinity of the heme groups could be essential for signal response triggering. These changes are expected to modify the chemical environment of the heme signals and can probably be monitored by chemical shift perturbation NMR experiments. Under this scope, the assignment of the heme NMR proton signals is one of the first steps to understand the functional mechanism of GSU0582 and GSU0935 sensors.

In the case of *c*-type hemes, there are several proton-containing groups that contribute to the NMR resonances ensemble, four methyl groups, four meso protons, two thioether protons, two thioether methyl and two propionate groups (Figure 3.1). However, the assignment of these signals is not always straightforward, in particular for paramagnetic proteins.

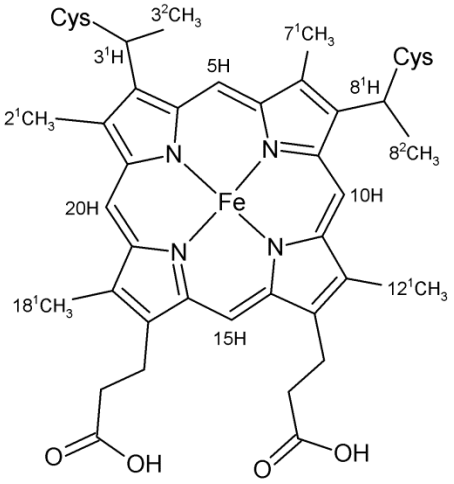

Figure 3.1 – Diagram of a heme *c* numbered according to the IUPAC-IUB nomenclature [175].

The heme sensor domains GSU0582 and GSU0935 have a pentacoordinated high-spin heme (S = $^5/_2$) in the oxidized state, which becomes hexacoordinated and low-spin (S = 0) after reduction. Therefore, the hemes in the sensor domains are paramagnetic in the oxidized form and diamagnetic in the reduced state. In the latter, the assignment of the heme NMR signals is simplified since they are dominated by the porphyrin ring-current shifts and, therefore, appear in well-defined regions of the NMR spectra. These are 11 to 7 ppm for meso protons 5H, 10H, 15H, and 20H; 7 to 5 ppm for protons 3^1H and 8^1H; 5 to 1 ppm for heme methyls 2^1CH_3, 7^1CH_3, 12^1CH_3, and 18^1CH_3; and 3 to -1.5 ppm for thioether methyls 3^2CH_3 and 8^2CH_3 [176]. The only exception is observed for the heme propionate protons, as they are structurally more variable. These regions are illustrated for the low-spin monoheme in cytochrome PccH from *G. sulfurreducens* in Figure 3.2.

On the contrary, due to the presence of unpaired electron in high-spin hemes in the oxidized form, the paramagnetic effect of the iron unpaired electrons, causes the spread of the heme signals, as well as those of the amino acid residues located in their neighborhoods, all over large

NMR spectral width. Except for heme methyls, there are no typical regions for the heme substituent (Figure 3.2).

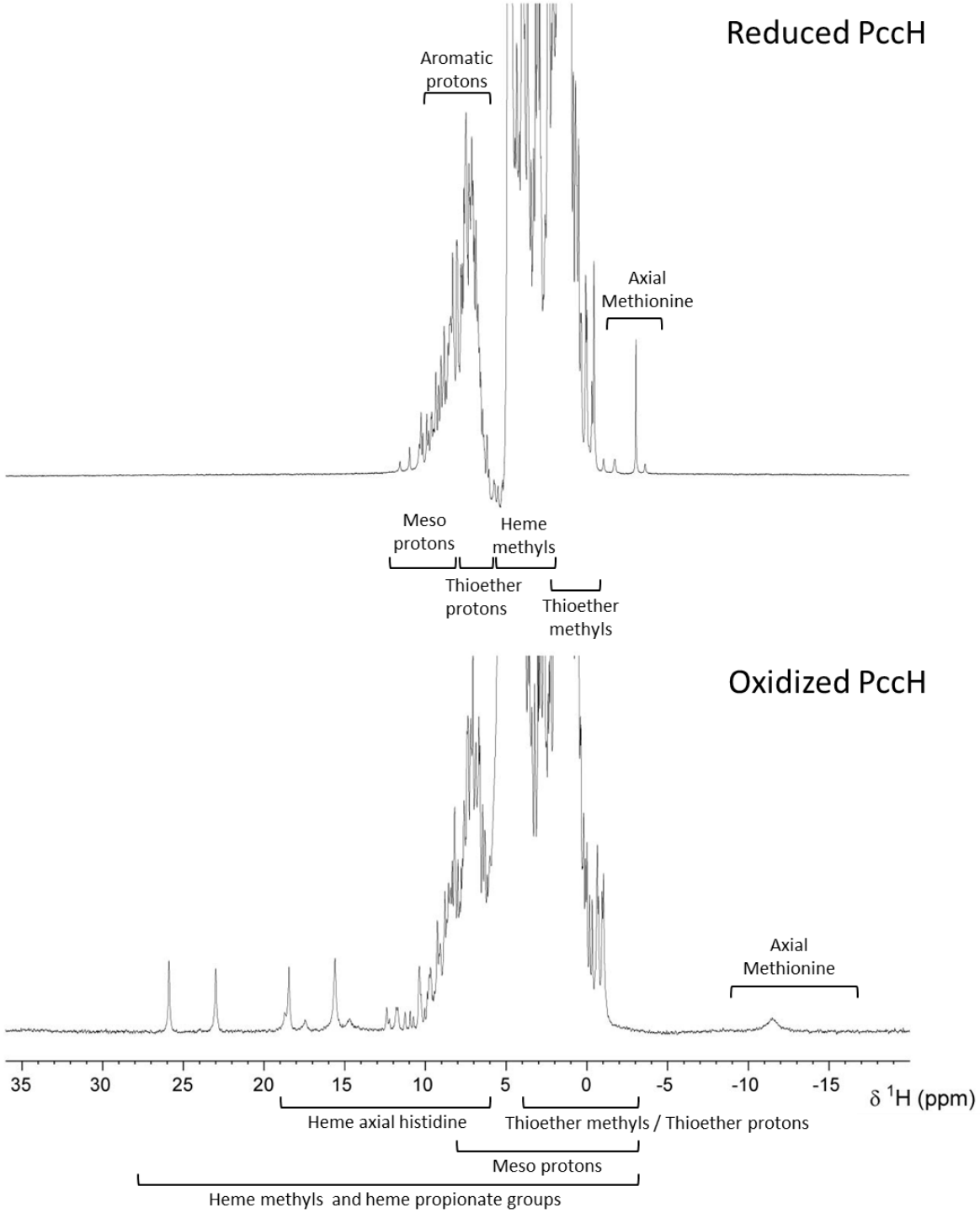

Figure 3.2 – 1D-^{1}H NMR spectra of the reduced (top) and oxidized (bottom) unlabeled cytochrome PccH from *Geobacter sulfurreducens* (140 μM) obtained at 25 ºC and pH 7.0. The typical regions of the heme substituents and heme axial ligands (histidine-methionine) are indicated.

Additionally, the NMR relaxation rates are fast compared to diamagnetic proteins, and these resonances are generally broader, which makes the complete assignment of the heme and polypeptide resonances a laborious and very time consuming task. NMR signal dispersion and broadness are even more remarkable in the case of the high-spin heme groups, as in the case of GSU0582 and GSU0935 sensor domains, due to the presence of multiple unpaired electrons.

Therefore, for the reasons described above, the NMR studies on GSU0582 and GSU0935 sensor domains were carried out on the reduced form. The studies aimed to assign the heme proton and the apoprotein NMR signals. 2D-NMR spectra were acquired for natural abundance samples prepared in D_2O in order to unambiguously assign the heme proton signals following the strategy first described by David Turner *et al.* [177]. Enriched ^{13}C and ^{15}N samples were prepared to study the apoprotein signals. These samples were obtained with an experimental methodology that uses an expression system optimized to produce cost-effective labeling of heme *c*-type cytochromes in *E. coli* that is based on two major aspects: (i) use of a two-step culture growth procedure, where cells were first grown in rich media and then transferred to minimal media containing ^{13}C-labeled glucose and ^{15}N-labeled ammonium chloride, and (ii) incorporation of the heme precursor α-aminolevulinic acid in minimal culture media [174].

3.3 Materials and Methods

3.3.1 Basic principles of NMR

Nuclear magnetic resonance spectroscopy is nowadays one of the most powerful and widely used techniques in the structural and functional characterization of biological molecules. As any spectroscopic technique, NMR uses the outcome of the interaction between electromagnetic radiation and matter to obtain information on a sample. The sample is placed in a strong and homogeneous magnetic field, and is subjected to electromagnetic radiation. Some nuclei will absorb radiation at a frequency determined by three factors: (i) the chemical nature of nucleus, (ii) the chemical environment surrounding the nucleus, (iii) and the strength of the magnetic field. NMR spectroscopy can be performed on nuclei that are sensitive to an external magnetic field, B_0, generated by the spectrometer. Both neutrons and protons have the quantum mechanical property of spin (I) and occupy defined energy levels. Only nuclei with non-zero spin are sensitive to the external magnetic field and can be observed by NMR. When these nuclei are placed in an external magnetic field, their magnetic moment will precess about the direction of the field. This precessional motion occurs with a frequency ω (Equation 3.1), which is proportional to the intensity of the effective magnetic field and to the gyromagnetic ratio of the nucleus (γ).

$$\omega = \gamma \mathbf{B_0} \quad (3.1)$$

This is called the Larmor equation and defines both the frequency of the precession of the magnetic moment about the direction of the external field and the energy splitting associated with the transitions between nuclear magnetic states [178].

When placed in a magnetic field the spins will be found precessing predominantly in the lower energy state. The difference in the number of spins depends on I, and on the energy separation between the states. The small excess of spins precessing in the state of low energy generates a macroscopic magnetization aligned with the magnetic field. Transitions between the low and high energy states are achieved by applying a magnetic field perpendicular to the static field generated by the magnet. This second field (B_1) is applied as electromagnetic radiation for a short duration (pulse). When B_1 field matches the Larmor frequency, energy will be absorbed by the nuclei and the difference between spins up and down will be reduced, reducing the macroscopic magnetization in the *z* direction. However, magnetization will not be eliminated. Instead it will be flipped away from the direction of the static B_0 field, because the nuclear spins are no longer randomly distributed and will point in the direction of the B_1 field *i.e*. they develop coherence. The flip angle achieved by the pulse depends on the nature of the nucleus, the strength of the B_1 field, and on the duration of the pulse. The maximum signal is observed for a pulse with a flip angle of 90º, which is also typically called a π/2 pulse. After switching off the B_1 field the spins gradually lose the coherence and the macroscopic magnetization returns to the direction of the static B_0 field. These two phenomena are called relaxation and follow an exponential decay. This is the free induction decay or FID. NMR spectrometers record a FID that is Fourier transformed to obtain a spectrum. Fortunately, nuclei of the same nature can have slightly different Larmor frequencies depending on the surrounding environment. Therefore, the nuclei sense an effective field that is different from the static field due to the influence of the surrounding electronic environment (the nuclear shielding) appear as dispersed signals in a NMR spectrum. The chemical shift (δ) is defined as the ratio between the nuclear shielding and the static magnetic field and is reported in parts per million relative to a reference compound [179].

Multidimensional NMR spectra can provide more information about a molecule than 1D NMR and are especially useful to more complex molecules like proteins and nuclei acids. The multidimensional NMR description in this Thesis is confined to the 2D NMR experiments used. Briefly, a 2D NMR spectrum is obtained by recording a series of 1D NMR ones. The experiment is initiated by a preparation procedure that can have different degrees of complexity depending on the specific experiment, but includes a 90º pulse. There is a waiting period called t_1 during which magnetization evolves. The magnetization is again manipulated by procedures that include another 90º pulse, and finally signals are recorded during a period called t_2. For each subsequent spectrum the t_1 period is incremented so that the signal recorded is a function of the t_1 period. At the end it is

possible to obtain a series of FID that depend on the t_1 period and can be Fourier transformed relative to this t_1 time and to the normal acquisition time t_2. The results are reported as a 2D contour map with signals located at the correct frequency for both evolution periods [180].

Multidimensional NMR experiments can be homonuclear when they correlate signals of nuclei of the same nature in all dimensions, or heteronuclear when nuclei of different nature are correlated in the various dimensions. For example, 2D-^{1}H COSY (COrrelation SpectroscopY) and 2D-^{1}H TOCSY (TOtal Correlation SpectroscopY) experiments use scalar coupling (through bond nuclear interactions) to correlate the spins within a spin system. In contrast to what succeeds in COSY, in TOCSY cross peaks are observed not only for nuclei which are directly coupled, but also between nuclei which are connected by a chain of couplings. On the other hand, in the 2D-^{1}H NOESY (Nuclear Overhauser Effect SpectroscopY) experiment the magnetization is exchanged between all protons using the NOE (Nuclear Overhauser Effect), establishing spatial proximity between protons. Finally, the 2D-^{1}H-^{13}C or 2D-^{1}H-^{15}N HSQC (Heteronuclear Single Quantum Correlation) NMR experiments correlates coupled heteronuclear spins across a single bond and identify directly connected nuclei [181].

3.3.2 Production of ^{13}C, ^{15}N enriched GSU0935 sensor domain

The sensor domain GSU0935 was isotopically labeled following the methodology previous developed for labeling *c*-type heme cytochromes [174]. The *E. coli* transformation and the initial steps of growth were the same as described for unlabeled samples in Chapter 2. However, after reaching $\boldsymbol{A}_{600}$ of 1.5–1.8, cells were harvested and washed twice, by centrifuge/resuspension cycles, with 250 mL per liter of culture of a salt solution containing 240 mM Na_2HPO_4, 110 mM KH_2PO_4 and 43 mM NaCl [174]. Cells were then resuspended in minimal medium (in a ratio of 250 mL of minimal medium for each liter of 2xYT medium) containing 48 mM Na_2HPO_4, 22 mM KH_2PO_4 and 8.6 mM NaCl, 20 mg/L biotin, 2 mM $MgSO_4.7H_2O$, 0.1 mM $CaCl_2$, 5 µM $MnCl_2.4H_2O$, 10 µM $FeSO_4.7H_2O$, 20 mg/L vitamin B_1, 1 mM of the heme precursor δ-aminolevulinic acid, 1 g/L $^{15}NH_4Cl$ and 4 g/L $^{13}C_6H_{12}O_6$ as nitrogen and carbon sources, respectively [174]. Cells were incubated at 37 ºC for 1 h at 200 rpm for recovery and clearance of unlabeled metabolites. After 1 h, protein expression was induced with 83 µM IPTG and cells were allowed to grow overnight at 30 ºC and 160 rpm [174]. The proteins were purified according to the procedures described for unlabeled samples in Chapter 2. The yield of double-labeled protein obtained after purification was 1.1 mg per liter of culture.

3.3.3 NMR Experiments

NMR experiments were acquired on a Bruker Avance 600 MHz spectrometer available at Faculdade de Ciências e Tecnologia, Universidade Nova de Lisboa or on a Bruker Avance 800 MHz spectrometer available at Instituto de Química-Física "Rocasolano", Consejo Superior de Investigaciones Científicas (Madrid, Spain), both equipped with triple-resonance cryoprobes. Proton chemical shifts were calibrated using the water signal as internal reference. Nitrogen and carbon chemical shifts were calibrated through indirect referencing [182]. Spectra were processed using TOPSPIN (BrukerBiospin, Karlsruhe, Germany) and analyzed with Sparky [183].

For the assignment of the heme proton signals a series of 2D-^{1}H NOESY with 80 and 150 ms mixing-time and 2D-^{1}H TOCSY with 60 ms mixing time were acquired on fully reduced unlabeled samples in D_2O at pH 8.0 and 286 K. The spectra were acquired on a BrukerAvance 600 MHz spectrometer. Complete reduction of the sample was achieved by the reaction with gaseous hydrogen in the presence of catalytic amounts of the enzyme hydrogenase from bacterium *D. vulgaris* (Hildenborough) or by the addition of a small excess of sodium dithionite.

1D-^{1}H NMR spectra were obtained with 0.4 mM sensor domains samples with a spectral width of 78 kHz and 512 scans per increment, before and after each multidimensional spectrum to confirm protein integrity and fully reduction. The 2D-NMR spectra were recorded with a spectral width of 108 kHz and 136 scans per increment.

For the assignment of the polypeptide signals of the sensor domain GSU0935 in the reduced form, 1.0 mM of ^{13}C ^{15}N labeled sample in 32 mM of sodium phosphate buffer at pH 7.4 in 8%D_2O/$^{2}H_2O$ was used and the following set of experiments was acquired on a BrukerAvance 800 MHz spectrometer: 2D-^{1}H-^{15}N HSQC with a spectral window of 12 kHz and 2.8 kHz in proton and nitrogen dimensions, respectively, and 32 scans per increment, and 2D-^{1}H-^{13}C HSQC with a spectral window of 12 kHz and 15 kHz in proton and carbon dimensions, respectively, and 32 scans per increment. The spectra were acquired over the temperature range 278-308 K and ionic strength (I) range 100-574 mM. Sodium dithionite was used to reduce the samples. 1D-^{1}H NMR spectra of reduced samples with hydrogenase and sodium dithionite were compared to confirm that sodium dithionite degradation products at pH 7.4 did not affect the spectral features of the protein. 1D-^{1}H NMR spectra were also obtained before and after each multidimensional spectrum to confirm protein integrity and fully reduction, with a spectral width of 16 kHz and 80 scans per increment.

3.4 Results and Discussion

The heme sensor domains GSU0582 and GSU0935 have appropriate molecular weights (approximately 15.1 and 15.7 kDa, respectively) for structural studies in solution. As described in Chapter 1 of this Thesis, the heme groups in both sensors domains are diamagnetic (S = 0) and paramagnetic (S = $^5/_2$) in the reduced and oxidized form, respectively [115].

The 1D-^{1}H NMR spectra of both sensors are indicated in Figure 3.3. As expected, the spectral widths and signal broadness are considerably different in the reduced and oxidized forms. In the reduced form, signals are spanned over a spectral width of 14 ppm. On the other hand due to the presence of five unpaired electrons in the fully oxidized proteins the spectral widths are considerable larger (90 ppm). For the same reason, the signals are too broad in the oxidized samples.

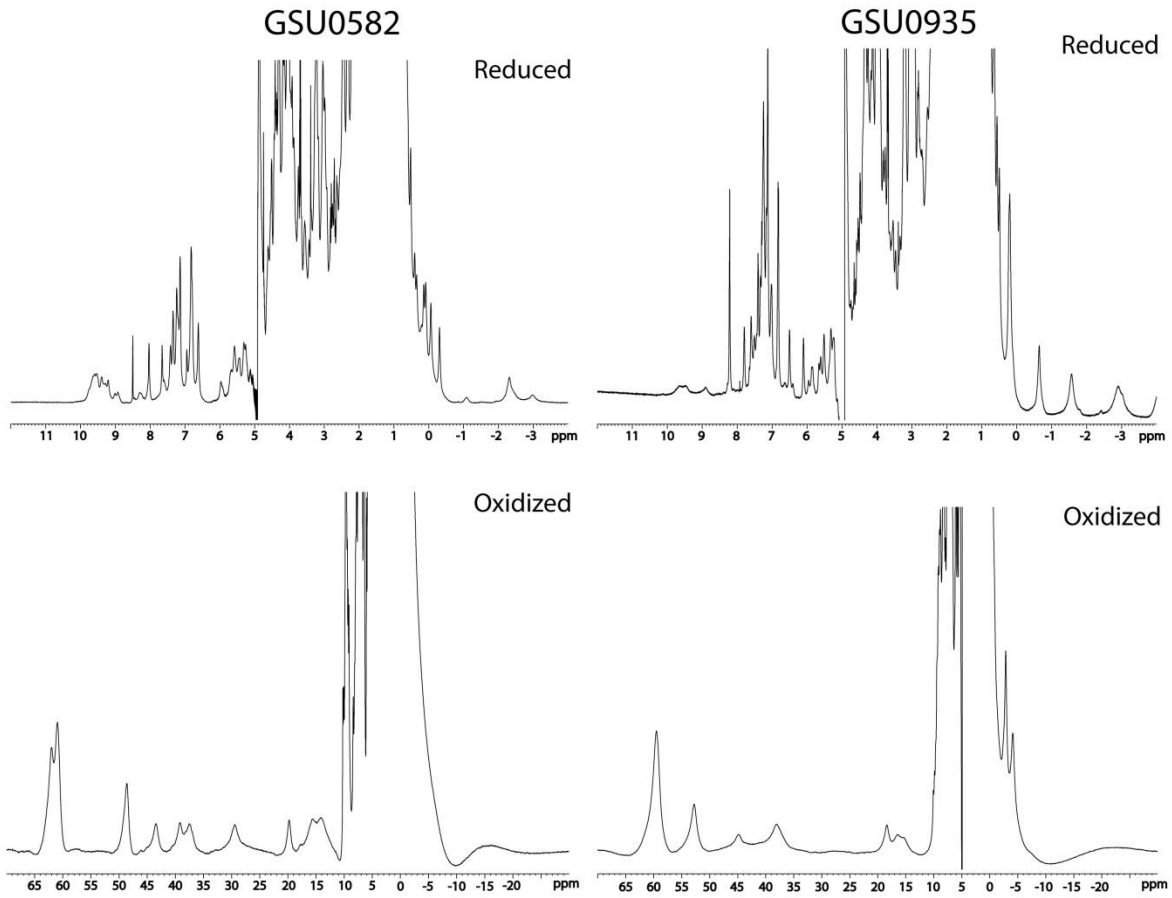

Figure 3.3 – 1D-^{1}H-NMR of oxidized and reduced sensor domains prepared in D_2O (pH 8.0 and 16 ºC). Bottom and upper spectra correspond to the fully oxidized and reduced samples, respectively.

The broadness of the NMR signals in the oxidized form impairs their assignment and therefore it was decided to select the reduced state for more detailed NMR studies. The reduction of the samples can be easily achieved by the addition of sodium dithionite. However, since the sensors domains are pentacoordinated in the oxidized state the degradation products of sodium dithionite (which are pH dependent) can eventually bind to the empty axial position of the heme. Therefore, attempts to reduce the protein were carried out, with gaseous hydrogen in the presence of catalytic amounts of hydrogenase from *D. vulgaris* (Hildenborough). The redox titration of GSU0935 sensor domain is indicated in (Figure 3.4) and shows that complete reduction was achieved.

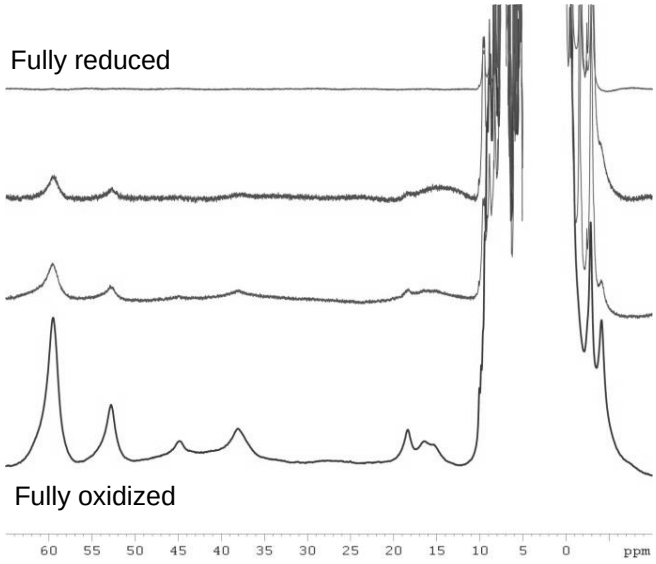

Figure 3.4 – Monitorization by 1D-^{1}H-NMR of the GSU0935 sensor domain reduction with *D. vulgaris* (Hildenborough) hydrogenase. Bottom and upper spectra correspond to the fully oxidized and reduced sample, respectively. The spectra corresponding to partially oxidized samples were obtained at different times during the reduction process.

For more concentrated samples, reduction with hydrogenase was a very slow process and reduction was achieved by sodium dithionite. In such cases, 1D-^{1}H-NMR spectra of the reduced samples by the two methods were compared to confirm that the spectral features of the protein were maintained (Figure 3.5).

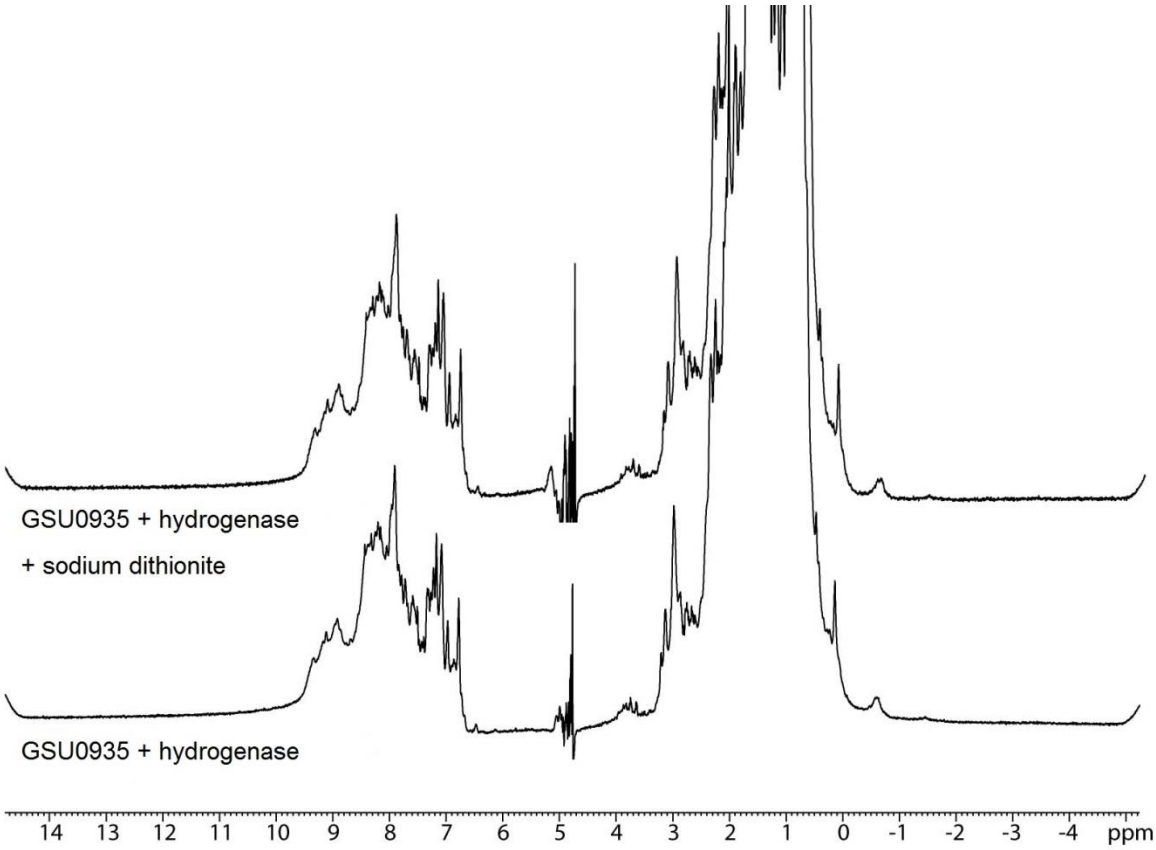

Figure 3.5 – 1D-^{1}H-NMR spectra of 8%D_2O/$^{2}H_2O$ reduced sample of GSU0935 sensor domain at pH 7.4. The reduction was achieved in the presence of catalytic amounts of hydrogenase from *D. vulgaris* (Hildenborough) under a H_2 atmosphere (bottom) or with sodium dithionite (top).

The heme proton resonances of the sensor proteins were assigned following the strategy previously described by Keller and Wüthrich for the horse heart ferrocytochrome [184] and applied later to multiheme ferrocytochromes by David Turner *et al*. [177]. The connectivities that are explored in the 2D-^{1}H NOESY and 2D-^{1}H TOCSY NMR spectra are depicted in Figure 3.6.

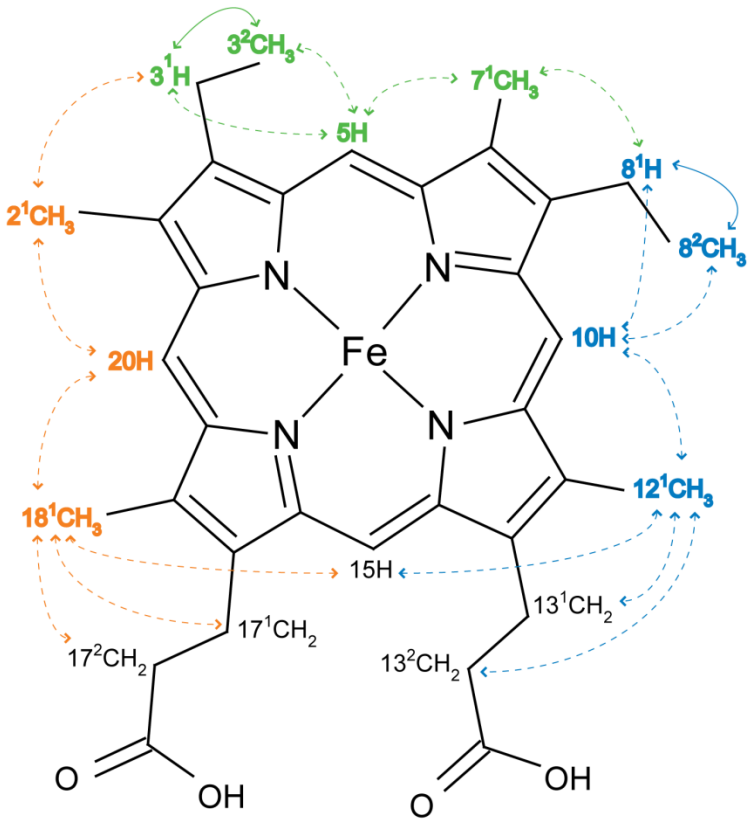

Figure 3.6 – Connectivities observed between the heme proton signals in 2D-^{1}H TOCSY (solid lines) and in 2D-^{1}H NOESY and 2D-^{1}H TOCSY (dashed lines).

In the 2D-^{1}H TOCSY NMR spectra the signals corresponding to the thioether pairs 3^1H/3^2CH$_3$ and 8^2CH$_3$/8^1H can be easily identified as their signals appear in very typical regions (Figure 3.7).

In the 2D-^{1}H NOESY NMR spectra with shorter mixing time characteristic patterns can be observed: 20H protons are connected to two methyl groups, 15H protons are not connected to any methyl or thioether groups, and 10H and 5H are connected to one methyl group and one thioether pair. This last ambiguity is overcome by analyzing connectivities between 2^1CH$_3$ and 3^1H, and between 7^1CH$_3$ and 8^1H signals. 15H protons are identified by connectivities to the methyl groups 12^1CH$_3$, and 18^1CH$_3$ at longer mixing times (Figure 3.8).

The assignment of the heme proton signals of GSU0582 and GSU0935 are indicated in Table 3.1.

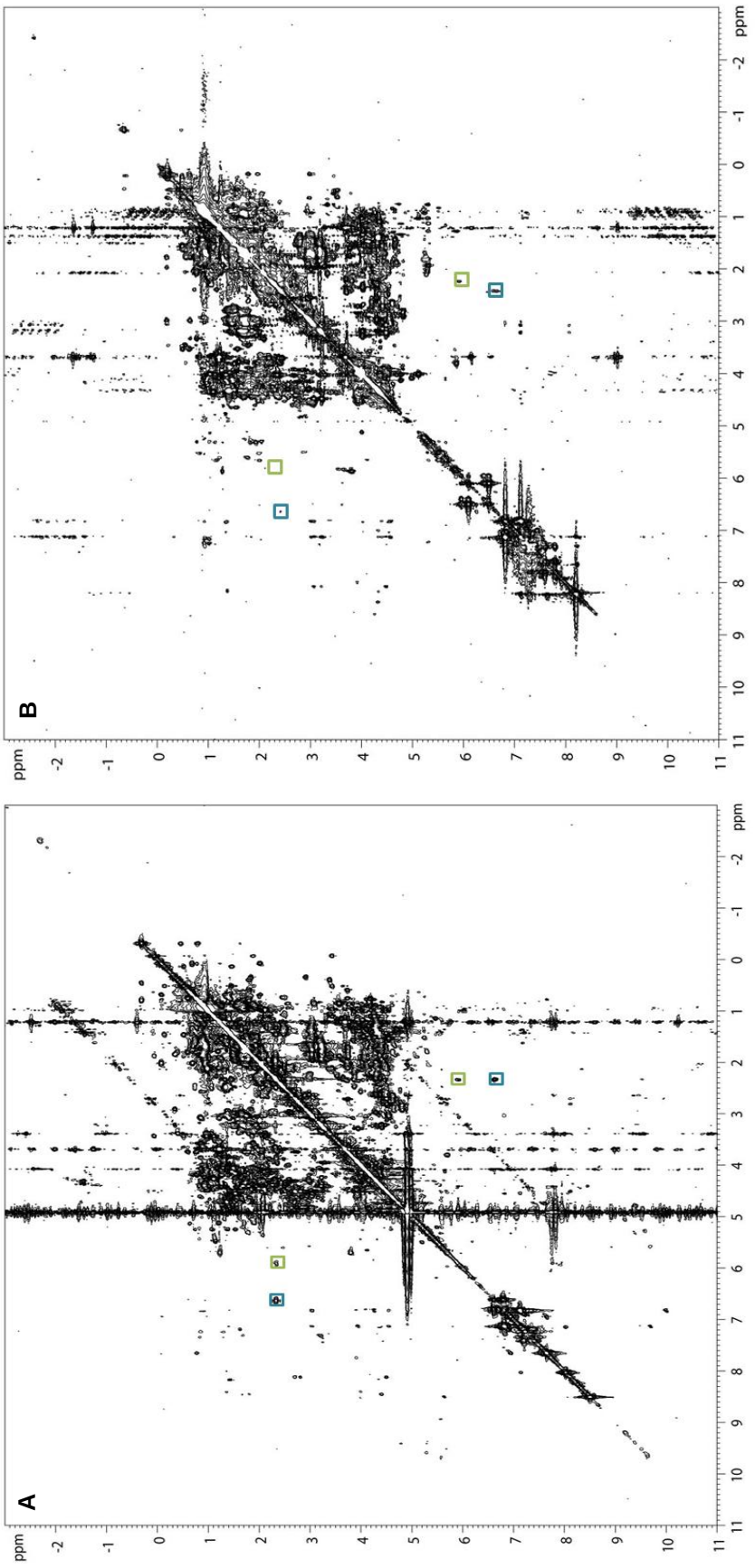

Figure 3.7 – 2D-^{1}H-TOCSY of GSU0582 (A) and GSU0935 (B) sensor domains with 60 ms mixing-time at pH 8.0 and 16 ºC. The proton signals corresponding to heme thioether pairs are boxed.

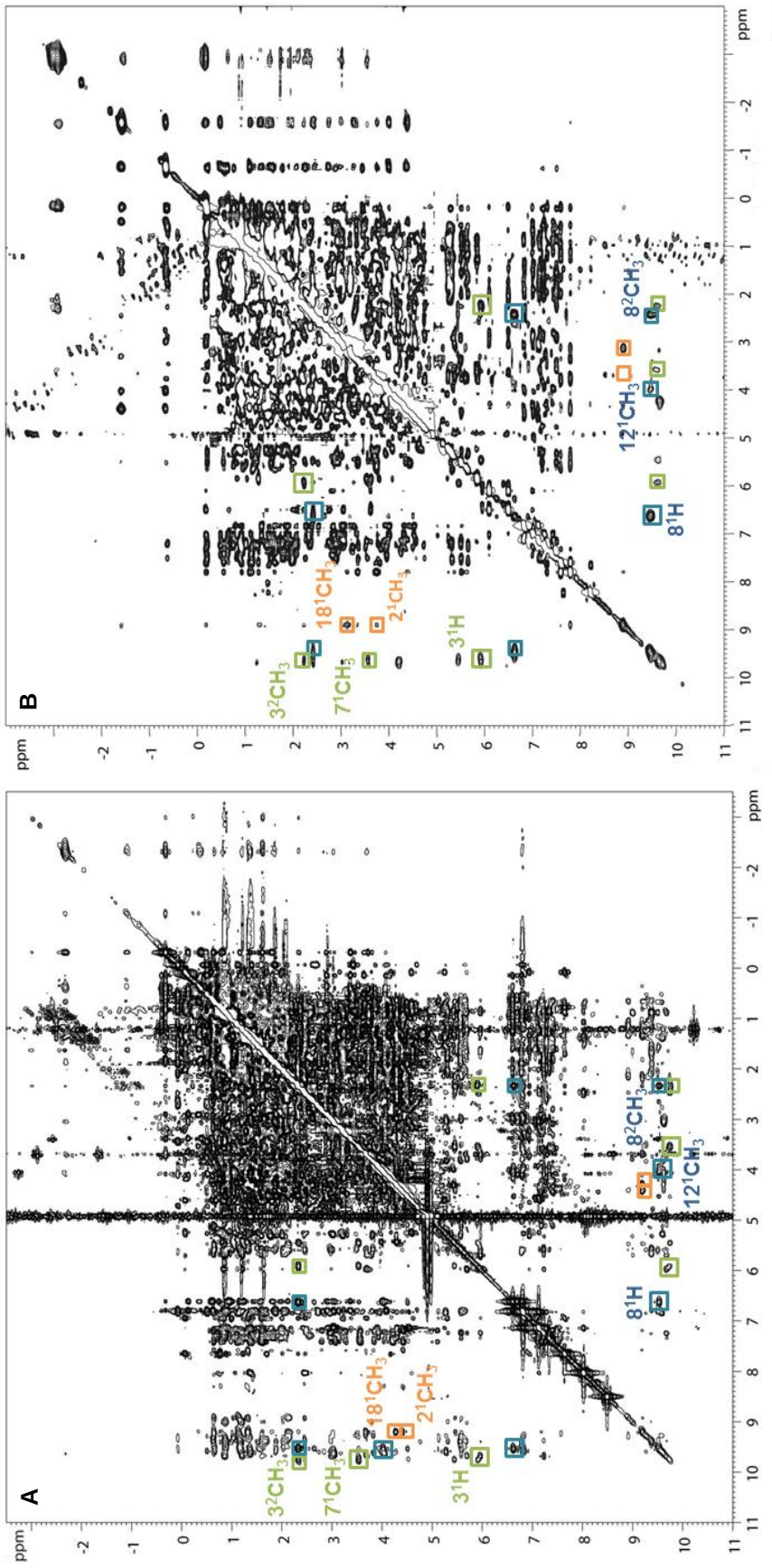

Figure 3.8 – 2D-^{1}H-NOESY spectrum of GSU0582 (A) and GSU0935 (B) sensor domains with 150 ms mixing-time at pH 8.0 and 16 ºC. The heme proton signals are labelled accordingly with the IUPAC-IUB nomenclature.

Table 3.1 – Chemical shifts (ppm) of the heme protons of and GSU0582 and GSU0935 sensor domains in the reduced state at pH 8.0 and 16 ºC. The unassigned resonances are indicated by "-".

GSU0582 heme substituent	Heme I	GSU0935 heme substituent	Heme I
5H	9.75	5H	9.63
10H	9.54	10H	9.45
15H	-	15H	-
20H	9.20	20H	8.90
2^1CH_3	4.29	2^1CH_3	3.76
7^1CH_3	3.55	7^1CH_3	3.57
12^1CH_3	4.04	12^1CH_3	3.98
18^1CH_3	4.42	18^1CH_3	3.12
3^1H	5.92	3^1H	5.94
8^1H	6.63	8^1H	6.63
3^2CH_3	2.34	3^2CH_3	2.24
8^2CH_3	2.34	8^2CH_3	2.43

As expected, the chemical shifts are observed in the typical regions for a diamagnetic *c*-type heme.

A closer inspection of the 2D-^{1}H-NOESY spectrum (Figure 3.8) shows a slight broadness of some NOE signals, which might suggest the presence of more than one conformation in solution. In order to investigate this, a less crowded region of the spectra that contains the ^{1}H signals of the axial methionine side chain was analyzed in detail. The NMR features of these signals includes a three-proton intensity peak at approximately -3 ppm and up to four resolved one-proton intensity peaks in the low-frequency region of the spectrum. The chemical shifts of methionine side chain protons are extremely sensitive to any change in the heme environment making NMR the most suitable technique to probe any slight difference in the environment of heme axial methionine, and thus of the heme environment in solution. Expansions of the 1D ^{1}H-NMR spectra obtained for heme sensor GSU0935 at different protein concentration showed that the heme environment is nearly identical since only set of signals is observed (Figure 3.9).

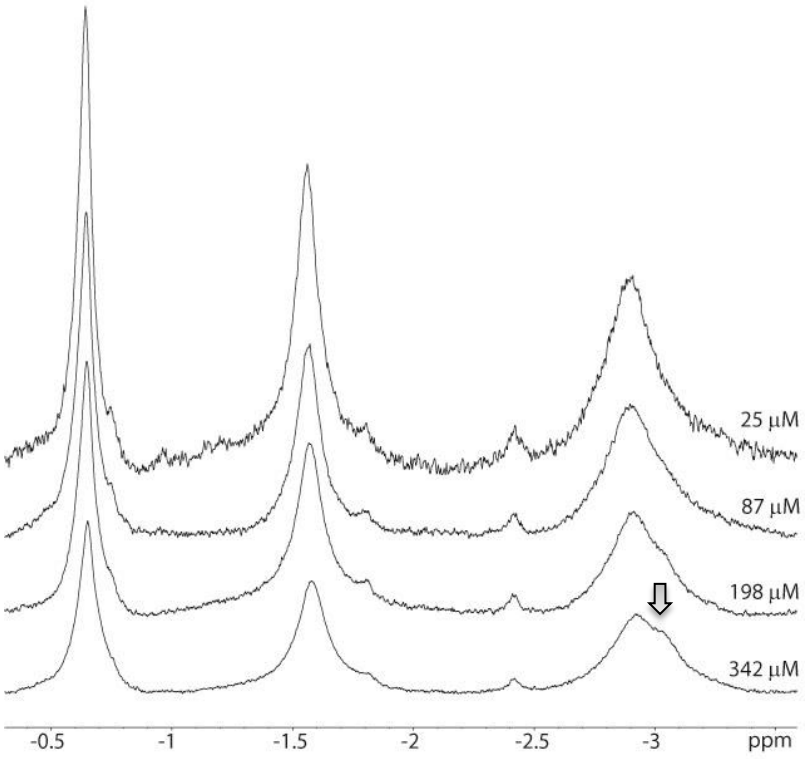

Figure 3.9 – Expansion of the high field region of 1D-^{1}H NMR spectra acquired with different concentration of GSU0935 sensor domain. The arrow points to the shoulder of the signal at approximately 3 ppm whose intensity decreases at lower protein concentrations.

However, it is noticeable that the signal at -2.93 ppm, correspondent to ε-CH_3 group of the axial methionine, shows one shoulder whose intensity decreases at diluted solutions (25 μM). The signal at -2.93 ppm is attributed to the ε-CH_3 group of the axial methionine in the monomer and the shoulder to the ε-CH_3 group of the axial methionine in the dimer. Also for heme sensor GSU0582 it is visible a shoulder on the signal correspondent to ε-CH_3 group of the axial methionine that suggests the presence of two different conformation in solution (Figure 3.9). The two different conformations presented by the protein represent an extra challenge on spectra analysis since it is not possible to assign uniquivocally the signals of each conformation.

The change in the heme environment and the existence of two different conformations in solution, can also occur at the level of the polypeptide chain. Since the sensor domain GSU0582 showed a higher tendency to precipitate, GSU0935 sensor domain was used to evaluate the existence of different conformations in solution at the level protein backbone signals.

The ^{1}H-^{15}N and ^{1}H-^{13}C HSQC spectra of the ^{13}C/^{15}N labeled GSU0935 sensor domain at different temperature (5 ºC and 25 ºC) and ionic strength (100 and 574 mM) values are indicated in Figure 3.10.

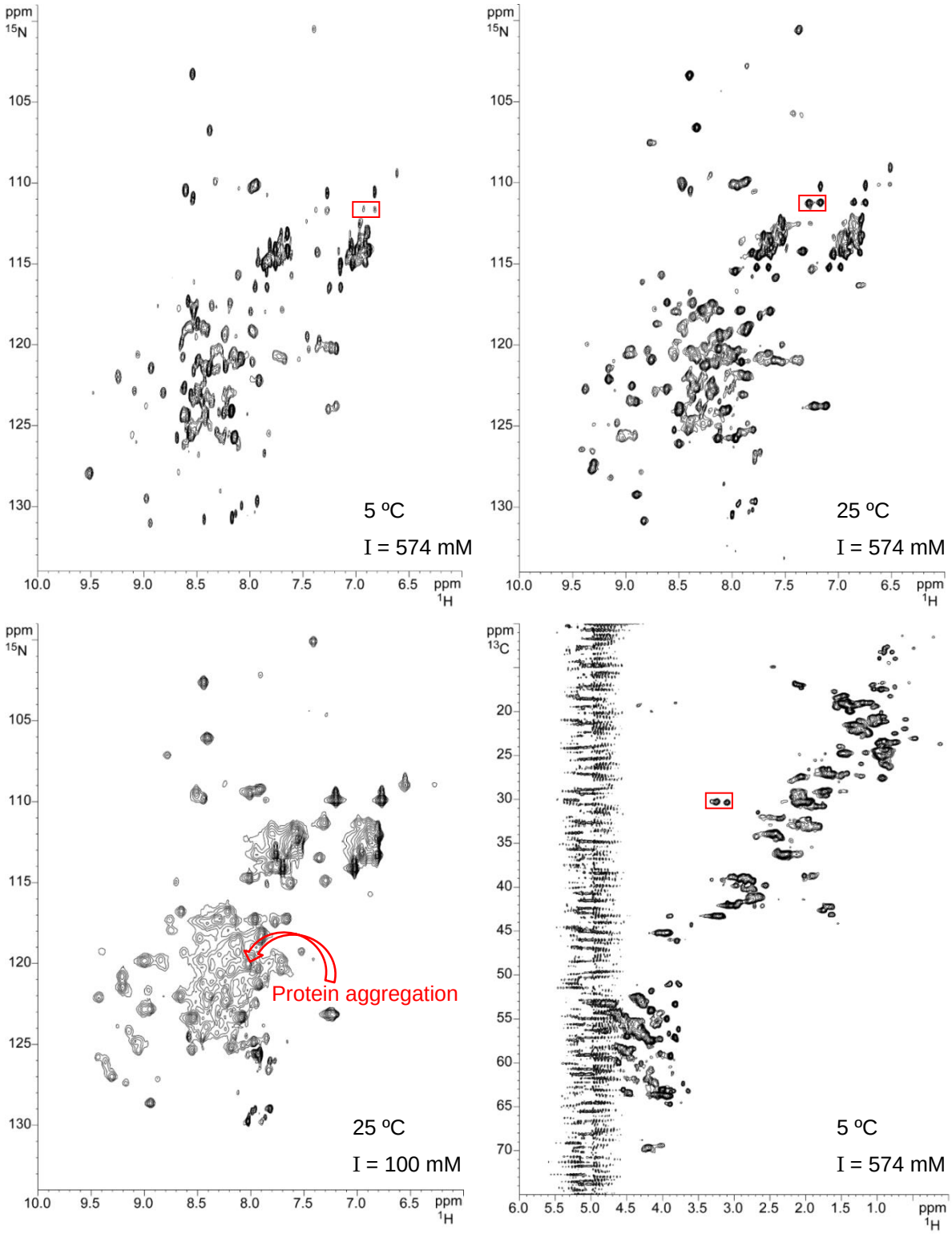
ppm
15N
105
110
115
120
125
130
10.0
9.5
9.0
8.5
8.0
7.5
7.0
6.5
ppm
1H
5 ºC
I = 574 mM
25 ºC
I = 574 mM
Protein aggregation
25 ºC
I = 100 mM
ppm
13C
20
25
30
35
40
45
50
55
60
65
70
6.0
5.5
5.0
4.5
4.0
3.5
3.0
2.5
2.0
1.5
1.0
5 ºC
I = 574 mM

(continued)

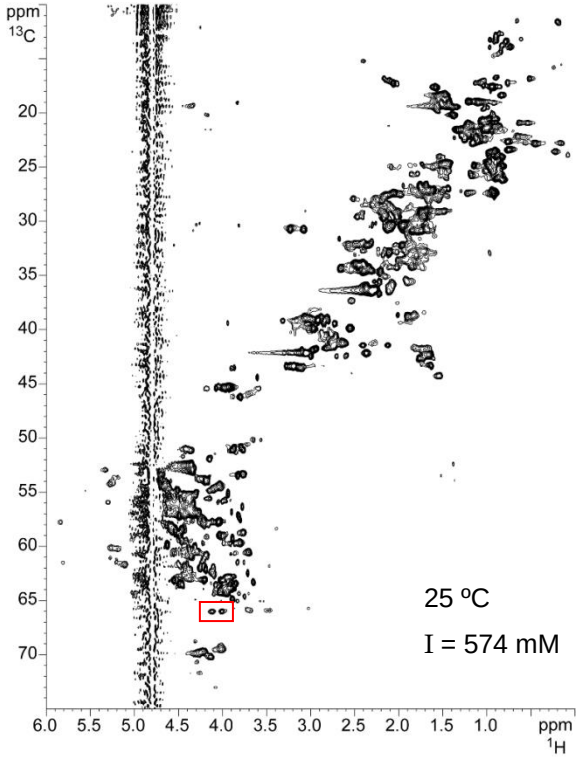

Figure 3.10 – ^{1}H-^{15}N and ^{1}H-^{13}C NMR spectra of sensor domain GSU0935 acquired at pH 7.0, different temperatures (5 °C and 25 °C) and ionic strength (100 and 574 mM). Boxed are examples of double signals and arrow points for putative protein aggregation signals.

The spectra showed unequivocally that GSU0935 sample was successfully labeled and the dispersion of NH in ^{1}H-^{15}N HSQC spectra indicate that the protein is folded. However, the data evidenced partial protein aggregation and the presence of two conformations as evidenced by the presence of several double signals. Attempts to overcome this problem by changing the ionic strength and temperatures values were promising but so far unsuccessful and prevented further structural studies of GSU0935 sensor domain.

3.5 Conclusions

The signal transduction pathways of heme-containing MCP proteins from *Geobacter sulfurreducens* must involve important conformational changes in the vicinity of the heme located at the sensorial domain of these proteins. This Chapter describes the efforts undertaken to monitor such changes in the heme sensor domains GSU0582 and GSU0935 from *G. sulfurreducens*, using NMR spectroscopy. The high-spin state of the heme iron of both sensor domains in the fully oxidized form and the parallel broadness of the NMR signals implied that detailed NMR studies must be carried out in the reduced form of the proteins. However, at the sample concentration required for NMR studies, the presence of multiple conformations in solution could not be completely overcome and prevented the full achievement of our main goal. Nonetheless, important steps were taken, which included the isotopic labeling of the proteins and the assignment of their heme substituents in the reduced form. The latter, constitutes the foundation for future studies once the complete assignment of the polypeptide signals is accomplished. This would allow the identification of the conformational changes in the heme sensor domains GSU0582 and GSU0935.

CHAPTER 4

FOLDING MODULATES THE SWAPPED DIMERIZATION MECHANISM OF CHEMOTAXIS HEME SENSORS GSU0582 AND GSU0935 FROM *G. SULFURREDUCENS*

RESULTS PUBLISHED IN:

M.A. Silva, T.G. Lucas, C.A. Salgueiro, C.M. Gomes, Protein folding modulates the swapped dimerization mechanism of methyl-accepting chemotaxis heme sensors, Plos One, 7 (2012) e46328.

4. FOLDING MODULATES THE SWAPPED DIMERIZATION MECHANISM OF CHEMOTAXIS HEME SENSORS GSU0582 AND GSU0935 FROM *G. SULFURREDUCENS*

4.1 Abstract

The crystal structures of the periplasmic sensor domains GSU0582 and GSU0935 from *G. sulfurreducens* revealed that these domains form swapped dimers with a PAS-like fold formed from the two protein chains. The swapped dimerization of these sensors is related to the mechanism of signal transduction and the formation of the swapped dimer involves significant folding changes and conformational rearrangements within each monomeric component. However, the structural changes occurring during this process are poorly understood and lack a mechanistic framework. To address this issue, it was studied the folding and stability properties of the two distinct heme-sensor PAS domains, using biophysical spectroscopies.

It was observed substantial differences in the thermodynamic stability (ΔG = 14.6 kJ.mol^{-1} for GSU0935 and ΔG = 26.3 kJ.mol^{-1} for GSU0582) and also demonstrated that the heme moiety undergoes conformational changes that match those occurring at the global protein structure. This indicates that sensing by the heme cofactor induces conformational changes that rapidly propagate to the protein structure, an effect which is directly linked to the signal transduction mechanism. Interestingly, the two analyzed proteins have distinct levels of intrinsic disorder (25% for GSU0935 and 13% for GSU0582), which correlate with conformational stability differences. This provides evidence that the sensing threshold and intensity of the propagated allosteric effect is linked to the stability of the PAS-fold, as this property modulates domain swapping and dimerization. Analysis of the PAS-domain shows that disorder segments are found either at the hinge region that controls helix motions or in connecting segments of the β-sheet interface. The latter is known to be widely involved in both intra- and intermolecular interactions, supporting the view that its folding and stability are at the basis of the specificity and regulation of many types of PAS-containing signaling proteins.

4.2 Introduction

Folding properties of GSU0582 and GSU0935 sensor domains

As described in Chapter 1 of this Thesis, the signaling systems are characterized by a highly modular design that has been adapted and integrated into a wide variety of cellular signaling circuits [20, 185]. These signal transducers couple a regulatory heme-binding domain (sensor domain) to a neighboring transmitter (transduction domain). The more common heme based sensors contain a *b*-type heme in the sensor domain, which is used to bind effector molecules such as O_2, NO, or CO [186]. The binding of the effector molecule to the sensor domain induces a conformational change in the transduction domain that is responsible for the generation of the intracellular signal and subsequent regulation of the physiological function [186-189]. *G. sulfurreducens* bacterium has a large number of chemotaxis genes including 35 methyl-accepting chemotaxis proteins. Indeed, two of these proteins have one heme *c*-binding motif [150], a characteristic only reported for the DcrA sensor from *D.vulgaris* [149, 190]. They are part of proteins annotated as two-component signal transduction or chemotaxis proteins, and have homologs in the *Geobacteraceae* family [115]. The structures of GSU0582 and GSU0935 heme sensors (Figure 1.14) are the first representatives of a new class of heme sensors since all other heme-containing PAS sensor domains described in the literature are formed by a single polypeptide chain, located at the cytoplasm and contain *b*-type hemes [191]. The spectroscopic properties of sensor domains GSU0582 and GSU0935 in solution were also addressed by using a set of complementary spectroscopic techniques [115, 168] suggesting that the sensor domains GSU0935 and GSU0582 might use the *c*-type heme for trigger the signal transduction mechanism recognition in a process that involves the formation of the swapped dimer at periplasm with the concomitant alteration of the relative positions of the transmembrane helices and response of the transducers domains in the cytoplasm. In this study, the conformation and folding properties of two distinct heme sensor PAS domains' were investigated in order to determine how folding modulates dimer formation and how the changes in the heme environment propagate to the global structure. The findings suggest that differences in the thermodynamic stability and intrinsic disorder of the two sensors not only directly modulate local unfolding events that lead to swapped dimer formation, but are at the basis of distinct signaling properties and activation thresholds within heme sensor homologues.

4.3 Materials and Methods

4.3.1 Basic principles of circular dichroism

Since the late 1980s, there has been an explosive growth in structural biology with the number of high resolution structures of proteins added to the Protein Data Bank (PDB). However, there is a growing realization of the need to perform structural studies under the conditions in which proteins actually operate (generally in solution) and to provide measures of the proteins structural changes rates that are often essential to their biological function. Circular dichroism (CD) has become increasingly recognized as a valuable structural technique for addressing these issues. Briefly, circular dichroism refers to the differential absorption of the left-handed and right-handed circularly polarized components of plane-polarized electromagnetic radiation. The CD spectra are obtained when the dichroism is measured as a function of wavelength by spectropolarimeters.

This technique is an excellent method for rapidly evaluate the protein secondary and tertiary structures, the conformational changes due to the binding of ligands or presence of denaturing agents and also to elucidate a number of aspects of protein folding and unfolding. In addition, CD can be used to study other biological chromophores, such as cofactors or nucleic acids [192]. This effect will occur when an absorbing group is optically active for one or more of the following reasons: i) it is intrinsically chiral because of its structure (for example, a carbon atom with 4 different substituents) or due to the presence of disulphide bond, which is chiral because of the dihedral angles made by the C–S–S–C atom chain, ii) it is covalently linked to a chiral center in the molecule, or iii) it is placed in an asymmetric environment caused by the 3-dimensional structure of the molecule [193]. In the CD experiment, plane-polarized radiation is split into its circularly polarized components by passage through a modulator. The modulator transmits each of the components in turn. If, after passage through the sample of interest, the left and right-handed components are not absorbed or are absorbed to equal extents, the recombination of left and right-handed would regenerate radiation polarized in the original plane. However, if left and right-handed are absorbed to different extents, the resulting radiation would be said to possess elliptical polarisation (Figure 4.1) [194].

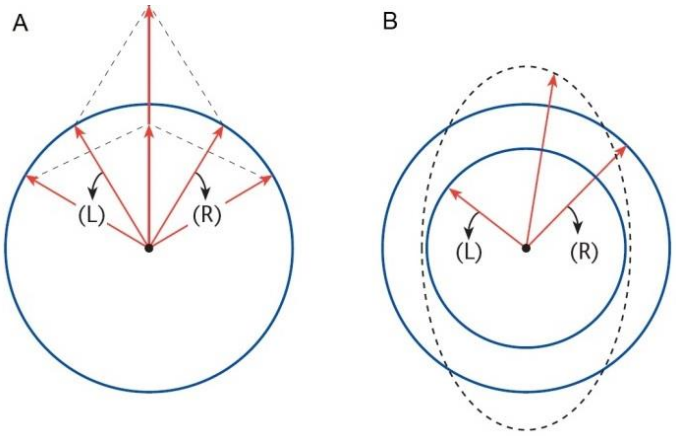

Figure 4.1 – Origin of the CD effect. The left- (L) and right- (R) circularly polarized components of plane-polarized radiation: (A) the two components have the same amplitude and when combined generate plane-polarized radiation and (B) the components are of different magnitude and the resultant (dashed line) is elliptically polarized. Reproduced from [192].

The result is that different structural elements have characteristic CD spectra (Figure 4.2).

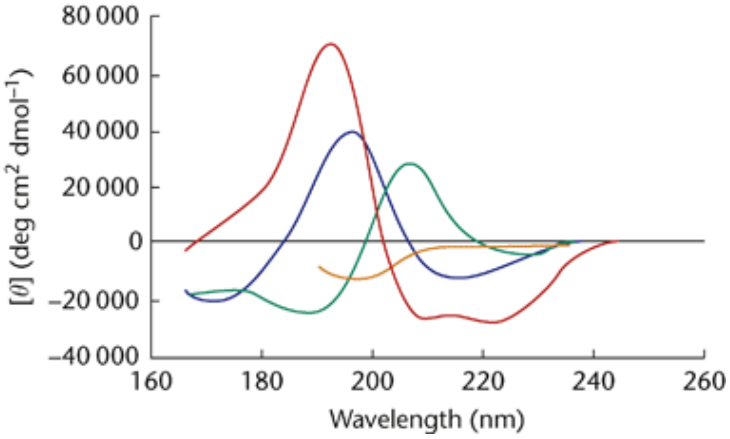

Figure 4.2 – Far-UV CD spectra associated with various types of secondary structure in proteins. Red, α helix; blue, antiparallel β sheet; green, type I β turn and orange, irregular structure. Reproduced from [192].

In proteins, the chromophores of interest include the peptide bond (absorption below 240 nm), aromatic amino acid side chains (absorption in near-UV region in the range 250 to 320 nm and in far-UV region in the range 180 to 250 nm) and disulphide bonds (weak broad absorption bands centered around 260 nm). In addition, non-protein cofactors can absorb over a wide spectral range [195], including pyridoxal-5′-phosphate around 330 nm, flavins in the range 300 nm to 500 nm (depending on oxidation state), heme groups strongly around 410 nm with other bands in the range from 350 nm to 650 nm (depending on spin state and coordination of the central Fe ion) and

chlorophyll moieties in the visible and near infrared regions. Finally, induced CD signals can arise from ligands, which have no intrinsic chirality but acquire chirality when bound in an asymmetric environment such as provided by a protein [193].

For example, α-helical proteins have negative bands at 222 nm and 208 nm and a positive band at 193 nm [196]. Proteins with well-defined antiparallel β-pleated sheets (β-helices) have negative bands at 218 nm and positive bands at 195 nm [197], while disordered proteins have very low ellipticity above 210 nm and negative bands near 195 nm [198]. The collagens are a unique class of proteins, which have three chains that wrap together in a triple helix. Each strand has a conformation resembling that of poly-L-proline [199] in a extended helical conformation where all of the bonds are trans to each other.

Because the spectra of proteins are so dependent on their conformation, CD can be used to estimate the structure of unknown proteins and monitor conformational changes caused by temperature, mutations, denaturants or binding interactions. Therefore, structural, kinetic and thermodynamic information can be derived from circular dichroism spectroscopy.

4.3.2 Disorder and structural analysis

The experimental structures of sensors GSU0582 and GSU0935 were retrieved from the PDB; the model of the GSU0935 constructed monomer as published in [115] was a kind gift from Drs. Marianne Schiffer and Raj Pokkuluri (Argonne National Laboratory, USA). Protein structure analysis was carried out using the WhatIF web server and structural models represented using Pymol. The DisProt analysis server for intrinsically disordered protein regions (http://www.dabi.temple.edu/disprot/predictor.php) using the VL3H neural network based Predictor [200] was employed to inspect the sequences for disordered segments.

4.3.3 Spectroscopic methods

Circular dichroism measurements were performed at 222 nm using a JASCO J-810 spectropolarimeter with a Peltier thermostated cell support using 0.1 cm path-length cell quartz. UV-visible spectra were recorded with a Shimadzu UVPC-1700 spectrometer at room temperature using a 1 cm path-length cell quartz cell.

4.3.4 Analytical size-exclusion chromatography

Size-exclusion chromatography experiments were performed on an analytical-scale Superdex-75 XK-16 (V_t = 124 mL) column attached to Akta Prime HPLC system. The column was preequilibrated with 20 mM Tris-HCl pH 7.5 and 150 mM NaCl and calibrated with the following molecular mass standards: bovine serum albumin (67 kDa), ovalbumin (43 kDa), chymotrypsinogen A (25 kDa), cytochrome *c* (12.5 kDa). The partition coefficient (K_{av}) was determined from equation $K_{av} = \frac{V_e - V_0}{V_t - V_0}$ where V_e is the elution volume for the protein, V_t is the total bed volume and V_0 the column void volume. Imidazole and the blue dextran 2000 were used to determine V_t and V_0, respectively. In order to monitor the changes in the monomer-dimer equilibrium, sensor samples with a final concentration of 1; 2; and 3 mg.mL^{-1} were prepared and 100 µl aliquot from each sample were injected separately into the column. The runs were performed at a flow rate of 0.5 mL.min^{-1} and protein elution monitored at 280 nm.

4.3.5 Equilibrium unfolding experiments

The conformational stability of the heme sensors GSU0582 and GSU0935 was assessed by performing temperature and chemical induced denaturations, monitored by far-UV CD at 222 nm, which reports on the stability of the secondary structural elements (α-helices and β-sheets) and UV-visible absorption spectroscopy (to analyze the heme moiety). Protein solutions (0.2 mg.mL^{-1}) were prepared in a 20 mM sodium phosphate buffer at different pH values covering the range 4–10. For thermal-induced denaturation, a heating rate of 1.0 ºC.min^{-1} was used, and temperature was increased from 10 ºC to 90 ºC. Chemical-induced denaturation experiments were carried out with several concentrations of GuHCl (in the range 0-4 M) or urea (in the range 0-9 M) at room temperature using CD and UV-visible spectroscopy. Fresh guanidinium hydrochloride (GuHCl) and urea solutions were used and their rigorous concentrations were determined from refractive index measurements. The reaction mixture was incubated for 2 h at room temperature for complete chemical denaturation. The fraction of unfolded protein (f_U) was monitored by CD spectroscopy at defined denaturant concentration or temperature and calculated according to the expression $f_U = \frac{\theta_N - \theta}{\theta_N - \theta_U}$ with θ_N being the ellipticity at 222 nm of the protein in the native folded state, θ the ellipticity at defined denaturant concentration or temperature, and θ_U being the ellipticity at 222 nm of the completely unfolded state. The f_U was also monitored by UV-visible spectroscopy at defined denaturant concentration and calculated from the absorbance of the Soret peak at 401 nm

according to the expression $f_U = \frac{A_N - A}{A_N - A_U}$ with A_N representing the absorbance of the native state, A the absorbance at each intermediate concentration of denaturant, and A_U the absorbance of the completely unfolded state.

4.3.6 Analysis of the thermodynamic data

The GuHCl and urea unfolding transition curves for the sensors were analyzed assuming a two-state transition: $N \rightarrow U$ where N and U represent the native and unfolded protein, respectively. The fraction of unfolded sensor, f_U, is calculated from the relationship: $f_N + f_U = 1$, where f_N and f_U represent the protein fraction in folded and unfolded conformation, respectively. Therefore, the equilibrium constant between the unfolded and native state is given by $K = \frac{[U]}{[N]} = \frac{f_U}{(1-f_U)}$ and is related to the standard free enthalpy of denaturation according to $\Delta G^0 = -R\,T\,ln\,K$, where R is the universal gas constant (8.31 J.K^{-1}.mol^{-1}) and T is the absolute temperature. In order to estimate the conformational stability ($\Delta G_U^{H_2O}$) of the sensors, it was assumed that the linear dependence of the free energy of unfolding with the concentration of the denaturant continued to zero concentration [201] $\Delta G_U^0 = \Delta G_U^{H_2O} - m\,[denaturant]$ where $\Delta G_U^{H_2O}$ is the value of standard free enthalpy at zero concentration of denaturant (i.e. the conformational stability of a protein) and m reflects the effectiveness of the denaturant in unfolding the protein [202, 203].

4.4 Results and Discussion

4.4.1 Studies of the monomer-dimer equilibrium

The heme sensor PAS domain undergoes dimerization in the methyl-accepting chemotaxis protein complex. This step is believed to be crucial in the signal transduction process and the formation of the domain swapped dimer likely involves significant folding changes and conformational rearrangements. It was thus carried out a study to warrant that at the concentrations used in the conformational stability studies, the monomer-dimer equilibrium is shifted towards the monomeric form. Indeed this was the case, as verified by using size-exclusion chromatography experiments which showed that at working protein concentrations (typically < 0.2 mg.mL^{-1}) both sensor proteins eluted with estimated masses around 19 kDa, close to those calculated for the

monomers (~ 16 kDa). Both sensors yielded similar results and those obtained for heme sensor GSU0935 are indicated as an example (Figure 4.3).

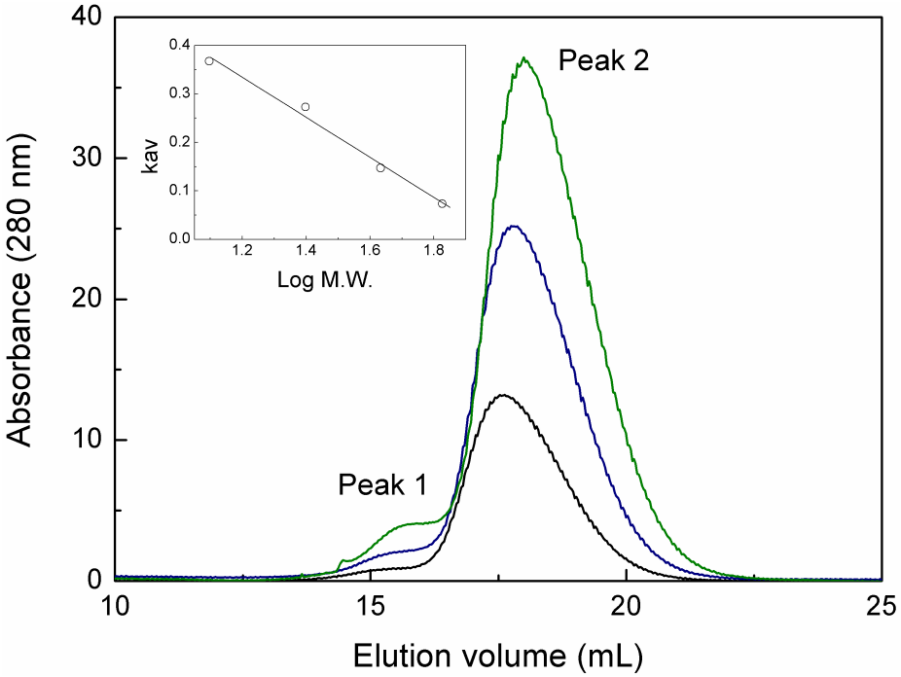

Figure 4.3 – Analytical gel filtration profiles of sensor GSU0935 on a calibrated Superdex-75 XK-16 column at different concentrations: 1 mg/mL (black line); 2 mg/mL (blue line) and 3 mg/mL (green line). The first and second peaks were eluted with volumes of 16 mL and 19 mL, corresponding to molecular weights of 38 kDa (dimer) and 19 kDa (monomer), respectively. The inset shows the calibration curve of gel phase distribution coefficient (k_{av}) *versus* log molecular weight (MW) of standard proteins.

4.4.2 Definition of independent conformation fingerprints for heme moiety and protein conformation

The next step was the establishment of the fingerprints corresponding to the native and unfolded conformers for the two spectroscopic methods selected for structural analysis: far-UV circular dichroism and visible absorption. This combination of methodologies allows monitoring independently effects on the secondary structure (far-UV CD) and heme moiety (visible absorption) during protein unfolding experiments. This will allow us to address the following questions: how do the conformational changes on the heme sensor triggered upon signaling events such as redox changes or ligand binding propagating to the PAS domain? Are structural changes within the heme environment propagating to the rest of the protein, or rather become locally restricted? This has obvious implications on the understanding on the influence over the mechanism of dimer

interaction. The far-UV CD spectra of the two sensor PAS proteins GSU0935 and GSU0582 are identical and can be typified by that of GSU0935 (Figure 4.4A). In the native state the spectra are typical of well folded α/β proteins, featuring an intense negative band with a shoulder at 208 nm and a broader component around 222 nm (Figure 4.4A, solid line). Protein unfolding results in a substantial loss of secondary structure as evidenced by a decrease in the 222 nm signal and conversion into a random coil, as reported by the emerging negative band at 208 nm (Figure 4.4A, dotted line).

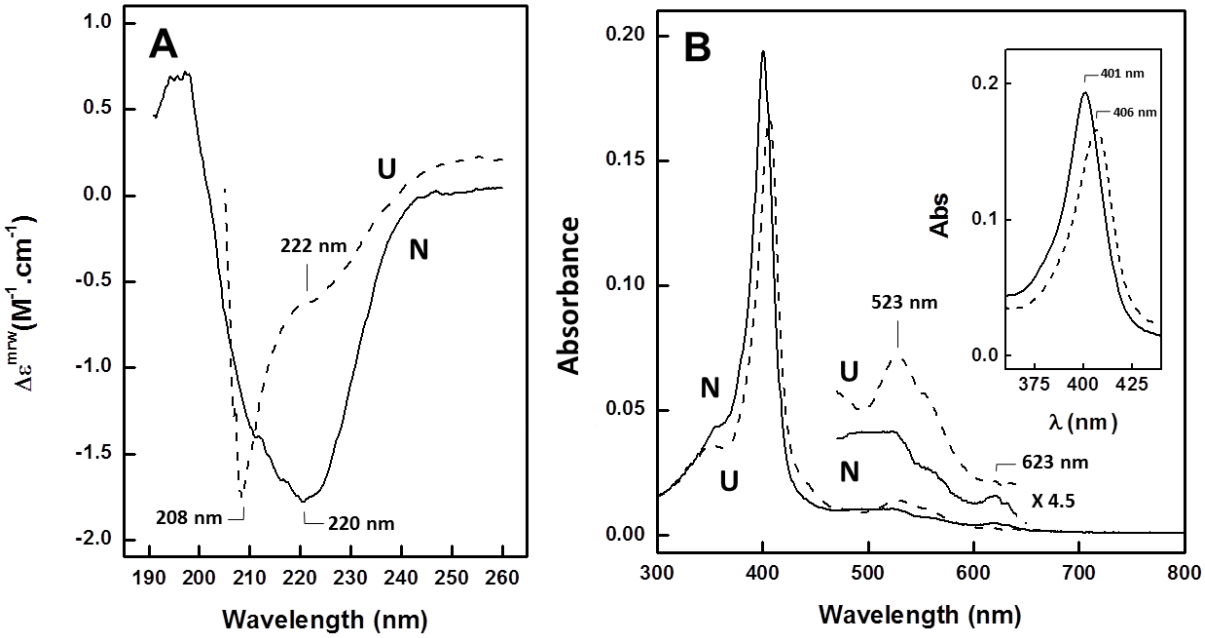

Figure 4.4 – Spectroscopic characterization of GSU0935 sensor domain conformers. Far-UV CD (A) and UV-visible absorption (B) spectra of the GSU0935 sensor in the native (N, solid lines) and in 6 M urea unfolded state (U, dashed lines).

The UV-visible spectroscopic signatures of the *c*-type heme of the two sensors allowed probing the conformational stability at the heme moiety and, thus, complementing the CD protein structural information. The electronic absorption maxima of native heme sensors is also overlapping, featuring in the oxidized form a Soret band at 401 nm and weak bands in the 490-523 nm and 623 nm regions (Figure 4.4B, solid line). Upon unfolding of the sensors, the covalently-bound heme group remains attached to the polypeptide chain even at high concentration of denaturants, and the differences in the UV-visible spectroscopic features indicate that the heme group is a good reporter for conformational changes within the neighboring polypeptide chain. The

Soret peak shifts to 406 nm and its intensity slightly decreases, whereas the 523/623 nm ratio increases (Figure 4.4B, dotted line and inset).

Indeed, non-covalently bound heme proteins lose their heme group upon denaturation with a concomitant and significant shift of the Soret peak maximum to ~ 365 nm [204], which is not observed in this case. It was also noticed that both thermal and chemical unfolding are reversible, as the far-UV CD and visible absorption fingerprints corresponding to the native conformers are restored upon removal of the destabilizing condition. This allows a thermodynamic analysis of the reaction, as the system reacts under equilibrium conditions: this is not always the case among metallo proteins which frequently unfold irreversibility either due to loss or deficient reintegration of the metal cofactor upon refolding [205-209], although other cytochromes also undergo reversible unfolding [210]. Overall, the spectroscopic analysis of the PAS-like sensor native and unfolded conformers shows that i) heme and secondary structure changes can be independently monitored as conformational probes and ii) the reversibility of the unfolding reaction allows a quantitative thermodynamic analysis of the folding properties of both proteins. The latter is determinant for understanding mechanistic differences between the different heme sensor domains.

4.4.3 Conformational coupling between the heme moiety and the protein fold

The conformational stability of PAS-like heme sensors was investigated from equilibrium unfolding with the chaotropic denaturants urea and guanidinium hydrochloride at pH 8.0. For both GSU0935 and GSU0582, the far-UV CD spectra denoted a gradual decrease in the ellipticity at increasing concentrations of denaturants, indicative of a gradual loss of secondary structure and formation of unstructured conformations. This transition was followed monitoring the variation of the CD signal at 222 nm, a wavelength at which both α-helices and β-sheets contribute significantly (Figure 4.5A, solid symbols).

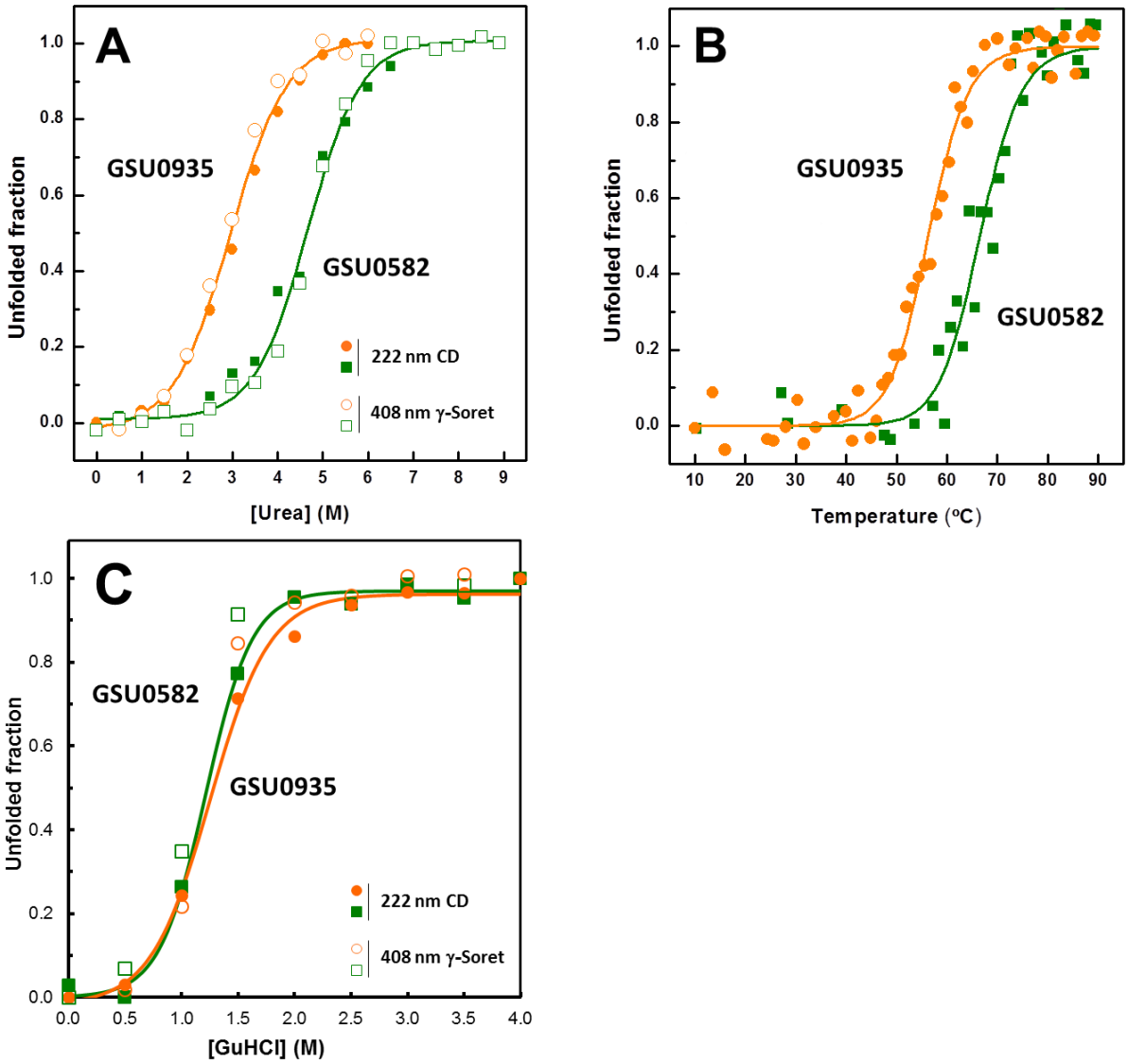

Figure 4.5 – Conformational stability of the protein sensors. Chemical denaturation by urea (A), chemical denaturation by GuHCl (B) and thermal denaturation (C). Solid symbols represent the transition monitoring the variation of the CD signal at 222 nm and void symbols represent the transition monitoring the variation of the UV-visible signal at 408 nm. The lines represent the fitting to the two-states model.

The stability of the heme moiety was also probed upon incubation of both proteins with chemical denaturants: for both cases it is notorious that the Soret band gradually red-shifts from 401 to 406 nm, as the denaturant concentration increases (Figure 4.5A and C, void symbols). The urea and GuHCl-induced unfolding curves obtained from these two complementary spectroscopic methods show that both conformational probes report the same event; in both cases, no intermediate species were observed and the denaturation curves are characterized by a sharp transition between folded and unfolded states suggesting a two-state reaction [211, 212]. This is in

contrast to other heme proteins including peroxidases with unmodified heme *b*, like horse radish peroxidase or cytochrome *c* peroxidase, where unfolding is not a simple two-state process and thermodynamic intermediates are observed [204]. This suggests that the energetics of the PAS-like fold GSU0935 and GSU0582 proteins is intertwined with the heme cofactor in a completely distinct way in respect to other heme-containing proteins. In fact, this coupling between heme and protein equilibrium unfolding in heme sensor domais is logical considering a cause-effect signaling process.

4.4.4 PAS-heme sensors have distinct thermodynamic properties

Analysis of the chemical equilibrium unfolding data was carried out assuming a two-state equilibrium from which the thermodynamic parameters of the folding reactions for the two PAS-like heme sensors were determined (Table 4.1).

Table 4.1 – Thermodynamic parameters of denaturation of sensors GSU0935 and GSU0582 for chemical denaturation by urea and GuHCl at pH 8.0.

Denaturant	Parameter	GSU0935	GSU0582
Urea	C_m (M)	3.2 ± 0.1	4.9 ± 0.1
	m (kJ.mol^{-1}.M^{-1})	4.6 ± 0.4	5.4 ± 1.3
	ΔG (kJ.mol^{-1})	14.6 ± 0.4	26.3 ± 6.7
GuHCl	C_m (M)	1.3 ± 0.1	1.2 ± 0.1
	m (kJ.mol^{-1}.M^{-1})	13 ± 5.0	16.3 ± 5.4
	ΔG (kJ.mol^{-1})	15.9 ± 5.0	18.8 ± 6.7

As expected, lower midpoint denaturant concentrations (C_m) were obtained when GuHCl was used, in agreement with the fact that it is a stronger denaturant agent. Also, the cooperativity of the transitions for both sensor proteins is identical as indicated by the comparable *m* values. The slightly higher cooperativity of the unfolding transition observed for sensor GSU0582 indicates that the surface area exposed during denaturation is higher in this protein. The occurrence of a two-state transition in both sensors reflects the covalent bonding between the prosthetic group and the central protein core. The heme binds covalently to the polypeptide chain by the two cysteine residues and histidine from the heme binding motif CQSCH. This motif is located in the loop between strands β3 and β4 and is in proximity to the loop between two N-terminal helices α1 and α2 (Figure 4.6).

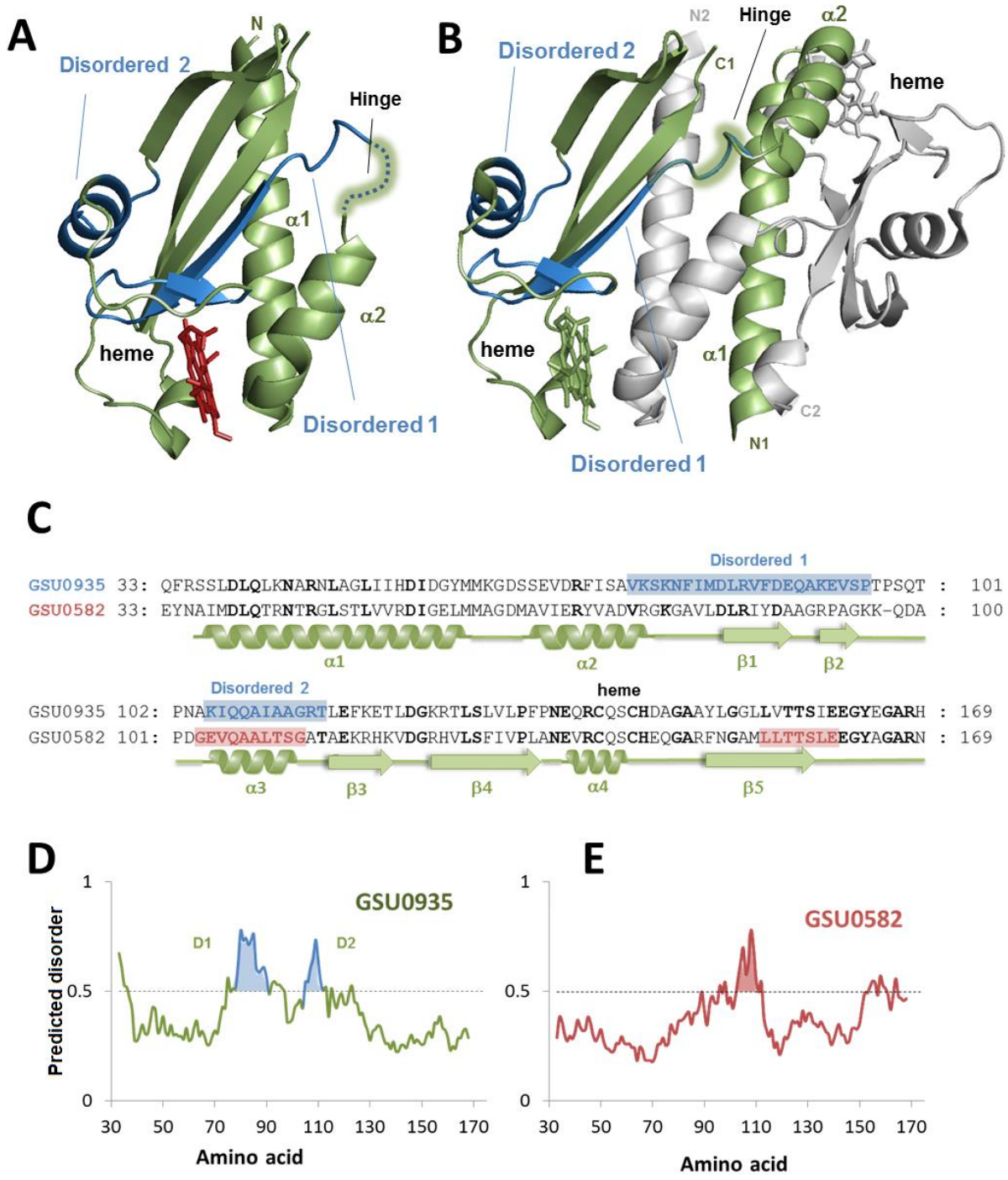

Figure 4.6 – Disordered segments in the monomer and swapped dimers in PAS-like heme sensor domains. Structure of the constructed monomer (A) and helix-swapped GSU0935 sensor dimer (B). One of the monomers is highlighted (green) and helices α1 and α2 displaced upon dimer assembly, are specifically labeled in the figures, as well as the "hinge region" through which this conformational change takes place. Analysis of the amino acid sequences of the two studied sensors (C) denotes regions of intrinsic disorder (marked in blue in the structure of GSU0935 sensor and in red in the amino acid sequence of the GSU0582). Coils and arrows denote helical (α1–α4) and strands (β1–β4) segments, respectively, and refer to the secondary structure of the crystallographic dimer. The residues that are part of the heme binding motif are bold-faced. The hinge regions in GSU0935 (KSKNFI) overlap with one of the disordered segments. The DisProt plots for intrinsic disorder prediction are shown for GSU0935 (D) and GSU0582 (E). The proteins share

a disordered segment (labeled as disordered 2) in a stretch linking the four-stranded anti-parallel β-sheet region, but the thermodynamically least stable GSU0935 sensor has an additional disordered segment that covers the hinge region (labeled as disordered 1). GSU0582 C-terminal region also presents a lower probability to display small disordered segments. N1 (C1) and N2 (C2) refer to N-terminal (C-terminal) in monomer 1 and 2, respectively.

This might explain the concerted unfolding of the heme cavity, melting of the secondary structural elements and structural disruption observed under denaturing conditions. Overall, these results indicate that the urea-mediated unfolding of both proteins is mechanistically comparable, in agreement with the fact that the two proteins have almost superimposable structures (~ 1.43 Å r.m.s.). However the two proteins have striking differences in respect to their conformational stabilities, as GSU0935 sensor is substantially less stable than GSU0582 (Table 4.1).

The characterization of temperature-induced unfolding followed by far-UV CD spectroscopy was also carried out, in order to monitor the thermal stability of the two proteins. For both sensors increasing the temperature resulted in a progressive α-helix to random coil transition (Figure 4.5B). At pH 8.0, the values of midpoint thermal unfolding or melting temperature (T_m) obtained for the two sensors are also clearly distinct: 55.8 ± 0.2 ºC and 65.9 ± 0.6 ºC for sensors GSU0935 and GSU0582, respectively. These values correlate extremely well with the chemical denaturation C_m values, which also indicated a higher stability for sensor GSU0582.

4.4.5 Electrostatic bonding contributes to differential stability of PAS-heme sensors

Although the two heme sensor domains have identical structural folds, the fact that they have different primary sequences results in the establishment of different sets of stabilizing interactions resulting in differences in conformational stability. Indeed, a number of factors influences protein stability, such as the number of hydrogen bonds, hydrophobic contacts and salts bridges, which relate to the prevalence of certain amino acid residues [213, 214]. For example, comparison of several amino acid sequences of thermophile-mesophile proteins indicate that arginine and tyrosine residues are significantly more frequent in more stable proteins, while cysteine and serine are less frequent [213]. Also, the α-helix content of glycine and alanine residues seems to contribute to protein stabilization [149, 215, 216]. It was carried out an analysis of amino acid sequences of the sensors under study (see below) and observed that the two proteins have rather different theoretical isoelectric points, being GSU0935 more acidic (pI ~ 5.9) than GSU0582 (pI ~ 7.0). It was thus investigated the role of electrostatic interactions on the stabilities of the two proteins by carrying out an analysis of the thermal stability as a function of pH. Using far-UV CD it was possible to analyze the overall protein folding and the relative secondary structure content of the proteins when poised at distinct pH vales, as well as to determine variations in the midpoint denaturation temperature (T_m). The results obtained for sensor GSU0582 evidence minor variations in the far-UV

CD spectra in the pH 6.0-9.0 range and some distortions towards the pH extremes (Figure 4.7A, Table 4.2).

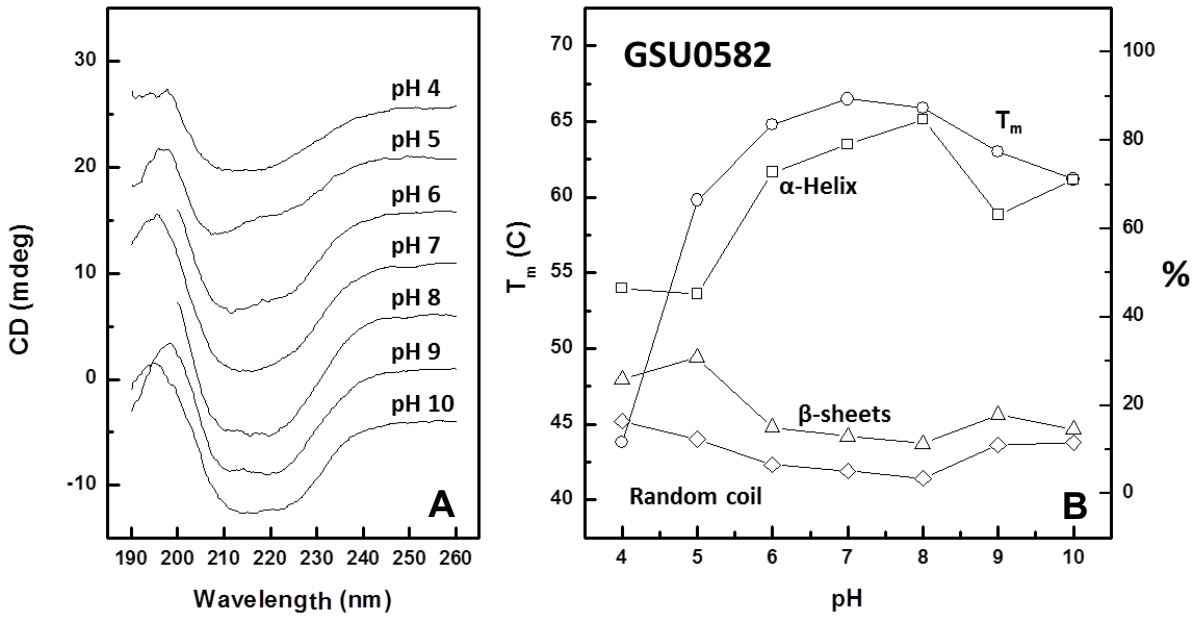

Figure 4.7 – Structural (far-UV CD) and conformational characterization of GSU0582 sensor domain as a function of pH. Far UV CD spectra (A) at different pH values were used to determine the melting temperature and secondary structure content as a function of pH (B).

These are more notorious at acidic conditions (pH < 5.0) and in agreement this results in substantial variations in the secondary structure, with a decrease in the α-helix content and an increase in β-sheets and random structures (Figure 4.7B, Table 4.2).

Table 4.2 – Thermal stability and secondary structure content of sensor GSU0582 as a function of pH.

pH	Thermal stability (°C)	Secondary Structure (%)		
		α-helix	β-sheets	Random coil
4	43.8 ± 0.9	47	26	16
5	59.8 ± 0.3	45	31	12
6	64.8 ± 0.3	73	15	7
7	66.5 ± 0.5	79	13	5
8	65.9 ± 0.6	85	11	3
9	63.0 ± 0.3	63	18	11
10	61.2 ± 0.4	71	15	12

Clearly, below the estimated isoelectric point side chain protonation of acidic residues results in a perturbation of the protein conformation, which is also inferred from a substantial decrease in the thermal stability from pH 6.0 to 4.0, corresponds to a $\Delta T_m \approx$ - 20 ºC. The maximal thermal stability of GSU0582 is observed between pH 6.0 and 8.0, averaging to $T_m \approx 66.0 \pm 1$ ºC within this range. Above the isoelectric point (pH 7.0-10.0), the measured T_m decreases only around 5 ºC, which suggests that, unlike acidification, increasing deprotonation and overall negative protein charges do not substantially affect the stability of the protein fold. In fact, within this range the relative variations in the secondary structure are somehow limited and the decrease in α-helix content goes along with a decrease in the T_m: this indicates that the decreased stability of GSU0582 above pH 8.0 results from the fact that the protein has already a modified fold upon equilibration at higher pH, prior to thermal perturbation. These results suggest that in sensor GSU0582 a set of electrostatic interactions contributes to the maintenance of the native fold. However, in respect to other stabilizing interactions such as hydrophobic contacts and hydrogen bonding, salt bridges do not seem to contribute significantly to protein stability, as their disruption does not substantially affects the protein melting temperature. A distinct scenario resulted from the analysis of sensor GSU0935. From pH 7.0 to 10.0 the secondary structure content is relatively invariant, as inferred from the comparable shape of the corresponding far-UV CD spectra and secondary structure quantitation (Figure 4.8, Table 4.3).

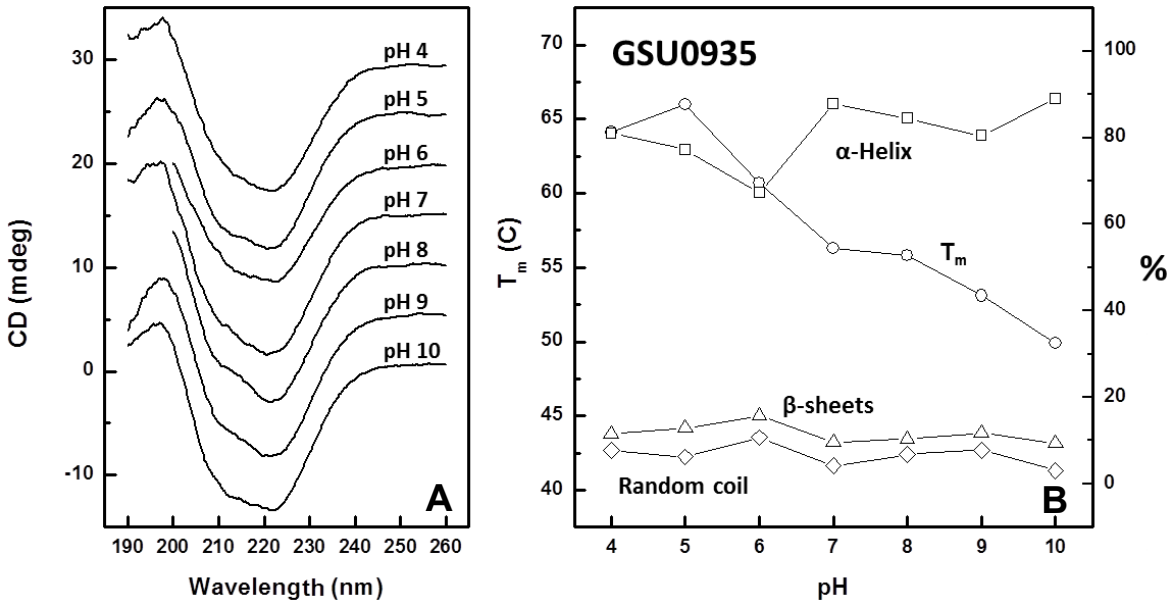

Figure 4.8 – Structural (far-UV CD) and conformational characterization of GSU0935 as a function of pH. Far-UV CD spectra (A) at different pH values were used to determine the melting temperature and secondary structure content as a function of pH (B).

Table 4.3 – Thermal stability and secondary structure content of sensor GSU0935 as a function of pH.

pH	Thermal stability (°C)	Secondary Structure (%)		
		α-helix	β-sheets	Random coil
4	64.1 ± 0.6	81	12	8
5	66.0 ± 0.2	77	13	6
6	60.7 ± 0.3	67	16	11
7	56.3 ± 0.2	88	10	4
8	55.8 ± 0.2	84	10	7
9	53.1 ± 0.2	80	12	8
10	49.9 ± 0.2	89	9	3

At pH 6.0 the α-helix content decreased but is noted to gradually recover as the protein is acidified down to pH 4.0, well below its theoretical isoelectric point. However, whereas the protein fold and secondary structure remain largely invariant in this broad pH range, protein stability steadily decreases with increasing pH. Contrary to what had been observed for GSU0582, these results indicate that in GSU0935 changes in protonation of charged amino acid side chains do not affect significantly the native fold but contribute significantly to protein stability, as their disruption results in a substantial decrease in the protein melting temperature (Figure 4.8B, Table 4.3).

4.4.6 Intrinsic disorder and distinct folding energetics influence swapped dimer formation

An important aspect to address is how the conformational and stability properties of the two sensors relate to the mechanism of dimer formation. The crystal structure of sensors GSU0582 and GSU0935 sensor domains show that these proteins form “swapped” dimers where the N-terminal helices from one molecule interact with the β-sheet of the other molecule (Figure 4.6A and B). The formation of the swapped dimer observed in the crystal structures of these two sensor domains was proposed to be a key step in the mechanism of signal transduction through the inner membrane carried out by these proteins [115]. For the swapped dimerization to occur, a significant disruption on intermolecular contacts must take place: the helical segment consisting of the two N-terminal helices (α1 and α2) of a monomer (Figure 4.6A) has to separate from its β-sheet after a rotation of the dihedral angle in the hinge region, resulting in the swapped dimer (Figure 4.6B) [115].

This means that this universal signaling fold must comprise some disorder: indeed this property has been observed in the PAS-like domain of the sensory histidine kinase DcuS, in which the disordered N-terminal helix plays an important functional role, suggesting that protein flexibility is related to the signal transduction mechanism [217]. Intrinsic disorder is a property vastly associated to signaling functions [176], and it was used the disorder predictor DisProt [200] to analyze the amino acid sequences of the two PAS-like heme sensors. The results obtained showed that GSU0935 comprises 25% of disordered residues (Figure 4.6C, blue amino acids), whereas in GSU0582 this number decreases to 13% (Figure 4.6C, red amino acids). The plots for disorder probability (Figure 4.6D, E) show that both proteins share a disordered segment (labeled as disordered 2 in Figure 4.6C) in a stretch linking the four-stranded anti-parallel β-sheet region, but the GSU0935 sensor has an additional disordered segment with comparable probability that covers the hinge region (labeled as disordered 1 in Figure 4.6C).

Since these regions are involved in domain swapping it is clear that flexibility and an intrinsic propensity to structural disorganization within these regions is an important functional property. It is then plausible that the overall stability of the PAS-like domain, which determines the overall propensity to populate unfolded conformers, is strictly related to dimer formation. As expected higher disorder and decreased conformational stability are coupled properties: the GSU0935 sensor domain which is the mostly disordered is also the least stable (Table 4.1). The thermodynamic differences observed for the two heme sensor domains correlate extremely well with the structural features of both sensors. The α-helix content of glycine and alanine residues in GSU0582 and GSU0935 structures is similar (Figure 4.6C) and, thus, other parameters should be responsible for the different stability observed. Indeed, comparison of the amino acid sequences of GSU0582 and GSU0935 shows that the first has four more arginine and six less serine residues. The higher content of arginine residues and the smaller content of serine are certainly one of the parameters that explain the different stability of the sensors. Indeed, more stable proteins have shown higher content of residues with larger side chains, which can form salt-bridges, long range or local electrostatic and hydrophobic interactions that stabilize secondary structural elements [213]. There is also a relationship with the existence of intrinsically disordered segments: the fact that GSU0935 has a higher dependence of its stability with pH than GSU0582 likely results from its higher intrinsic disorder, as usually these proteins require a higher enthalpic stabilization to counteract their decrease in configurational entropy [218].

4.5 Conclusions

PAS-domains are structural folds involved in signaling processes and the heme-containing PAS-like sensors from the bacterium *G. sulfurreducens* provide a unique framework to analyze how conformational changes effectively modulate function. In particular, the GSU0935 and GSU0582 sensor domains are excellent working models, as these proteins are unique examples of PAS-like folded sensors undergoing swapped dimer formation. The study here reported points to the hypothesis that the primary sequence of structurally identical PAS-like heme sensors dictating differences in stability will favor or disfavor the formation of the swapped dimer and thus function, as dimerization is a crucial step for signaling. Intrinsically disordered segments found within these proteins will also contribute to protein “fuzziness”, especially as it involves linker regions that modulate conformational rearrangements, interactions and the nesting of interfaces between the two subunits. Overall, the observations here reported provide a structural and energetic framework to explain the functional properties of PAS-like hemic sensors. In light of this possibility, the existence of multiple PAS-like heme homologues within *G. sulfurreducens* could be related to the fact that differences in stability between otherwise structurally identical proteins result in different signaling properties and activation thresholds, thus broadening the functional range of action of the sensors [218].

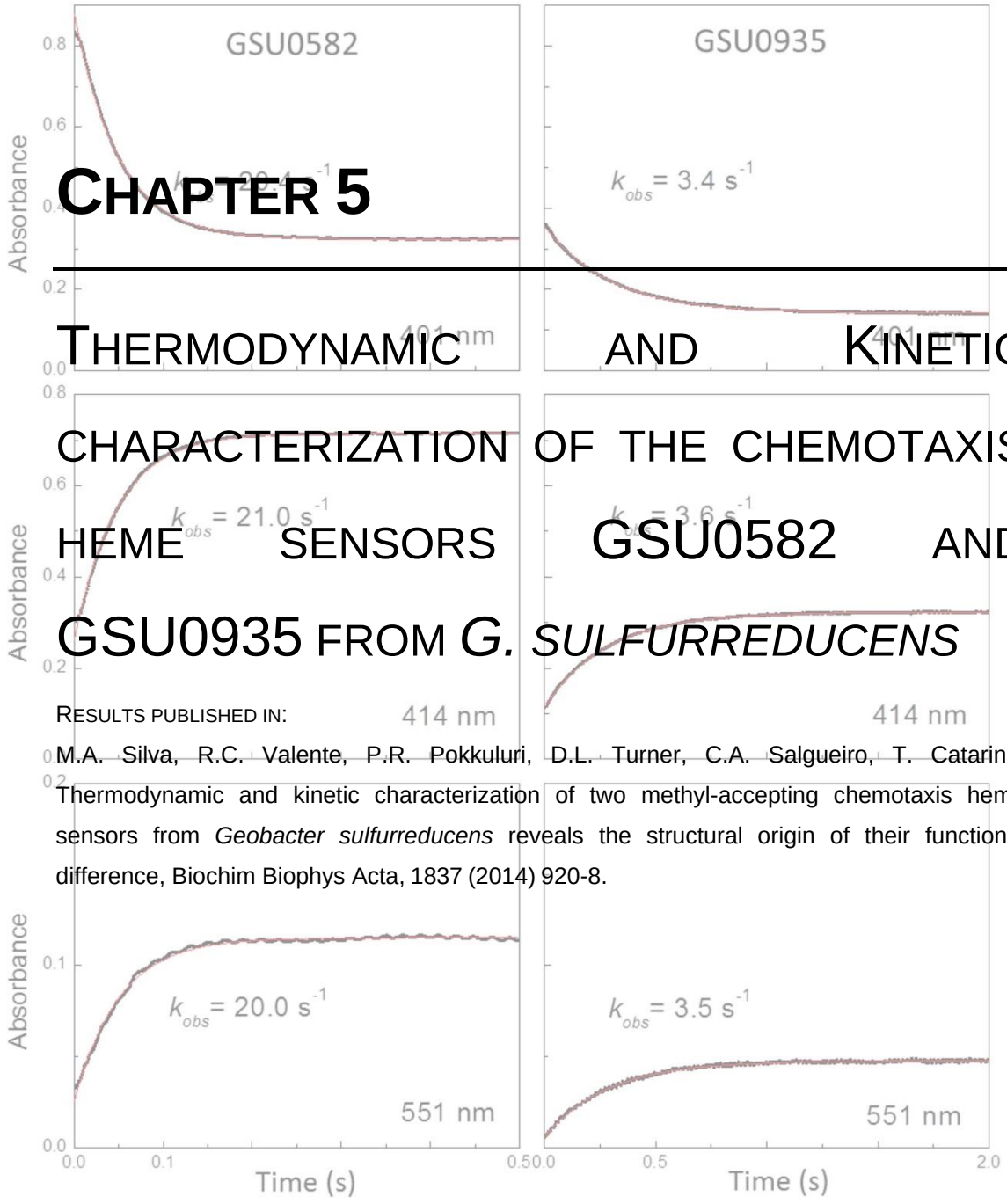

CHAPTER 5

THERMODYNAMIC AND KINETIC CHARACTERIZATION OF THE CHEMOTAXIS HEME SENSORS GSU0582 AND GSU0935 FROM *G. SULFURREDUCENS*

RESULTS PUBLISHED IN:

M.A. Silva, R.C. Valente, P.R. Pokkuluri, D.L. Turner, C.A. Salgueiro, T. Catarino, Thermodynamic and kinetic characterization of two methyl-accepting chemotaxis heme sensors from *Geobacter sulfurreducens* reveals the structural origin of their functional difference, Biochim Biophys Acta, 1837 (2014) 920-8.

5. THERMODYNAMIC AND KINETIC CHARACTERIZATION OF THE CHEMOTAXIS HEME SENSORS GSU0582 AND GSU0935 FROM *G. SULFURREDUCENS*

5.1 Abstract

The periplasmic sensor domains GSU0582 and GSU0935 are part of methyl-accepting chemotaxis proteins of the bacterium *Geobacter sulfurreducens* that might have their signal transduction mechanism related with the redox-linked ligand switch. It is now report the thermodynamic and kinetic characterization of the sensors GSU0582 and GSU0935 by visible spectroscopy and stopped-flow techniques, at several pH and ionic strength values. Despite their similar spectroscopic features, the midpoint reduction potentials and the rate constants for reduction by sodium dithionite are considerably different in the two sensors. The reduction potentials are negative and well framed within the typical anoxic subsurface environments in which *Geobacter* species predominate. The GSU0935 midpoint reduction potentials are lower than those of GSU0582 at all pH and ionic strength values and the same were observed for the reduction rate constants. The origin of the different functional properties of these closely related sensor domains are rationalized in the structural terms. The results suggest that the sensors GSU0582 and GSU0935 are designed to function in different working potential ranges, allowing the bacteria to trigger an adequate cellular response in different anoxic subsurface environments. These findings provide an explanation for the co-existence of two very similar methyl-accepting chemotaxis proteins in *Geobacter sulfurreducens*.

5.2 Introduction

The bacterial environment is constantly changing due to variations in physicochemical parameters such as temperature, nutritional opportunities, environmental gases, light or oxygen tension. Signal transduction systems establish intracellular information-processing networks that link external stimuli to specific adaptative responses. Bacterial heme-based sensors constitute an important group of proteins that exploit the redox chemistry of the heme group to sense environmental changes [132, 187, 191, 219-221]. The more common heme-based sensors contain a *b*-type heme in the sensor domain that could bind effector molecules such as O_2, NO, or CO

[168]. These proteins typically comprise a regulatory heme-binding domain (sensor domain) coupled to a neighboring transmitter (transduction domain). In functional terms, the binding of a physiological effector to the heme triggers the response process by conformational changes at the transduction domain generating the intracellular signal and concomitant regulation of the physiological response [132, 187, 191, 219-222]. The residues located in the neighbourhood of the heme play a crucial role in discriminating the physiological ligand from other possible ligands since the intramolecular signal transduction cascade is initiated by local conformational changes in this region. Therefore, discrimination and selection of the correct stimulus is crucial for triggering an appropriate response. This is a particular challenge for *Geobacter* bacteria whose remarkable respiratory versatility allows the microorganisms to proliferate in quite distinct environments [223]. The versatility showed by the bacterium *G. sulfurreducens* might explain the coexistence of a large number of heme-based sensors since an efficient metabolic switch is necessary to respond to the exhaustion of a particular electron acceptor, the appearance of a different electron donor or even a change in the redox potential of the environment. Indeed, as mentioned in Chapter 1, two periplasmic sensor domains were found in *G. sulfurreducens* genome, each containing one heme *c*-binding motif [150]. The *G. sulfurreducens* heme sensors, encoded by genes *gsu0582* and *gsu0935*, are parts of methyl-accepting chemotaxis proteins with similar predicted topologies. The sensor domains of GSU0582 and GSU0935 have been structurally and biochemically characterized, despite their moderate sequence homology (Figure 1.13) showing that in oxidized form, GSU0582 and GSU0935 sensor domains have a high-spin heme able to bind NO and a low-spin heme in the reduced form which can bind NO and CO. The binding/dissociation of CO or NO is fully reversible and at ferric form, sensor GSU0582 shows a much higher affinity for NO [168].

Collecting all the available information for these sensor domains, it was proposed that the change of the redox state coupled to heme spin state/coordination alteration could initiate the signal transduction mechanism [168]. This hypothesis, reinforced by the significant differences observed in the low reduction potential values of GSU0582 and GSU0935 [115], suggests that the proteins could work as redox sensors for chemotaxis. To further understand the functional differences between the two sensors, it was performed a detailed thermodynamic and kinetic characterization of their redox behavior within the physiological pH range and rationalized the results in terms of the sequence and structural determinants.

5.3 Materials and Methods

5.3.1 Stopped-flow technique

Kinetic methods of analysis have become increasingly popular in many areas of analytical and bioanalytical chemistry. Perhaps the most frequently used rapid kinetics techniques is stopped-flow. The stopped-flow spectrophotometer is essentially a UV-visible spectrophotometer coupled to a sample handling unit (Figure 5.1) designed to carry out rapid mixing of the reagents, enabling the study of reactions that occur in the millisecond and second time scales.

Figure 5.1 – Photo of the stopped-flow system implemented at the Instituto de Tecnologia Química e Biológica (ITQB). Photo credit: Inorganic Biochemistry and NMR research group at ITQB.

Both absorbance and fluorescence detection can be employed to follow the reactions by optical changes. Small volumes of the two reagents are held in the drive syringes, a common drive push plate is used to drive the syringes quickly, displacing the reagents and causing them to mix rapidly in the mixing chamber that precedes the observation cell.

The resultant reaction volume then displaces the contents of an observation cell thus filling it with freshly mixed reagents. The volume injected is limited by the stop syringe used to set the driven volume (stop volume). Just prior to stopping, a steady state flow is achieved. The solution entering the flow cell is only milliseconds old. The aged solution flows through the tip of the stop syringe until the piston is stopped by a rigid stop block, causing rapid deceleration of the solutions and triggering the data acquisition system (Figure 5.2).

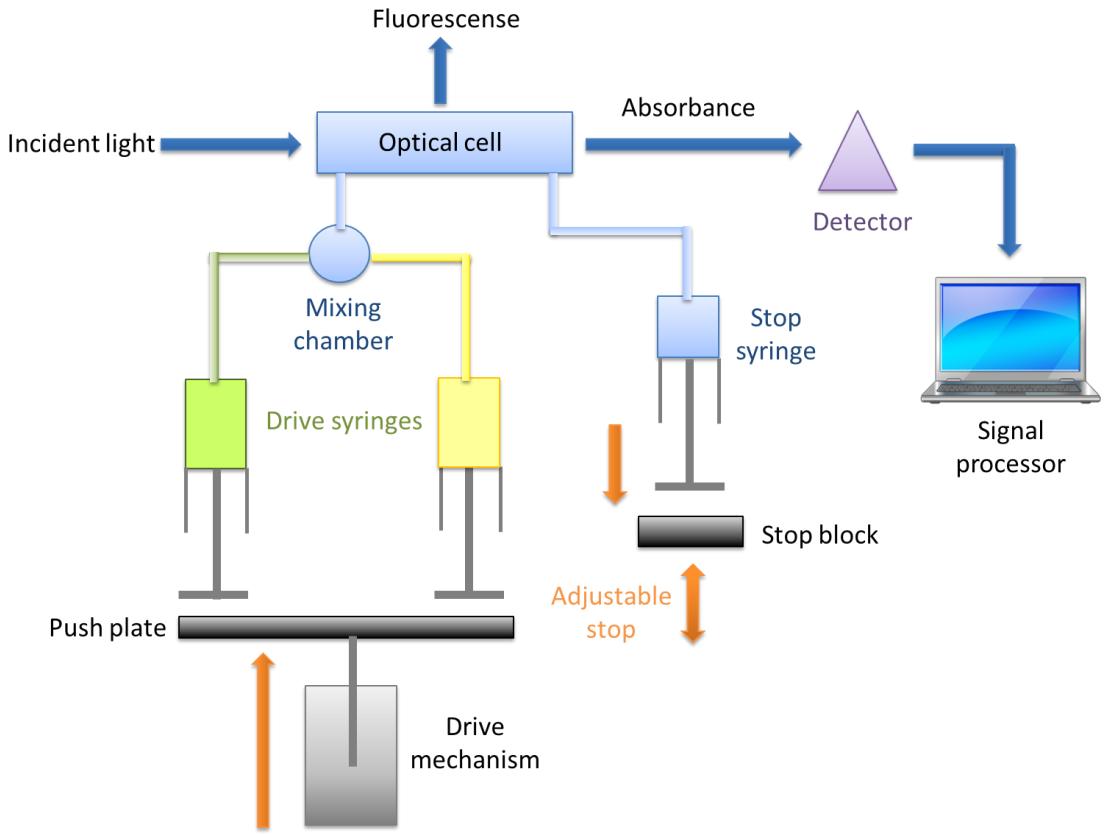

Figure 5.2 – Schematic diagram of a stopped-flow analyzer. The blue arrows show the direction in which the system is moving and the orange arrows the movement of the system units.

Because the solution takes a finite time to flow from the mixer to the observation point, the mixed solution is already of a certain age and has consequently reacted to a certain extent when the acquisition of the data starts. The age of the solution at the instant of stopping is defined as the dead time of the stopped-flow system. Since the process of mixing is not instantaneous, a short deadtime is not necessarily a good thing. In fact, if the mixing time exceeds the deadtime the reagents are still being mixed in the observation cell when data collection starts. For very fast reactions, at the limit of measurability, this results in a sigmoidal shape of the trace. The stopped-flow apparatus is designed such that the mixing time is smaller than the deadtime.

The complete stopped-flow apparatus includes a spectrophotometer unit, a sample handling unit, a data acquisition system and a thermostating system. The monochromatic light emitted by the optical assembly of the spectrophotometer unit is conducted to the sample handling unit by a quartz optical fibre. In absorbance measurements, a photomultiplier detects the light transmitted through the samples. The temperature of the reagents in the drive syringes is kept constant by the thermostating bath connected to the sample handling unit.

5.3.2 Redox titrations followed by visible spectroscopy

Anaerobic redox titrations followed by visible spectroscopy were performed inside a glove box (MBraun MB-10-Compact) under an argon atmosphere with O_2 levels kept below 0.2 ppm as previously described [115]. The UV-visible spectra were recorded with a Thermo Scientific Evolution™ 300 UV-visible spectrophotometer and the temperature was maintained by using an external circulating bath [224]. The solution potentials were measured using a combined Pt/Ag/AgCl electrode (Crison), calibrated before each titration with freshly prepared saturated solutions of quinhydrone at pH 7.0 and 4.0 and checked at the end for stability. The reported values are relative to the standard hydrogen electrode (SHE). Experiments were performed at pH 6.0, 7.0 and 8.0 using 5 mM sodium phosphate buffer at two different ionic strengths (10 and 200 mM) and 9 µM protein solutions. To ensure a good equilibrium between the redox centers and the working electrode, a mixture of redox mediators was added to the protein solution: methylene blue (E_{m7} = 11 mV), gallocyanine (E_{m7} = 21 mV), indigo tetrasulfonate (E_{m7} = -30 mV), indigo trisulfonate (E_{m7} = -70 mV), indigo disulfonate (E_{m7} = -10 mV), anthraquinone-2,6-disulfonate (E_{m7} = -185 mV), 2-hydroxy-1,4-naphthoquinone (E_{m7} = -152 mV), anthraquinone-2-sulfonate (E_{m7} = -225 mV), safranine O (E_{m7} = -280 mV), diquat (E_{m7} = -350 mV), benzyl viologen (E_{m7} = -345 mV), neutral red (E_{m7} = -325 mV), and methyl viologen (E_{m7} = -440 mV). The final concentration of mediators was 2 µM to avoid interference caused by specific binding of mediators to the protein. Each titration consisted of a stepwise reduction using a solution of sodium dithionite, followed by oxidation using a solution of ferricyanide. After each addition of titrant, ample time was allowed for a stable measurement of redox potential to be reached and a spectrum of the sample was taken in the range 700-400 nm. In order to confirm that the pH is stable, the pH was also measured at the end of each redox titration. The redox titrations were repeated at least twice for each pH value, each time both in the oxidative and reductive directions to check for hysteresis. Reproducibility between the runs was typically better than 5 mV.

5.3.3 Analysis of thermodynamic data

The reduced fraction of each sensor was determined using the α band peak at 551 nm. The optical contribution of the mediators was subtracted by measuring the height of the peak at 551 nm relative to the straight line connecting the two isosbestic points (509 and 565 nm for GSU0582; 506 and 562 nm for GSU0935) flanking the α and β bands according to the method described in the literature [225, 226]. The reduction potentials were obtained by fitting the experimental variation of the total reduced fraction to one-electron Nernst equation as previously described [227]. Values of

the reduction potentials extrapolated to infinite ionic strength (E^{∞}) were calculated as described by Pedro Quintas *et al*. [228], using the Equation 5.1.

$$E^{\circ} = E^{\infty} - 0.09182 \left(\frac{\exp(-\kappa r_1 \sqrt{I})}{1+\kappa r_2 \sqrt{I}} - \frac{\exp(-\kappa r_2 \sqrt{I})}{1+\kappa r_1 \sqrt{I}} \right) \left(\frac{Z_1 Z_2 - Z_1' Z_2'}{r_1 + r_2} \right) \quad (5.1)$$

In this equation κ = 0.329 $Å^{-1}M^{-½}$ at 25 ºC, r_1 and r_2 are the radii, and Z_1 and Z_2 are the charges of the reactants. The primed terms represent the products. For the reducing agent r_2 = 1.5 Å [229], Z_2 = -1 and Z_2' = 0 were used in the calculations. The effective radii of the proteins were considered equal to the distance between the iron and the carboxylate group of the heme propionate, r_1 = 8 Å. From the fit it was also estimate the protein charge Z_1 that is affecting the reduction potential of the heme at the different pH values.

5.3.4 Kinetic experiments

The rate of reduction of GSU0582 and GSU0935 by sodium dithionite was studied as a function of ionic strength in the pH range 6.0 to 8.0. Rapid mixing kinetic experiments were carried out on a HI-TECH Scientific SF-61 stopped-flow instrument inside an anaerobic chamber (Mbraun MB 150 I) where the oxygen level was kept below 0.2 ppm. The temperature was kept at 293 ± 1 K using an external circulating bath. The data were acquired at 401, 414 and 551 nm using a large excess of sodium dithionite to guarantee pseudo-first order kinetics, irreversible electron transfer steps and the complete reduction of the sensors [228]. At least three data sets for each experimental condition were averaged to increase the signal to noise ratio.

Buffers at different ionic strengths covering the range 10 to 200 mM were prepared by diluting a concentrated NaCl solution in 5 mM sodium phosphate buffer pH 6.0, 7.0 and 8.0 with degassed water inside an anaerobic chamber. Small pH variations were corrected by adding concentrated HCl or NaOH. Protein solutions (9 µM) were prepared by diluting a concentrated stock solution (200 µM) in the desired buffer. The concentration of protein was determined after each experiment by UV-visible spectroscopy using ε_{401} = 188 000 $M^{-1}cm^{-1}$ [168] for the oxidized protein. The reducing agent, sodium dithionite was prepared in the same buffer for the experiments at pH 7.0 and pH 8.0. For the experiments below pH 7.0, solutions were prepared in 5 mM sodium phosphate buffer pH 7.0 to avoid the sodium dithionite decomposition in acidic conditions, with NaCl added to the desired ionic strength. After each experiment the actual pH of the reaction was measured. For each experiment the actual concentration of sodium dithionite was measured by UV-visible spectroscopy using ε_{314} = 8 000 $M^{-1}cm^{-1}$ [230] and the values were in the range 100–200 µM after mixing.

5.3.5 Analysis of kinetic data

The kinetics of the reduction by sodium dithionite ($Na_2S_2O_4$) of both sensor domains were analyzed assuming the kinetic reaction: Protein^{ox} + $Na_2S_2O_4$ → Protein^{red} using a large excess of $Na_2S_2O_4$ to ensure that the reaction occurred under pseudo-first-order conditions. Observed rate constants (k_{obs}) were obtained by single exponential fitting of the kinetic traces using the analysis tools provided by the stopped-flow software Kinetic Studio. The reported k_{obs} values are the average of at least three independent curves obtained at different wavelengths and different time scales and the errors were calculated from the standard deviations. The nature of the reducing agent was determined according to the method of Lambeth and Palmer [231] considering the reaction $S_2O_4^{2-} \rightleftarrows 2\ SO_2^{\bullet-}$. Second-order rate constants k were obtained using Equation 5.2.

$$k = k_{obs}\left(k_{diss} \times \left[Na_2S_2O_4\right]\right)^{-1/2} \tag{5.2}$$

where k_{diss} is the equilibrium dissociation constant of sodium dithionite.

The variation of the equilibrium dissociation constant of dithionite (k_{diss}) with ionic strength (I) (Equation 5.3) was taken into account as described by Pedro Quintas *et al.* [228]:

$$\ln k_{diss} = \ln k_1^{\infty} - \ln k_{-1}^{\infty} + \frac{2\,Z^2\alpha\,\sqrt{\mathrm{I}}}{1+\kappa r\sqrt{\mathrm{I}}} - \frac{4\,Z^2\alpha\,\sqrt{\mathrm{I}}}{1+2\,\kappa r\sqrt{\mathrm{I}}} \tag{5.3}$$

where α = 1.17 $M^{-½}$, κ = 0.329 $Å^{-1}M^{-½}$ at 25 ºC and Z and r are the charge and radius of $SO_2^{\bullet-}$, respectively Z = -1 and r = 1.5 Å [2]. The value $\ln k_1^{\infty} - \ln k_{-1}^{\infty}$ = –19.93 was obtained from the data of Thorneley and Lowe by using I = 0.03 M and k_{diss} = 1.60 × 10^{-9} M [232].

Marcus theory applied to the Debye-Hückel formalism (Equation 5.4) [228, 233] was used to fit the dependence of the second order rate constants on the ionic strength and obtain the effective charge on the protein surface (Z_1), which is relevant for the electrostatic interaction with the exogenous electron donor, hereafter designated by effective charge, and the value of the second order rate constant extrapolated to infinite ionic strength (k_∞).

$$\ln k = \ln k_\infty - 3.576\left(\frac{\exp\left(-\kappa r_1\sqrt{\mathrm{I}}\right)}{1+\kappa r_2\sqrt{\mathrm{I}}} + \frac{\exp\left(-\kappa r_2\sqrt{\mathrm{I}}\right)}{1+\kappa r_1\sqrt{\mathrm{I}}}\right)\left(\frac{Z_1 Z_2}{r_1+r_2}\right) \tag{5.4}$$

In this equation κ = 0.329 $Å^{-1}M^{-½}$ at 25 ºC, r_1 and r_2 are the radii, and Z_1 and Z_2 are the charges of the reactants. For the reducing agent r_2 = 1.5 Å [229] and Z_2 = -1 were used in the calculations. The effective radius of the protein was considered equal to the distance between the iron and the carboxylate group of the heme propionate, r_1 = 8 Å.

5.4 Results and Discussion

5.4.1 Thermodynamic studies

The redox titrations of sensor domains GSU0582 and GSU0935 followed by visible spectroscopy in the physiological pH range for *G. sulfurreducens* growth at two ionic strengths (10 and 200 mM) are shown in Figure 5.3.

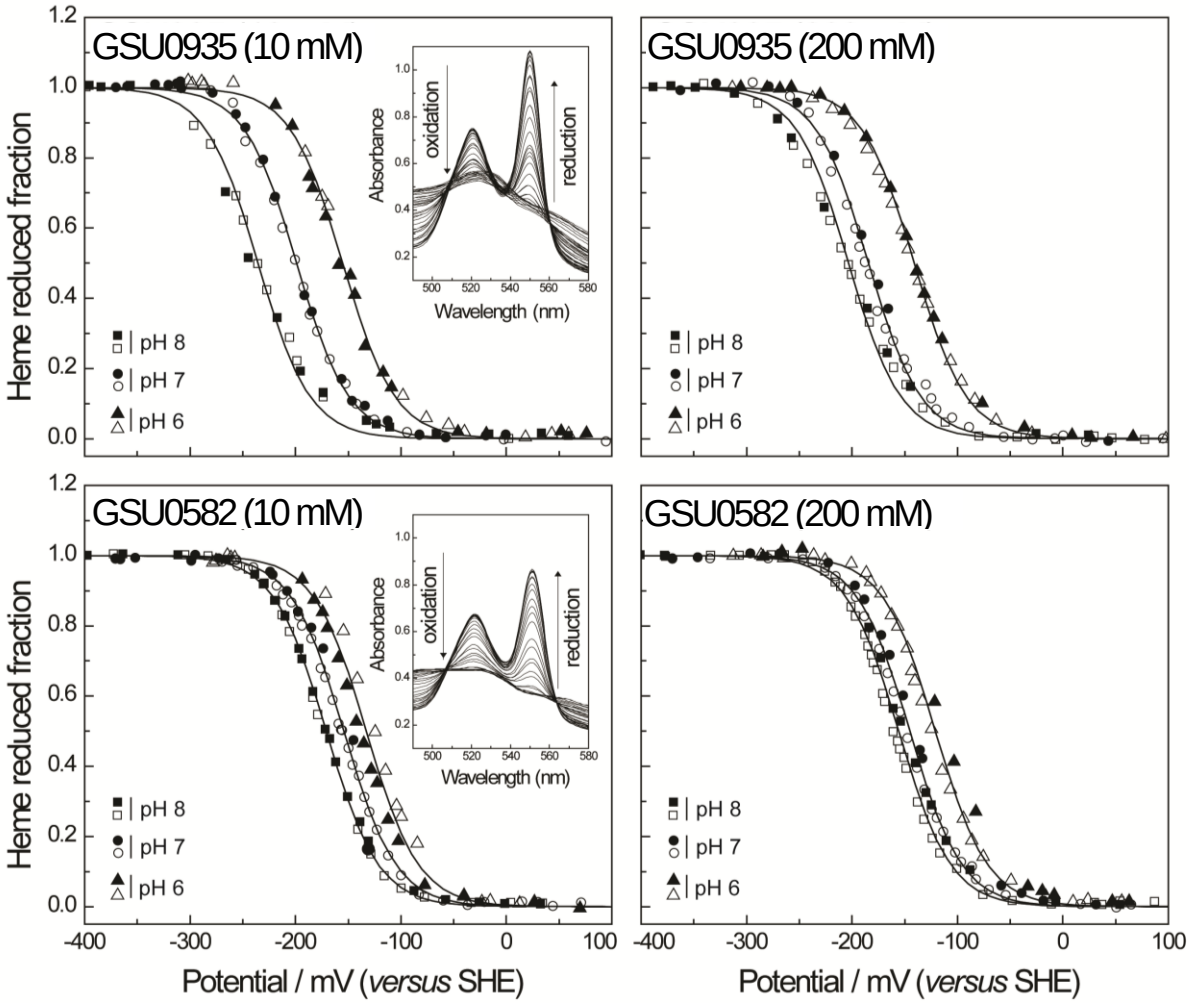

Figure 5.3 – Redox titrations followed by visible spectroscopy for GSU0935 and GSU0582 sensor domains at different pH and ionic strength values (10 and 200 mM). The triangles correspond to the curves obtained at pH 6.0, the circles at pH 7.0 and squares at pH 8.0. The void and solid symbols represent

the data points in oxidative and reductive titrations, respectively. The lines are the results of the fit to the Nernst equation for one-electron reduction. The reduction potentials obtained, relative to standard hydrogen electrode (SHE), are listed in Table 5.1. As an example, the inset illustrates α and β band regions of the visible spectra for sensors GSU0935 and GSU0582 at pH 7.0 acquired during the redox titration. The arrows in the insets indicate the direction of reduction and oxidation.

The previous spectroscopic characterization showed that the change in the redox state of the sensor domains is coupled to a heme state/coordination alteration [115, 168]. This would imply conformational changes in the heme region, in particular at the distal ligand position. However, with exception of sensor GSU0582 at pH 6.0, no hysteresis was observed, as the reductive and oxidative curves are superimposable, indicating that the redox process is fully reversible. Even for sensor GSU0582, the hysteresis is not significant since the reductive and oxidative curves differ by less than 10 mV. The midpoint reduction potentials obtained from the fitting of the Nernst equation to each curve are indicated in Table 5.1. The reduction potential values are negative for both heme sensors but cover different working potential ranges (Table 5.1 and Figure 5.3).

Table 5.1 – Midpoint reduction potentials in mV (*versus* SHE) of heme sensor domains GSU0582 and GSU0935 measured at different pH and ionic strength values.

pH	6.0		7.0		8.0	
Ionic strength (mM)	10	200	10	200	10	200
GSU0582	-133 ± 4	-121 ± 4	-154 ± 4	-145 ± 3	-171 ± 3	-156 ± 3
GSU0935	-155 ± 4	-141 ± 4	-199 ± 3	-184 ± 3	-235 ± 2	-203 ± 3

The negative values for the reduction potentials are well framed within the typical anoxic subsurface environments in which *Geobacter* species predominate [234-238] suggesting that the *c*-type heme group might work primarily as redox sensor in *G. sulfurreducens* periplasm.

The reduction potential values of sensors GSU0582 and GSU0935 are affected by the ionic strength of the solution. For both proteins, the reduction potential increase with the ionic strength (Table 5.1 and Figure 5.4), an effect that is more noticeable for GSU0935, particularly at high pH.

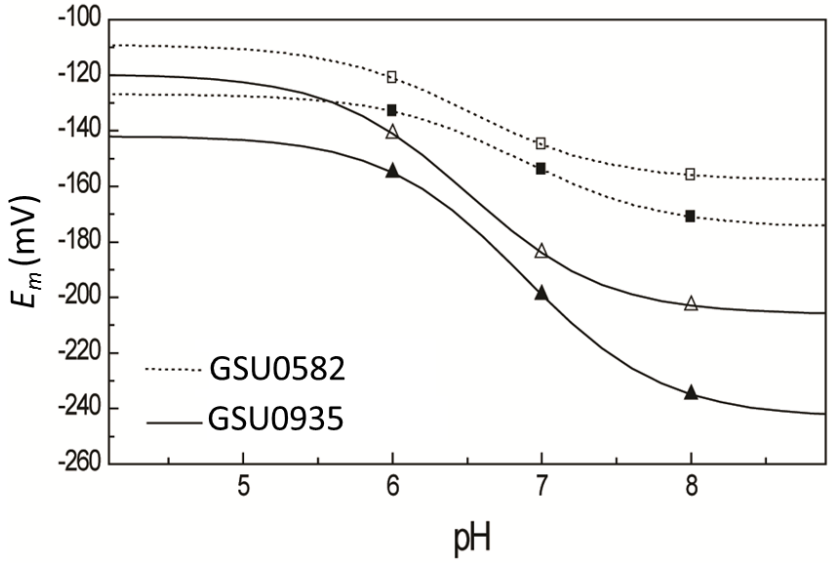

Figure 5.4 – pH dependence of the reduction potential (E_m) of sensors GSU0582 (squares) and GSU0935 (triangles). Data points are represented by symbols (solid symbols for 10 mM ionic strength and void symbols for 200 mM ionic strength). The lines were simulated with Equations 5.5 and 5.6 and are an illustration of the transfer of one electron coupled to one proton (dashed lines) or one electron coupled to two identical protons (solid lines). If a single proton (Equation 5.5) were used to simulate all the data, the difference pK_a^{red}-pK_a^{ox} would be about 1 pH unit in GSU0582 and about 2 pH units in GSU0935.

As the ionic strength increases, the electrostatic effect of charged residues located in the vicinity of the heme groups is reduced by counter ion shielding effects. Thus, the observed increase of the reduction potential values suggests that the dominant charged residues in the vicinity of the heme groups are negative.

The midpoint reduction potential of both sensors is pH dependent (redox-Bohr effect) in the physiological range for *G. sulfurreducens* growth and those of GSU0935 sensor are the ones most affected (Figure 5.4). The decrease in the reduction potential values with pH leads to a progressive stabilization of the oxidized form, which can be explained on a purely electrostatic basis: the progressive deprotonation of an acid/base group in the vicinity of the heme groups is expected to lower its affinity for electrons with the concomitant decrease of the reduction potential values.

The variation in the reduction potential of a heme affected by a single proton is given by Equation 5.5 [239], where the superscripts *red* and *ox* indicate the K_a values of the ionizable group with the heme reduced or oxidized and *basic* indicates the limiting value of E_m at high pH.

$$E_m = E_0^{basic} - \frac{RT}{F} \ln \left(\frac{1 + \frac{[H^+]}{K_a^{ox}}}{1 + \frac{[H^+]}{K_a^{red}}} \right) \qquad (5.5)$$

The larger pH dependence of the reduction potential observed for GSU0935 must reflect a stronger electron-proton interaction, which could be the result of a smaller distance between the heme and the ionizable group or a smaller dielectric constant of the intervening medium. However, it could also be caused by the involvement of a second ionizable group. The expression for two distinct and non-interacting protons labelled α and β is given in Equation 5.6, which is the simple sum of the effects of the two protons.

$$E_m = E_0^{basic} - \frac{RT}{F} \ln \left(\frac{\left(1 + \frac{[H^+]}{K_{a\alpha}^{ox}}\right)\left(1 + \frac{[H^+]}{K_{a\beta}^{ox}}\right)}{\left(1 + \frac{[H^+]}{K_{a\alpha}^{red}}\right)\left(1 + \frac{[H^+]}{K_{a\beta}^{red}}\right)} \right) \tag{5.6}$$

The observable macroscopic values are related to these by Equation 5.7.

$$K_{aA} = \frac{K_{a\alpha}K_{a\beta}}{K_{a\alpha} + K_{a\beta}} \quad ; \quad K_{aB} = K_{a\alpha} + K_{a\beta} \tag{5.7}$$

where A and B refer to the first and second acid/base equilibrium, respectively. The effect of two protons becomes indistinguishable from that of a single proton when the microscopic K_a values for the individual groups are $K_{a\alpha}^{ox} = K_a^{ox}$, $K_{a\beta}^{red} = K_a^{red}$ and $K_{a\alpha}^{red} = K_{a\beta}^{ox}$. It is therefore impossible to distinguish the effect of one or two protons from the slope of the pH dependence of the reduction potential. Additional information must be obtained from different experiments to be able to discriminate if the redox-Bohr effect involves one or two protons. In this work, information obtained from the analysis of kinetic and structural data was used to distinguish between the two, as discussed below.

5.4.2 Kinetic studies

To determine the nature of the reducing species, the rate of reduction of GSU0582 and GSU0935 was studied as a function of the concentration of sodium dithionite [229]. The linear dependence of the observed rate constants (k_{obs}) on the square root of the concentration of

sodium dithionite (Figure 5.5) showed that the reducing species is the bisulfite radical ($SO_2^{\bullet-}$) for both sensors.

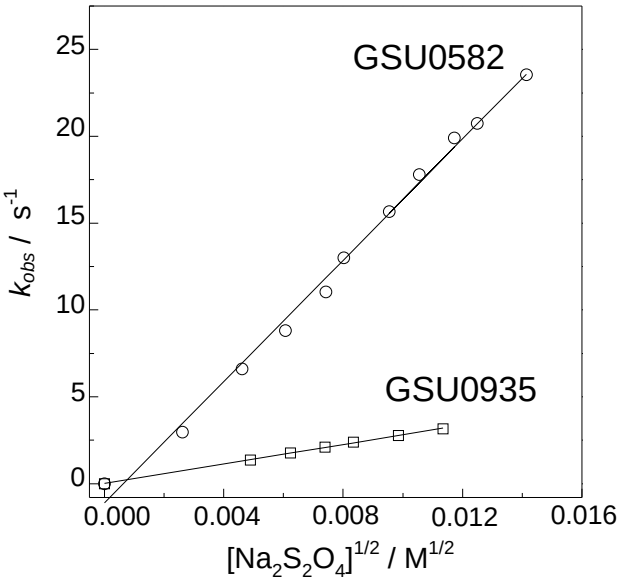

Figure 5.5 – Dependence of the observed rate constants (k_{obs}) on the square root of the sodium dithionite concentration at pH 7.0 for sensor domains GSU0935 (squares) and GSU0582 (circles). The dashed lines are the result of the linear fit to the data points.

The second order rate constants calculated from the observed rate constants, as described in the Materials and Methods section, are included in a Table 5.2.

Table 5.2 – Values of second order rate constants of the reduction of the two heme sensor domains, at different pH values and ionic strengths. The errors were calculated as 3 times the standard deviations.

		GSU0582	GSU0935
	I (mM)	**k / 10^6 $M^{-1}s^{-1}$**	**k / 10^6 $M^{-1}s^{-1}$**
pH 6.0	6	28 ± 1	6 ± 1
	30	35 ± 2	8 ± 2
	50	38 ± 3	9 ± 2
	100	44 ± 7	11 ± 1
	150	49 ± 5	12 ± 2
	200	51 ± 2	13 ± 2

(continued)

		GSU0582	GSU0935
	I (mM)	***k* / 10^6 $M^{-1}s^{-1}$**	***k* / 10^6 $M^{-1}s^{-1}$**
pH 7.0	11	30 ± 1	5 ± 1
	30	34 ± 3	6 ± 1
	50	39 ± 2	7 ± 2
	100	43 ± 7	9 ± 2
	150	48 ± 2	10 ± 3
	200	50 ± 3	11 ± 2
pH 8.0	15	28 ± 2	3 ± 0.2
	30	34 ± 4	4 ± 0.4
	50	36 ± 3	5 ± 0.9
	100	43 ± 4	6 ± 0.8
	150	46 ± 5	8 ± 1
	200	49 ± 4	9 ± 2

Despite the low value of the equilibrium dissociation constant of sodium dithionite, the concentration of $SO_2^{\bullet-}$ can be considered constant due to the very fast dissociation rate and the high concentration of sodium dithionite compared to the protein, making the reaction between $SO_2^{\bullet-}$ and the sensors pseudo-first-order. To obtain information on the nature and intensity of charges in the vicinity of the hemes, the rate of reduction of GSU0582 and GSU0935 by sodium dithionite was studied as a function of ionic strength at different pH values using the stopped-flow technique. As an example the time course traces obtained for both sensors at pH 7.0 and 200 mM ionic strength are shown in Figure 5.6.

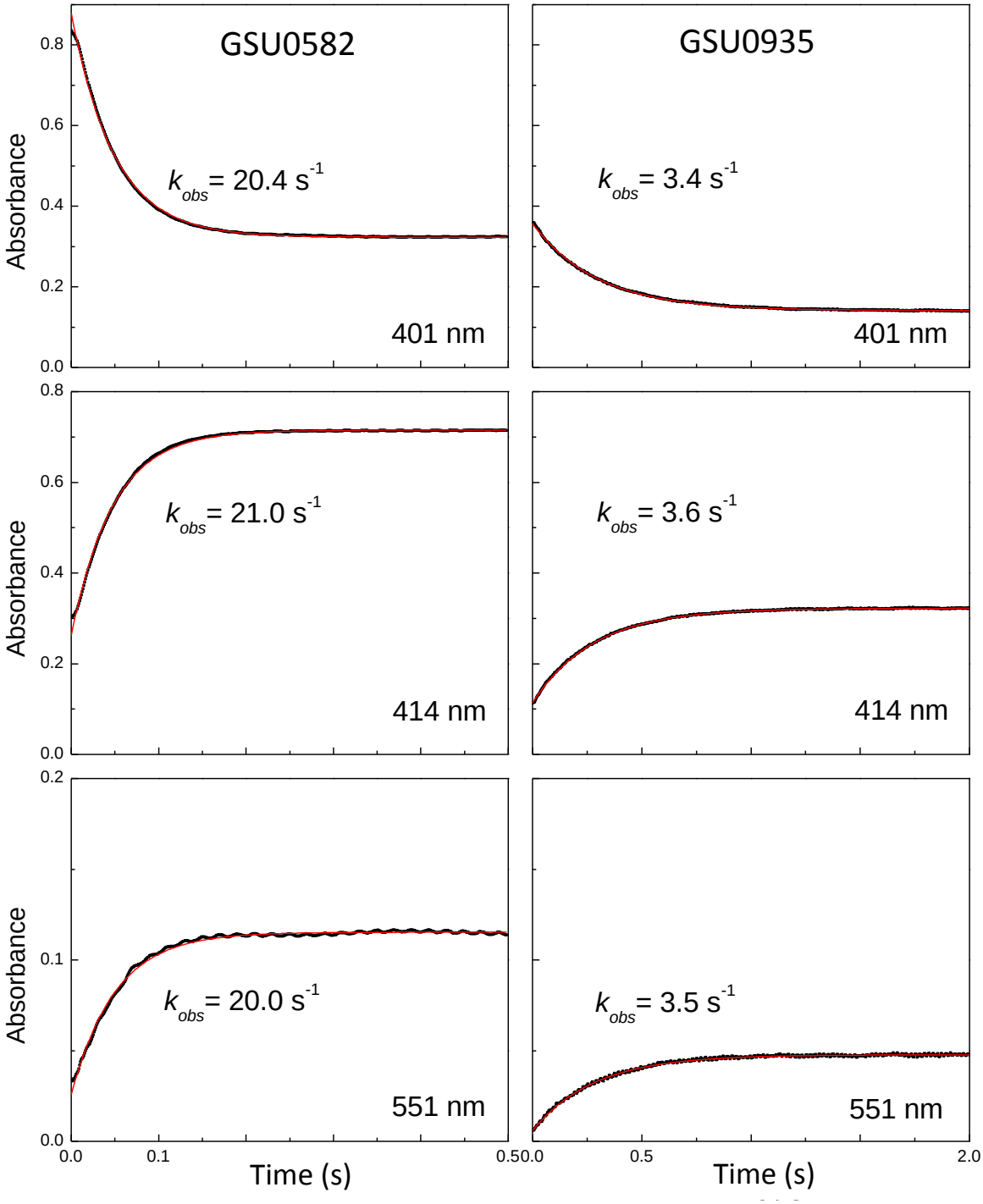

Figure 5.6 – Kinetics of reduction by sodium dithionite of GSU0582 (left panels) and GSU0935 (right panels) obtained at 401, 414 and 551 nm (pH 7.0 and 200 mM ionic strength). The colored lines are the result of the fit of the data using a single exponential.

The logarithm of the second order rate constants as a function of the square root of the ionic strength, at different pH values, is presented in Figure 5.7.

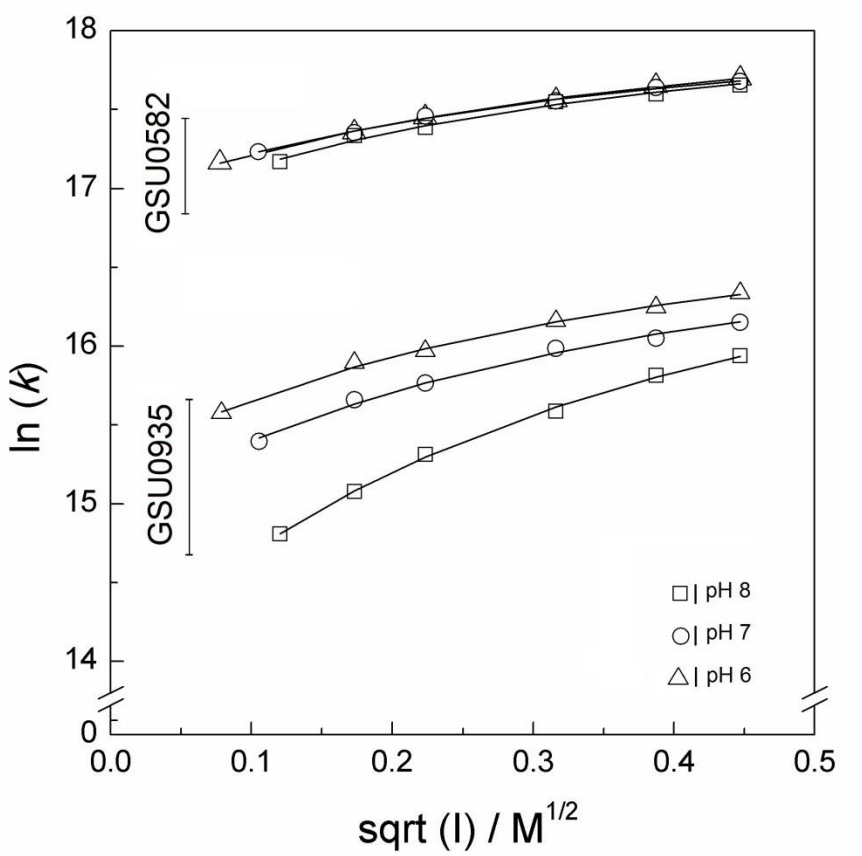

Figure 5.7 – Dependence of the logarithm of the second order rate constant for the reduction of the heme sensor domains by sodium dithionite, ln(*k*), on the square root of the ionic strength at different pH values for sensors GSU0582 and GSU0935 (triangles pH 6.0, circles pH 7.0 and squares pH 8.0). The lines are the result of the fit of Equation 5.4 to the data points.

From the positive slope of the curves it can be concluded that the electrostatic interaction between the redox partners is repulsive because the shielding of the charges at high ionic strength leads to an increase of the rate constant. Since the reducing species is negatively charged, the effective charge on the protein must be also negative for both sensors.

The rate constants of GSU0582 are higher than those of GSU0935, which might be a consequence of the larger driving force for the electron transfer reaction. The reducing species is $SO_2^{\bullet-}$ and the couple $SO_2/SO_2^{\bullet-}$ has a reduction potential -0.3 V, which is independent of pH above pH 2.0 [240]. Since the reduction potential of GSU0582 is less negative than that of GSU0935 (Table 5.1), this shows that GSU0582 has a larger driving force for electron transfer. The rate constants of GSU0582 are also independent of pH whereas those of GSU0935 are clearly pH dependent, the rates decrease with pH increasing. Because of the slope increase with the intensity of the charge and the fact that GSU0935 curves at pH 6.0 and pH 7.0 are nearly parallel, it is suggested that the charge does not change much in this pH range, consequently the lower rate observed at pH 7.0 is probably due to a decrease in the driving force. However, the slope increases

significantly going from pH 7.0 to pH 8.0, indicating that the effective charge on the protein becomes more negative. As expected, the repulsive effect of the extra negative charge is more apparent at low ionic strength.

A quantitative analysis based on Marcus theory applied to the Debye-Hückel formalism (Equation 5.4) makes it possible to obtain the effective charges of the two sensors at the different pH values and the rate constants extrapolated to infinite ionic strength. The results of the fit are presented in Table 5.3, together with the extrapolation of the reduction potentials of the heme sensor domains to infinite ionic strength, obtained as described by Pedro Quintas *et al*. using the Equation 5.1 [228].

Table 5.3 – Effective charge on the protein (Z_1), second order rate constant extrapolated to infinite ionic strength (k_∞) and reduction potential E_m^∞ extrapolated to infinite ionic strength, at different pH values for the heme sensor domains GSU0582 and GSU0935. The values of Z_1 and k_∞ were obtained with Equation 5.4. The reduction potentials extrapolated to infinite ionic strength were obtained as described by Pedro Quintas *et al.* [228]

	GSU0582			GSU0935		
	pH 6.0	pH 7.0	pH 8.0	pH 6.0	pH 7.0	pH 8.0
Z_1	-1.5	-1.4	-1.7	-2.1	-2.3	-3.8
k_∞ ($M^{-1}s^{-1}$)	6.8×10^7	6.7×10^7	6.4×10^7	2.0×10^7	1.8×10^7	2.0×10^7
E_m^∞ (mV)	-129	-138	-144	-151	-173	-178

The effective charge of GSU0935 is slightly more negative than that of GSU0582, suggesting the presence of a higher number of acidic groups in the region where $SO_2^{\bullet-}$ approaches the heme. The larger negative charge also contributes to the smaller rate constants measured for GSU0935 at typical ionic strengths, but should not contribute to the difference between the rate constants of GSU0935 and GSU0582 at infinite ionic strength. The effective charge of GSU0582 hardly changes in the pH range 6.0 to 8.0, whereas the charge of GSU0935 changes by at least one unit between pH 7.0 and pH 8.0. These results indicate that in GSU0935 there is at least one ionizable group that deprotonates in this pH range that is not present in GSU0582. This group affects the electrostatic interaction between $SO_2^{\bullet-}$ and the protein and may also affect the reduction potential of the heme, depending on its location.

The effect of the driving force can be separated from the effect of the electrostatic interactions by comparing the ratios of rate constants at infinite ionic strength, obtained from the fit, with ratios of rate constants calculated for a given driving force, using Marcus theory for electron transfer [241] (Equation 5.8) [228]:

$$\frac{k_{ET}^{pHi}}{k_{ET}^{pHj}} = \exp\left(\frac{(E_{GSU}^{pHi} - E_{GSU}^{pHj})F}{2RT}\left(1 + \frac{E_{SO2}F}{\lambda} - \frac{(E_{GSU}^{pHi} + E_{GSU}^{pHj})F}{2\lambda}\right)\right) \quad (5.8)$$

In Equation 5.8 the E_{GSU} are the reduction potentials of the heme sensor domains at different pH values extrapolated to infinite ionic strength (Table 5.3). A value of λ = 0.7 eV was used for the reorganization energy [242] and $E_{SO_2}^{\bullet -}$ = -0.3 V. For each sensor, the small variation in reduction potentials extrapolated to infinite ionic strength correlates well with the small variation in rates also extrapolated to infinite ionic strength (Table 5.4).

Table 5.4 – Comparison between measured and predicted rate constants for each sensor domain. Ratios of the rate constants at different pH values (given as subscripts), extrapolated to infinite ionic strength, for each sensor (labeled as experimental) are compared with the expected ratios calculated using Marcus theory for electron transfer (Equation 5.8) with reduction potentials extrapolated to infinite ionic strength.

	GSU0582		GSU0935	
	Experimental	*Marcus*	*Experimental*	*Marcus*
k_7/k_6	1.0	0.9	0.9	0.7
k_8/k_7	1.0	0.9	1.1	0.9

However, comparison of the two sensors (Table 5.5) shows that the ratio of their rate constants extrapolated to infinite ionic strength cannot be explained solely on the basis of the difference in driving force.

Table 5.5 – Comparison of the rate constants of the two sensor domains. The ratios of the rate constants of the two sensors, extrapolated to infinite ionic strength at each pH value are compared with the expected ratios determined using Marcus theory for electron transfer. Equation 5.8 was used with the two sensors in place of two pH values and with reduction potentials extrapolated to infinite ionic strength.

$k^{GSU0582}/k^{GSU0935}$ infinite ionic strength		
pH	experimental	Marcus
6.0	3.4	1.4
7.0	3.7	1.7
8.0	3.2	1.7

Since the difference in charge should have no effect at infinite ionic strength, it can be concluded that there are other structural factors that favor the interaction of $SO_2^{\bullet-}$ with GSU0582 when compared to GSU0935.

5.4.3 Structural correlations

The thermodynamic and kinetic studies for sensors GSU0582 and GSU0935 indicated that: (i) the dominant charged residues in the vicinity of the hemes are negative; (ii) the effective charge of GSU0935 is more negative than that of GSU0582; (iii) in GSU0935 there is at least one ionizable group with a pK_a between 7 and 8 that is not present in GSU0582, and (iv) the midpoint reduction potentials of both sensors decrease with increasing pH, with GSU0935 sensor most affected. In order to rationalize these inferences it was then moved to a detailed structural analysis of both sensors, in particular of their heme environment, noting that the charged groups which affect the interaction with $SO_2^{\bullet-}$ are not necessarily the same as those which affect the reduction potential. The crystal structures of GSU0582 and GSU0935 sensors were determined and showed that they form swapped-dimers with a PAS-type fold formed by polypeptide segments of the two monomers [115]. Also, each heme has axial ligands provided by both monomers. In solution, under the experimental conditions used in this work, the monomer-dimer equilibrium is shifted towards the monomeric form as previously described [243]. Models of GSU0582 and GSU0935 monomers in solution were previously constructed from the respective crystal structures [115] and were used in this work to rationalize the thermodynamic and kinetic observations.

The comparison between the structures of the swapped-dimers and monomers is depicted in Figure 5.8.

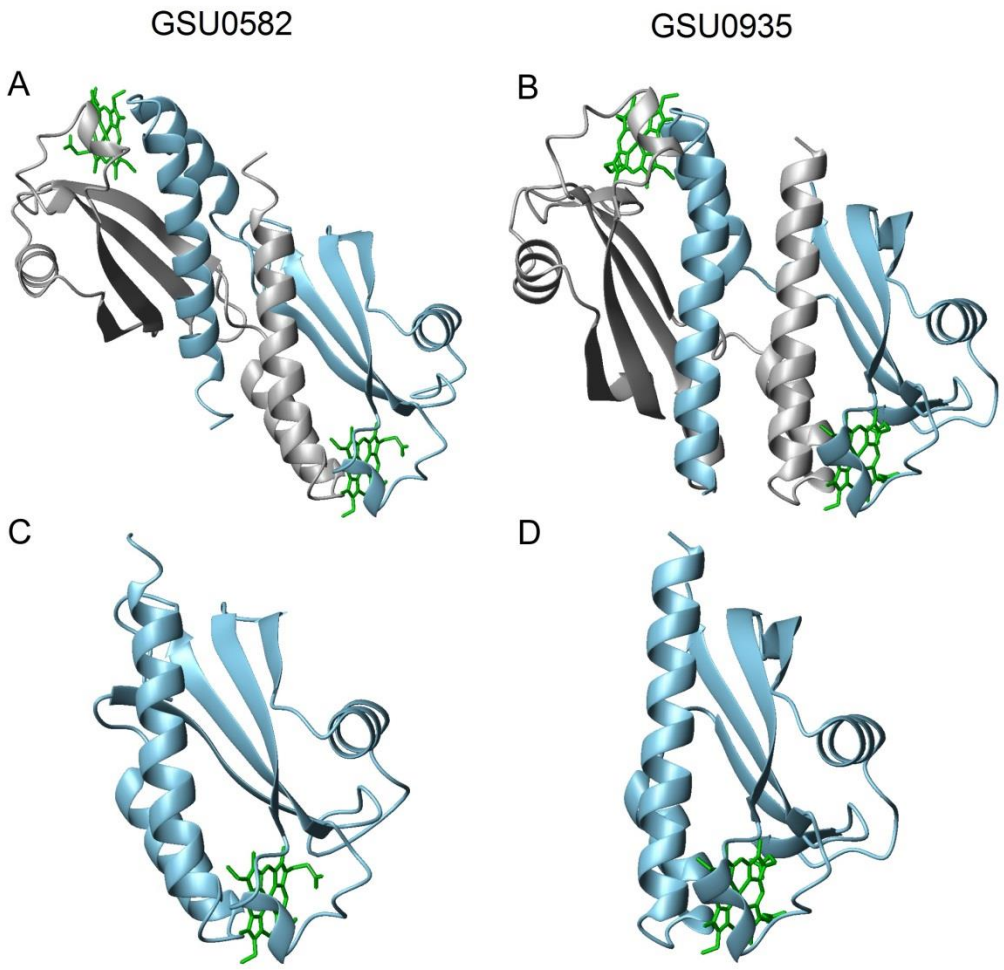

Figure 5.8 – Ribbon diagram of swapped dimers of heme sensors GSU0582 (A) and GSU0935 (B). The structures of sensors were retrieved from the PDB. In the dimers the monomers are highlighted blue and grey and are presented in panels C and D, respectively. Figures were produced using MOLMOL [244].

Despite the fact that some amino acid residues belong to a different polypeptide chain in the swapped dimer, the heme environment is expected to be similar in the monomers of both proteins (Figure 5.8). Although the two heme sensor domains have similar structural folds, their distinct primary sequences (Figure 1.13) results in different distributions of electrostatic potential at the surfaces (Figure 5.9A and B).

However, both sensors show a predominantly negative electrostatic surface in the region of the heme groups (Figure 5.9), which explains the observed increase in the reduction potentials with the ionic strength for both sensors.

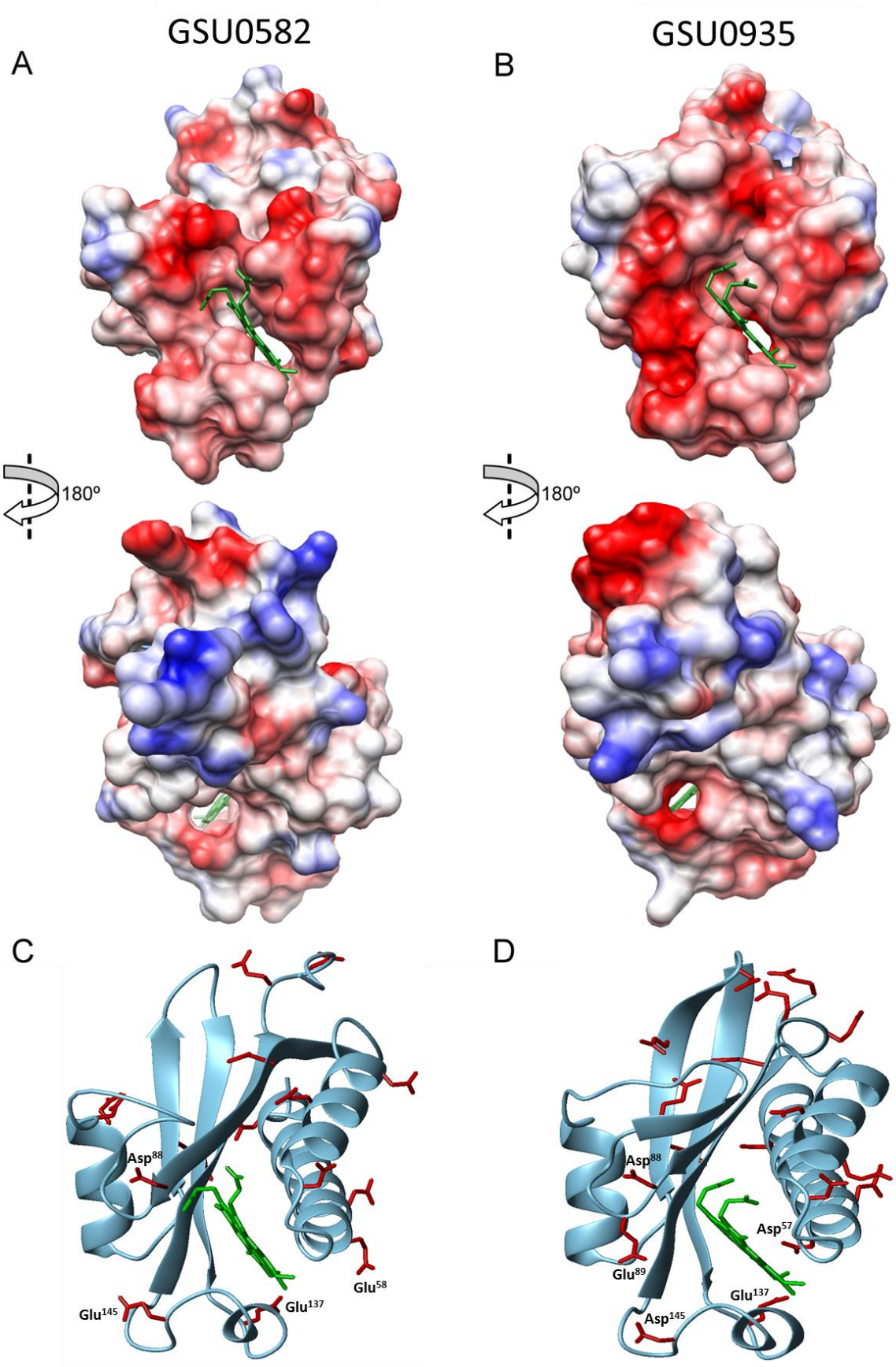
GSU0582
GSU0935
A
B
180º
180º
C
D
Asp88
Glu58
Glu137
Glu145
Asp88
Glu89
Asp57
Glu137
Asp145

Figure 5.9 – Surface electrostatic potential around the heme region calculated by the program CHIMERA [74] for sensors GSU0582 (A) and GSU0935 (B). Red indicates negative and blue indicates positive potential. The heme groups are colored green. Ribbon diagram of GSU0582 (C) and GSU0935 (D) sensor domains. The peptide chain and the hemes are colored blue and green, respectively. The negatively charged residues are shown in red and those in the vicinity of the heme groups are labeled according to the amino acid sequence numbering. Figures were produced using MOLMOL [244].

A detailed comparison of the negative charges in the vicinity of the heme groups shows that in GSU0935 there is a glutamic acid (Glu^{89}) (accessible surface area of the Glu^{89} side chain is 59 $Å^2$), which has no counterpart in GSU0582, with the equivalent residue being an Ala. An aspartic acid (Asp^{57}) in GSU0935 is within van der Waals contact distance pointing towards the heme and is fairly buried (accessible surface area of the Asp^{57} side chain is 7 $Å^2$), whereas the equivalent residue is Gly in GSU0582. There is a glutamic acid residue present in GSU0582 at position 58 (Glu^{58}) fully exposed to the solvent (accessible surface area of the Glu^{58} side chain is 68 $Å^2$), which is farther from heme with its side chain pointing away from the heme (Figure 5.9C, D). The heme propionates of the two sensor domains also show some structural differences: in GSU0582 both heme propionates are fairly exposed to the solvent (surface exposure of propionates P17 and P13 are 49.6 $Å^2$ and 92.2 $Å^2$, respectively), whereas in GSU0935 heme propionate P17 is rather buried when compared to heme propionate P13 (surface exposure of propionates P17 and P13 are 18.6 $Å^2$ and 77.9 $Å^2$, respectively). Therefore, sensor GSU0935 has a more negative electrostatic surface around the heme group, which agrees with the lower reduction potentials and their higher ionic strength dependence, which is more noticeable at pH 8.0 as shown in Figure 5.4.

The positive slope of the kinetic data in Figure 5.7 was also indicative of a negative surface potential around the heme in both sensors. The effective charges calculated from these data (Table 5.3) are also consistent with the more negative environment of the heme in GSU0935 (panels A and B of Figure 5.9). The kinetic data also suggests the existence of an ionizable group with a pK_a value in the pH range 7.0-8.0 in GSU0935 that is not present in GSU0582. This group could also be responsible for the stronger redox-Bohr effect observed in GSU0935. However, the pK_a observed in the rate constant is macroscopic (Equation 5.7) and not necessarily the property of a single ionizable group. This pK_a will be shifted to a higher pH by the statistical effect and also by any interaction between the groups, and so the pK_a of the additional group in GSU0935 may be below 7.0.

Given the structural differences described, it is also possible that different acid/base groups give major contributions either to the redox-Bohr effect or to the repulsive interaction with $SO_2^{\bullet-}$. It is likely that the two more buried carboxylic groups (Asp^{57} and propionate P17) have a greater influence in the reduction potential of the heme, while the exposed Glu^{89} should play a bigger role in the electrostatic interaction with the electron donor.

Putting together thermodynamic, kinetic and structural information, it may be concluded that, although it is possible to simulate the pH dependence of the reduction potentials of the two sensors with a single acid/base group, it is probable that an additional group plays a part in GSU0935.

Therefore, both sensors have at least one acid/base group that accounts for a difference between pK_{red} and pK_{ox} of about 1 pH unit and GSU0935 has at least a second ionizable group that accounts for the rest of the redox-Bohr effect.

The comparison of the kinetic properties of the two sensors also showed that the difference in absolute rate constants measured cannot be fully explained by the difference in charge and driving force and there must be another structural factor involved. Since the reducing agent is a small inorganic ion, the solvent exposure of the heme may play a significant role [245]. The solvent exposure of the heme in the sensor domains was calculating with the program surface using default parameters within ccp4 package [246], and the values obtained were 234 Å for GSU0582 and 180 Å for GSU0935. The higher solvent exposure of the heme in sensor domain GSU0582 could account for the fact that the reduction of GSU0582 is nearly twice as fast as GSU0935, when charge effects and driving force are discounted (Table 5.5).

5.5 Conclusions

The detailed thermodynamic and kinetics characterization of periplasmic sensor domains of the methyl-accepting chemotaxis proteins GSU0582 and GSU0935 from *G. sulfurreducens* provided for the first time a rationalization for the co-existence of two methyl-accepting chemotaxis proteins with remarkably similar spectroscopic features and structural folds. The results obtained in the *G. sulfurreducens* physiological pH range for growth showed that the properties of the sensor domains GSU0935 and GSU0582 are different. The thermodynamic studies showed that the sensor domain GSU0935 displayed more negative reduction potentials, which are more strongly modulated by the pH (redox-Bohr effect) and ionic strength. Similarly, the kinetic studies showed that the rate constants of the sensor GSU0935 are smaller, compared to those of GSU0582 and are considerably more affected by the pH or ionic strength. The analysis of the structure of the two sensors allowed us to rationalize the thermodynamic and kinetic data and to understand the functional differences between the two sensors at molecular level: (i) the electrostatic surface in the heme neighborhoods is negative in both sensors, as determined from the kinetic studies with a negatively charged reducing agent, since the rate constants increase with the ionic strength; (ii) the more negative electrostatic surface around the heme group of sensor GSU0935 correlates with the more negative reduction potentials, smaller rate constants, and with the larger negative charge predicted from the kinetic studies; (iii) the solvent exposure of the GSU0582 heme group is larger, compared to that of GSU0935, and might contribute to the higher rate constants observed in the former protein; (iv) the greater effective negative charge around the heme group of GSU0935 may contribute to the higher redox-Bohr effect observed in this sensor domain, and might be explained by the close proximity of aspartic acid (Asp^{57}) and propionate P17; (v) the kinetic data of GSU0935 predicts an increase in the negative charge between pH 7.0 and 8.0, which could be explained by

the deprotonation of the side chain of glutamic acid (Glu^{89}), an exposed residue in the middle of a highly negative surface potential, that has no counterpart in GSU0582. Overall, the distinct functional properties described here for the two heme sensor domains from *G. sulfurreducens* correlate with the structural data available and provide an excellent example of how functional properties of structurally related proteins from the same microorganism could be modulated by key residues placed in strategic positions. Finally, the good correlation observed between the thermodynamic and kinetic analysis and the available structural data, demonstrates that the strategy presented here for the two methyl-accepting chemotaxis proteins GSU0582 and GSU0935 from *G. sulfurreducens*, and elsewhere for cytochrome *c*" from *Methylophylus methylotrophus* [228] where the electrostatic interaction with the electron donor is attractive, can be used to obtain information on the electrostatic environment of the heme groups in the absence of structural models. This information might be important to understand, or predict, protein-protein interactions that are fundamental to *in vivo* electron transfer.

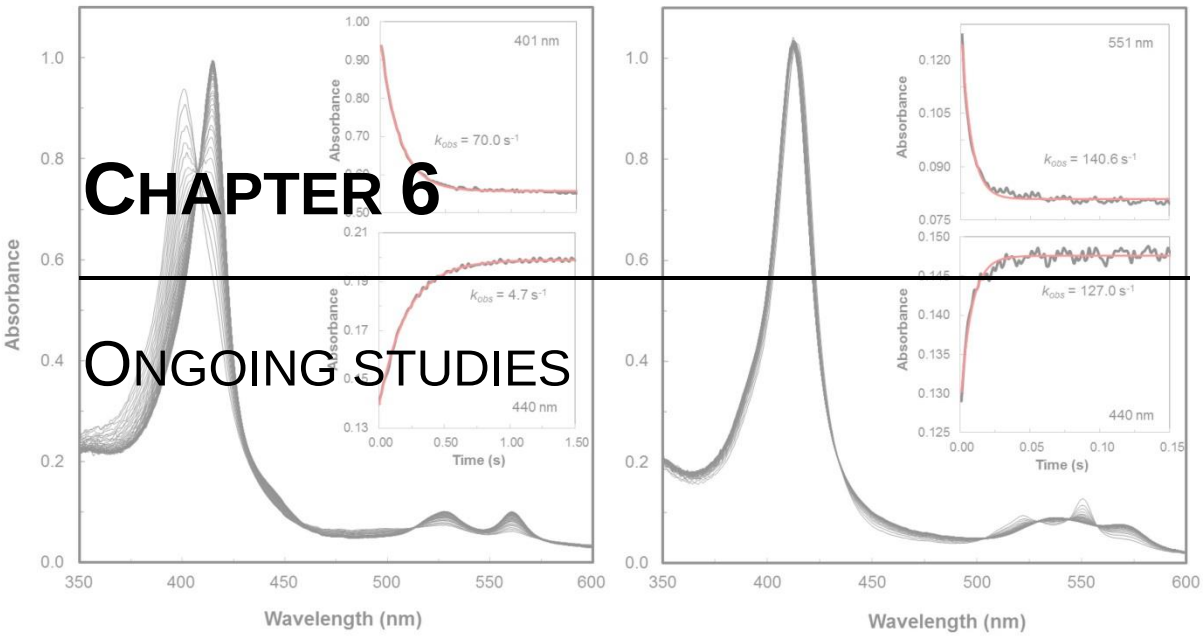

CHAPTER 6

ONGOING STUDIES

6. ONGOING STUDIES

Despite the contribution of this Thesis to the characterization of heme methyl-accepting chemotaxis sensors from *G. sulfurreducens*, much remains unclear. Therefore, complementary studies are needed to further elucidate the signal transduction mechanisms in these proteins. One interesting aspect requiring further investigation encompasses the elucidation of the structural and functional role of specific residues. Particularly promissing targets encompasses (i) Met^{60} that axially coordinates the heme iron in the reduced form and might be responsible for the redox-linked ligand switch and (ii) negatively charged residues found in GSU0935 sensor domain, which have no counterpart in GSU0582. A second important aspect would involve the study of the kinetic features of CO and NO binding mechanisms. Previous studies showed that heme *c* iron has the ability to bind both CO and NO in ferrous (Fe^{2+}) form and NO in the ferric (Fe^{3+}) form. In both cases, the reactions are fully reversible. A detailed kinetics study of such binding would contribute to elucidate at the molecular level how these putative signaling molecules might initiate the adequate response in *G. sulfurreducens*.

6.1 Preliminary characterization of mutated forms of GSU0582 and GSU0935 sensor domains

The spectroscopic characterization of GSU0582 and GSU0935 sensor domains revealed that the heme groups in both proteins are high-spin in the oxidized form and becomes low-spin after reduction. The change in the redox state of the sensor domains is coupled to a heme state/coordination alteration [115, 168] which might be related to the coordination of a methionine residue (Met^{60}) at the heme distal position in the reduced form. This spin state interconversion suggests an important role for this residue in trigger the signal transduction. In order to study the role of Met^{60}, this residue was replaced by site-directed mutagenesis by an alanine in both GSU0582 and GSU0935 (Appendix A.1.1).

The structural differences between the two sensor domains, as described in Chapter 5, showed that GSU0935 has two extra negatively charged residues in the vicinity of the heme group, which have no counterpart in GSU0582: Glu^{89} and Asp^{57}. Aspartic acid (Asp^{57}) is less exposed compared to glutamic acid (Glu^{89}) and it was suggested that its carboxylic group might have a role in the modulation of the heme reduction potential of GSU0935. Thus, to investigate this aspect, both residues were replaced by a positively charged amino acid (lysine) or by a neutral one (asparagine or glutamine), according to the rationaly detailed in Figure A.1 (Appendix A1.1). In

order to take into consideration the impact of both mutations together in the sensor domains potential, the following double mutants for GSU0935 were also produced: $Asp^{57}Lys/Glu^{89}Lys$; $Asp^{57}Lys/Glu^{89}Gln$, $Asp^{57}Asn/Glu^{89}Lys$ and $Asp^{57}Asn/Glu^{89}Gln$.

Typically, the expression yields for the mutated proteins were substantially lower compared to native proteins. For some mutants, no expression was obtained (Table 6.1).

Table 6.1 – Summary of the expression trials for the different mutated heme sensor domains. The mutants that showed no expression are indicated by ⊖. The mutants whose expression could be achieved are represented by the ⊕ symbol. - : not done.

Mutant	GSU0582	GSU0935
$Met^{60}Ala$	⊖	⊕
$Asp^{57}Lys$	-	⊕
$Asp^{57}Asn$	-	⊖
$Glu^{89}Lys$	-	⊕
$Glu^{89}Gln$	-	⊕
$Asp^{57}Lys/Glu^{89}Lys$	-	⊕
$Asp^{57}Lys/Glu^{89}Gln$	-	⊕
$Asp^{57}Asn/ Glu^{89}Lys$	-	⊖
$Asp^{57}Asn/ Glu^{89}Gln$	-	⊖

For the mutants for which enough expression was obtained, their folding was probed by CD spectroscopy (Figure 6.1). Compared to the CD spectrum of the wild-type sensor domain GSU0935, the mutants show similar features, except for $Met^{60}Ala$, suggesting that these proteins are folded. However, the spectra are not identical, which might indicate slightly variation on the sample conformer's heterogeneity. This is also supported by the slightly less cooperative transitions between the folded and unfolded states (Figure 6.1). The CD spectrum of $Met^{60}Ala$ mutant revealed a substantial variation at 208 nm indicating a loss of the helical secondary structure. This is also confirmed by the comparison of the thermal denaturation curve obtained for these mutants and that of the wild-type protein. In fact, the highly monotonic thermal denaturation curve of the mutant $Met^{60}Ala$ indicates a higher heterogeneity of the sample, which also explains the higher tendency of this mutant to aggregate upon purification. Therefore, these results corroborate the assumption that Met^{60} has a crucial role not only for the functional mechanism of these sensors but also for their correct folding.

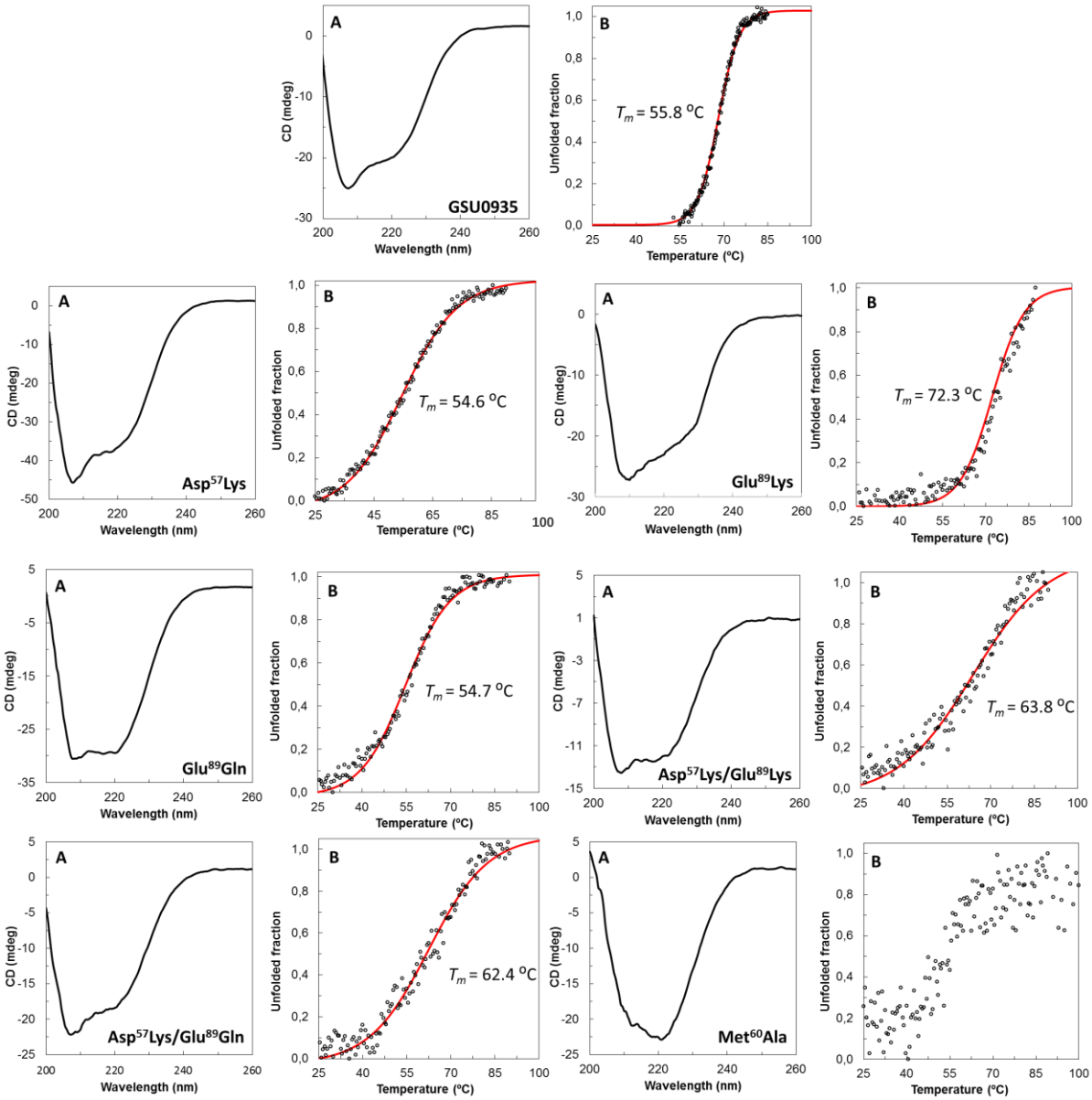

Figure 6.1 – Far-UV CD (A) and thermal denaturation (B) of GSU0935 mutants. For comparison the values obtained for the wild-type protein are also included. The thermal denaturation was followed by monitoring the variation of the CD signal at 222 nm, a wavelength where both α-helices and β-sheets contribute significantly. The red lines represent the fitting to the two-states model described in Chapter 4. The midpoint denaturation temperature values (T_m) are indicated.

In order to explore this hypotheses and also to evaluate the impact of the other mutations in the sensor domain GSU0935, redox titrations followed by visible spectroscopy were carried out, except for Met^{60}Ala (Figure 6.2).

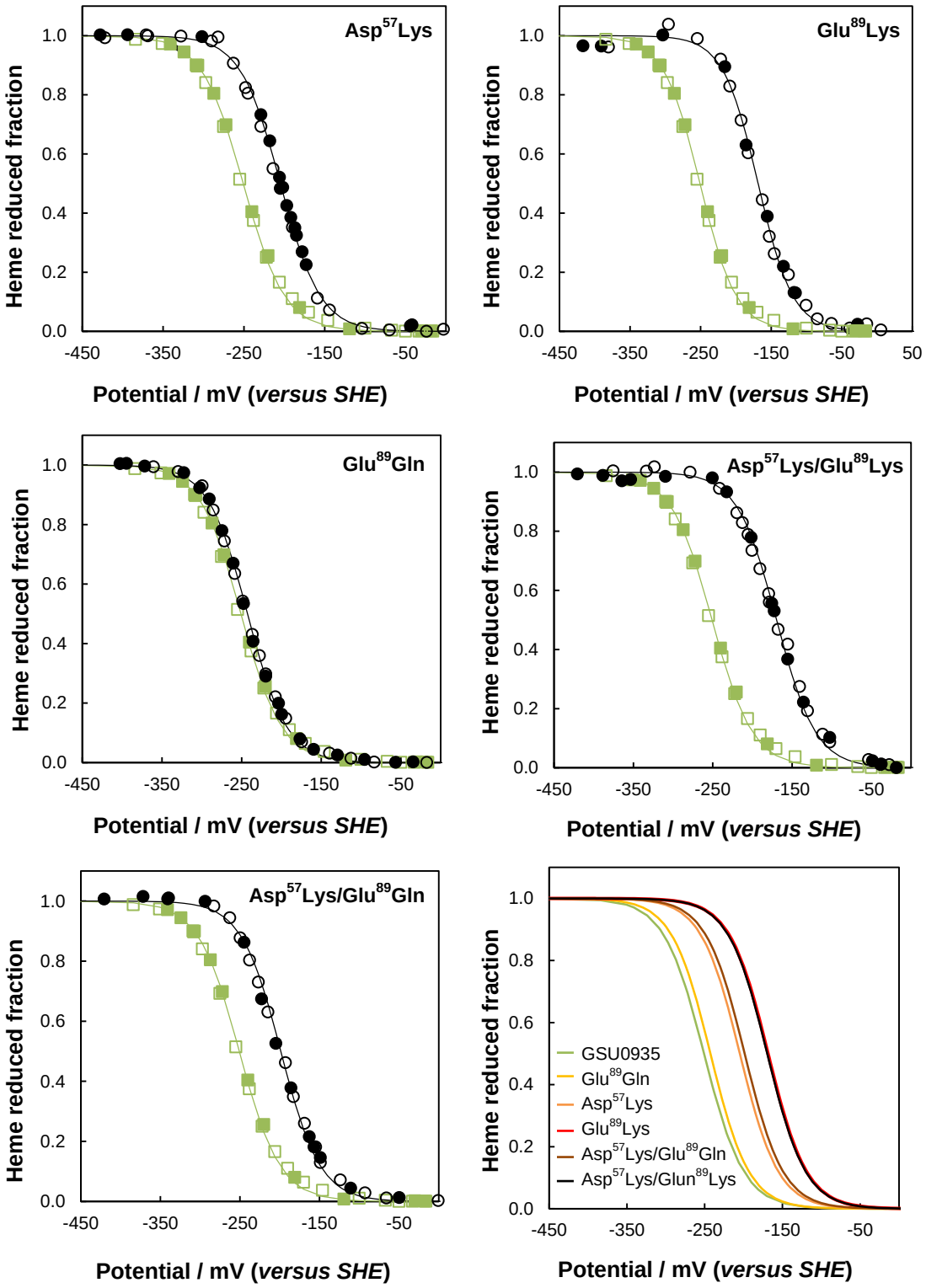

Figure 6.2 – Redox titrations followed by visible spectroscopy for the mutants of the GSU0935 sensor domain at 100 mM Tris-maleate buffer at pH 8.0. The void and solid symbols represent the data points in oxidative and reductive titrations, respectively. The lines are the results of the fit to the Nernst equation for one-electron reduction. The reduction potentials obtained, relative to standard hydrogen electrode (SHE), are listed in Table 6.2. The squares and circles represent the native and the mutant proteins, respectively.

Similarly to the behavior of the native proteins, no hysteresis was observed, as the reductive and oxidative curves are superimposable, indicating that the redox process is fully reversible. The midpoint reduction potential values obtained from the fitting of the Nernst equation to each curve are indicated in Table 6.2.

Table 6.2 – Midpoint redox potentials in mV (*versus SHE*) for heme sensor domain GSU0935 mutants (pH 8.0). For comparison the midpoint redox potentials values of the wild-type sensor domains GSU0935 and GSU0582 are provided: -156 mV (GSU0582) and -251 mV (GSU0935).

Protein	Em (mV)
$Asp^{57}Lys$	-205
$Glu^{89}Lys$	-169
$Glu^{89}Gln$	-243
$Asp^{57}Lys/Glu^{89}Lys$	-170
$Asp^{57}Lys/Glu^{89}Gln$	-199

The analysis of Table 6.2 showed that the significant changes on the reduction potential values are observed when a negative charge is replaced by a positive one at position 57 or 89. As mentioned in Chapter 5, these two negatively charges are not present in the sensor domain GSU0582. Therefore, the decrease of the reduction potential in Asp^{57} and Glu^{89} mutants reinforces the hypothesis that the higher reduction potential observed for heme sensor domain GSU0582 is related with the less negative electrostatic surface around the heme (see Figure 5.9). In the absence of significant conformational changes, it is expected that the presence of two extra positive charges in the vicinity of the heme group of sensor GSU0935 would have a higher effect on the reduction potential. However, this is not the case for the double mutant $Asp^{57}Lys/Glu^{89}Lys$. In order to understand this observation, the effect of these substitutions in the predicted structure of the sensor domain GSU0935 was evaluated using *in-silico* modeling studies. Replacement of Asp^{57} by lysine showed that the side chain has steric conflicts with the Arg^{139}. The Arg^{139} is displaced and the salt bridge formed with Glu^{137} is disrupted. The lysine could also interact with Glu^{137}, however the salt bridge interaction Arg-Glu is superior compared to Lys-Glu. Apparently, this is a very crowded region and the presence of a lysine could force local structural changes and might explain why in the double mutant the effect of having two positive charges is not additive.

6.2 Kinetic characterization of nitric oxide binding to GSU0582 and GSU0935 sensor domains

The kinetic characterization of the nitric oxide binding to the *G. sulfurreducens* sensor domains may provide insights to understand the biological function of these proteins. These studies were performed in the oxidized and reduced forms of GSU0582 and GSU0935 in anaerobic conditions through stopped-flow techniques. An excess of ligand was used to ensure that the reaction occurred under pseudo-first-order conditions. The reactions were followed by measuring the change in absorbance with time at different wavelengths chosen by inspection of spectra obtained with the diode array, and corresponding to different mixtures of the NO concentrations. The spectra of GSU0935 and GSU0582 sensor domains are identical and can be typified by that of GSU0935 (Figure 6.3).

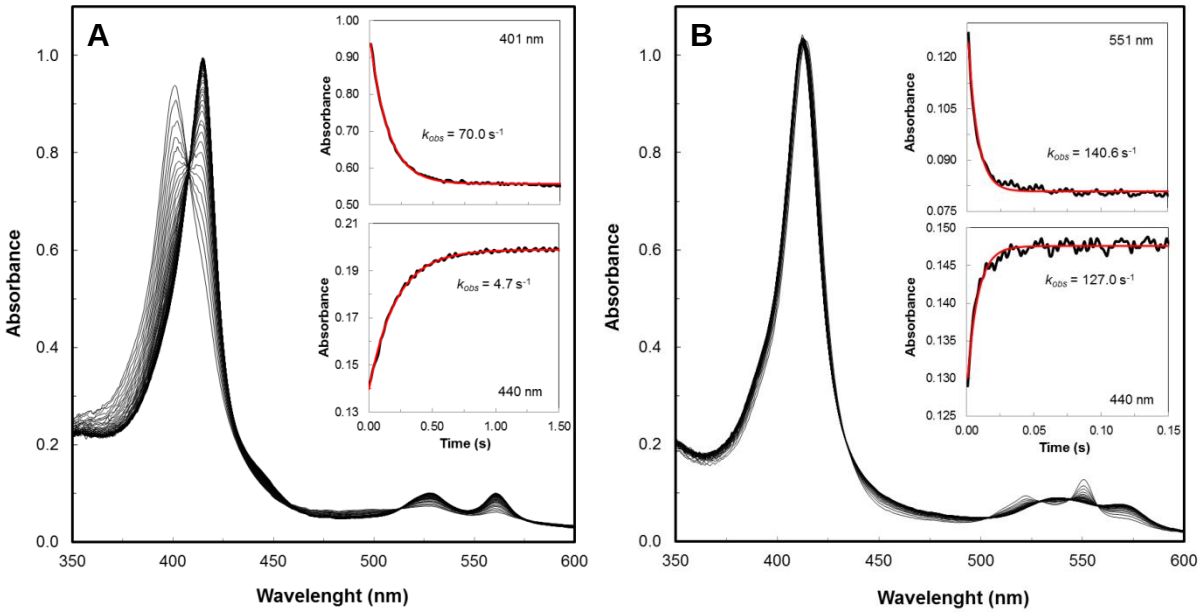

Figure 6.3 – Evolution of the UV-visible spectrum during NO binding experiments to the sensor domain GSU0935. (A) Experimental spectra obtained in the oxidized form. (B) Experimental spectra obtained in the reduced form. Insets represent the time-course traces at 401 (oxidized), 551 (reduced) and 440 nm for the reaction with 295 µM NO (black line). The red lines result from fitting the data using a single exponential.

Each trace was fitted with single exponentials to obtain first-order rate constants k_{obs} for the NO binding. The second-order rate constant for the binding of NO was determined from the slope of the straight line obtained by plotting the values of k_{obs} at different NO concentrations (Figure 6.4).

Two distinct rate values were obtained (Figure 6.4A and B), which indicate that the NO binding in the oxidized state occurs *via* two distinct reactions in both sensor domains.

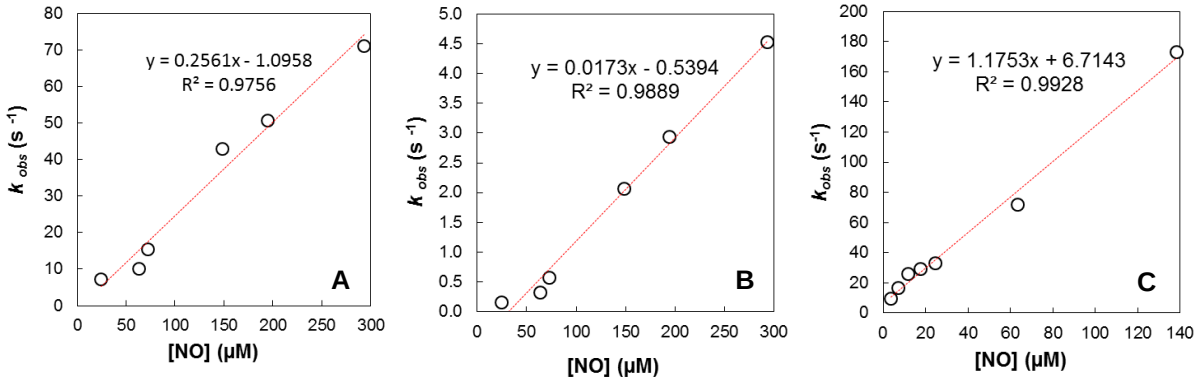

Figure 6.4 – Dependence of k_{obs} on the concentration of NO in GSU0935 sensor domain. Values of k_{obs} were obtained by fitting time-course traces to exponentials. Each point represents an average of separate fittings at different wavelengths. (A) k ($\mu M^{-1}s^{-1}$) obtained from the rapid reaction identified in oxidized form. (B) k ($\mu M^{-1}s^{-1}$) obtained from the slow reaction identified in oxidized form. (C) k ($\mu M^{-1}s^{-1}$) obtained from the reaction in the reduced form. The second-order constant rates of the sensor domains were the follow: GSU0582: 0.060 and 0.004 $\mu M^{-1}s^{-1}$ in the oxidized and 2.376 $\mu M^{-1}s^{-1}$ in the reduced form; GSU0935: 0.256 and 0.017 $\mu M^{-1}s^{-1}$ in the oxidized and 1.175 $\mu M^{-1}s^{-1}$ in the reduced form.

The different values obtained suggest a mechanism by which NO binds to the oxidized sensor domains, forming a NO-Fe-His intermediate that is then converted to a NO-Fe form, with the detachment of the axial histidine (Figure 6.5).

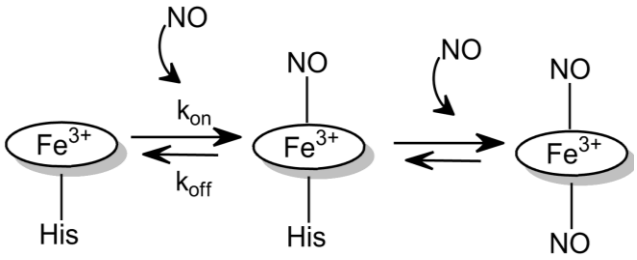

Figure 6.5 – Proposed mechanism for NO binding to oxidized GSU0582 and GSU0935 sensor domains.

In the reduced form, the NO binding reaction is even faster than those observed for the oxidized state (Figure 6.4C). Therefore, in the reduced form a mechanism that comprises the replacement of the methionine by the NO molecule at the distal site is proposed (Figure 6.6).

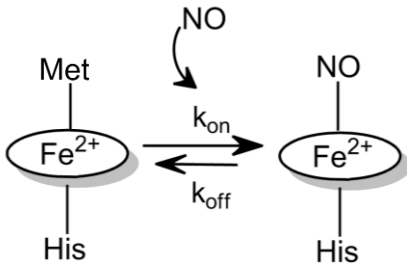

Figure 6.6 – Proposed mechanism for NO binding to reduced GSU0582 and GSU0935 sensor domains.

Further kinetics and binding studies may also contribute to identify and elucidate the binding mechanism of other diatomic molecules that may act as physiological signal for these sensor domains.

CHAPTER 7

CONCLUDING REMARKS

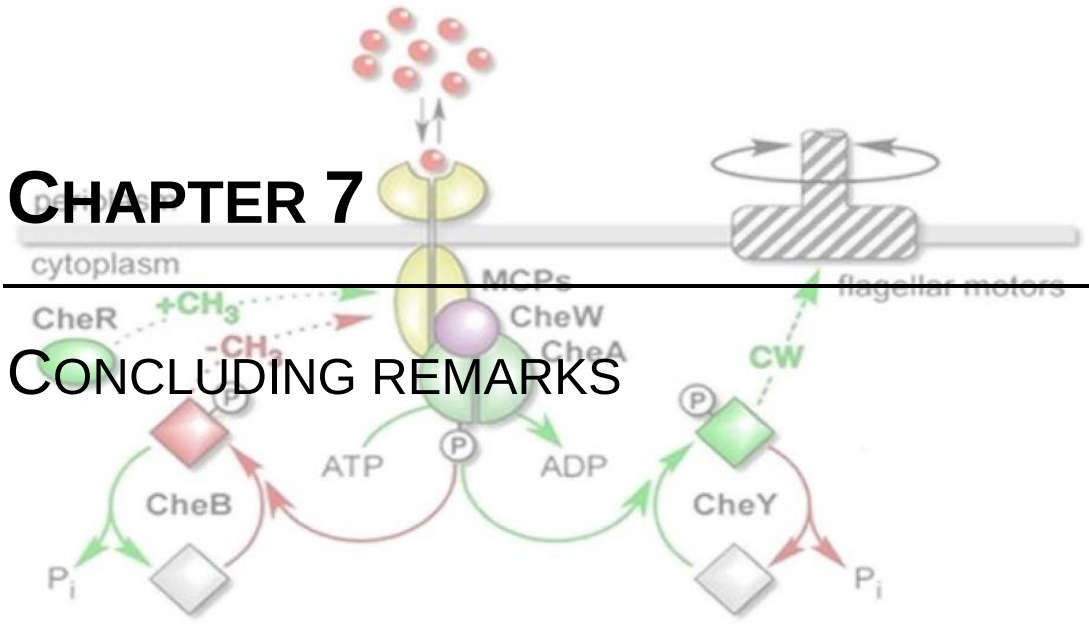

7. CONCLUDING REMARKS

Sensing environmental signals and trigger efficient adaptation responses are key features for cell survival and proliferation. Bacteria from the *Geobacter* genus have the ability to survive in different challenging environments using their versatile respiratory chain and chemotaxis systems. Consistent with the complexity of the habitats in which *G. sulfurreducens* proliferate, this bacterium has a large number of chemosensory systems and a diverse repertoire of methyl-accepting chemotaxis proteins. Two of these proteins, GSU0582 and GSU0935, which are members of a new family of chemotaxis sensor proteins, contain a periplasmic PAS-like sensing domain with a heme *c*-binding motif. Apart from the inherent interest to comprehend the general bases underlying signaling transduction mechanisms, these systems are particularly relevant in the case of *G. sulfurreducens* since this microorganism is presently targeted for many practical applications, including bioremediation of radioactive and toxic metals in contaminated subsurface environments and bioenergy production in microbial fuel cells.

The study of the methyl-accepting chemotaxis proteins GSU0582 and GSU0935 yielded the first important steps in 2008 with the determination of the crystal structure of their heme sensor domains in the oxidized form [115]. Despite their moderate sequence identity (40%) the two sensor domains have similar structures and form swapped dimers with a PAS-like fold. Likewise, the spectroscopic characteristics of the two proteins also revealed similar features [115, 168]. The heme groups are high-spin in the oxidized form and become low-spin after reduction. This also involves the binding of a methionine residue to the distal position of the heme.

The main aim of this Thesis was to contribute to the understanding of the signaling transduction pathways in *G. sulfurreducens*, particularly those involving the two methyl-accepting chemotaxis proteins GSU0582 and GSU0935. Additionally, it was also aimed to provide a functional interpretation for the co-existence of these two very similar methyl-accepting chemotaxis proteins in *G. sulfurreducens*. In order to accomplish these goals, several spectroscopic techniques were used, including NMR, UV-visible and CD, together with kinetics and potentiometric measurements.

NMR was explored as a tool to monitor conformational changes occurring either within the heme group vicinity or through the entire polypeptide chain (Chapter 3). Although the co-existence of two conformations in solution impaired the achievement of such goal, this approach and the successfully isotopic labeling of GSU0935 set up the experimental design for future studies.

The thermal and chemical stability studies (Chapter 4) as well as the kinetic measurements and UV-visible redox titrations (Chapter 5) revealed important differences between the GSU0582 and GSU0935 sensor domains. The stability studies showed that GSU0582 is more stable (ΔG = 26.3 kJ.mol^{-1} *versus* ΔG = 14.6 kJ.mol^{-1} for GSU0935), correlating to the distinct levels of intrinsic

disorder in the two proteins (13% for GSU0582; 25% for GSU0935). The fact that the heme moiety undergoes conformational changes that match those occurring at the global protein structure suggests that signaling at the heme group induces conformational changes that rapidly propagate to the protein structure, an effect which is directly linked to the signal transduction mechanism.

Another striking result from the work presented in this Thesis is the midpoint reduction potentials determined for each heme sensor within the *G. sulfurreducens* physiological pH range. The negative values of these reduction potentials are well framed within the typical anoxic subsurface environments in which *Geobacter* species predominate and with several studies on *G. sulfurreducens* biofilms with a reduction potential centered at around -150 mV, covering a potential working range of approximately 200 mV (Figure 7.1).

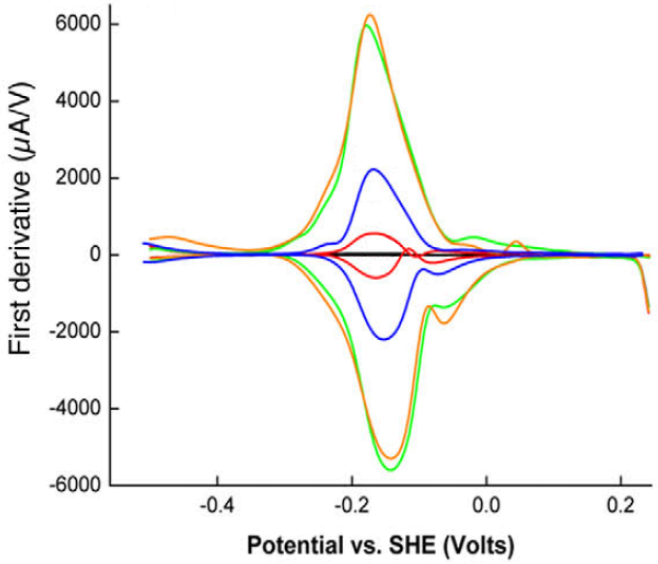

Figure 7.1 – First derivative plot of cyclic voltammetry (1 mV/s) of *Geobacter sulfurreducens* biofilms at different stages of growth. The plots were obtained at 22 h (red), 53 h (blue) and 72 h (green) of growth in vitamin-free anaerobic medium at pH 6.8 and 30 ºC [247], using acetate and fumarate as electron donor and acceptor, respectively. At 72 h, the medium was removed, replaced by fresh medium and the assay was repeated (orange). Adapted from [248].

Thus, the work described in this Thesis provides additional support to the hypothesis that changes in the redox potential coupled to heme spin state/coordination alterations may constitute the putative signal that triggers the transduction mechanism in these *G. sulfurreducens* sensors. One may speculate that this same mechanism may be common to other *c*-type heme based sensors in *G. sulfurreducens* and other bacteria. Therefore, besides the reversible binding of CO and NO to the heme group [168], the methyl-accepting chemotaxis proteins GSU0582 and GSU0935 probably work as redox sensors. The distinct midpoint reduction potential values of each sensor domain suggest that they are designed to function in different working potential ranges (with GSU0935 and GSU0582 operating respectively at lower and higher redox potentials), allowing

bacteria to trigger an adequate cellular response in diverse anoxic subsurface environments. These findings provide for the first time an explanation for the co-existence of these two very similar methyl-accepting chemotaxis proteins in *G. sulfurreducens*.

As mentioned above, *G. sulfurreducens* shows a large potential range, with the ability to preserve the homeostasis over this potential range and maintain its location. However, when subjected to environmental changes namely in the redox potential, bacteria activate their response mechanisms by methyl-accepting chemotaxis systems and move until they reach again optimal environment conditions (Figure 7.2).

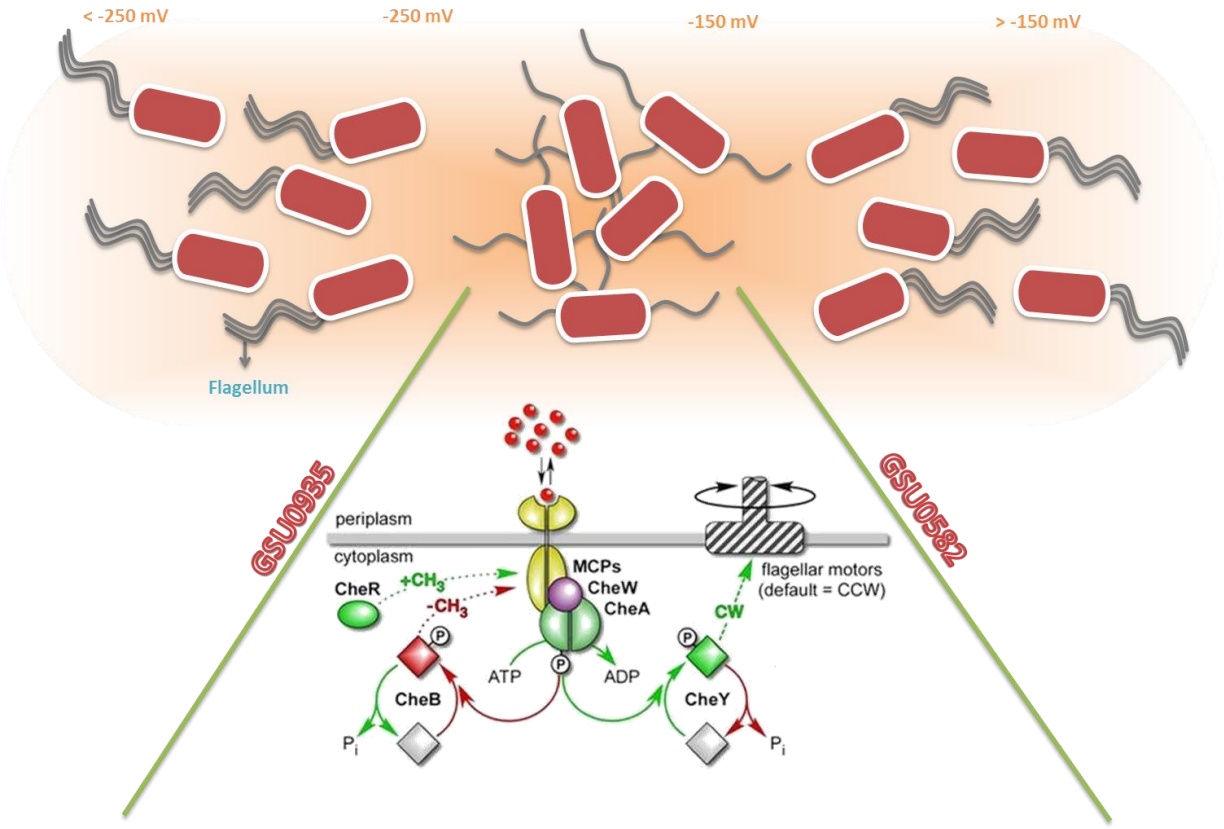

Figure 7.2 – Ilustration of the proposed signal transduction mechanism for *Geobacter sulfurreducens*. Signal sensing promotes the phosphorylation of CheA coupled by an adaptor protein CheW and consequently the phosphorylation of CheY, which brings about tumbling. The signal saturation blocks the phosphorylation of CheA and CheY, so tumbling is not promoted, and instead, running predominates. Then adaptation follows: CheB cause demethylation of the methylated MCP and CheR cause its methylation. CCW, counterclockwise rotation. Partially adapted from [249].

The results obtained in this Thesis provide additional understanding of bacterial signal transduction mechanisms by showing that two chemotaxis sensors of *G. sulfurreducens* operate over large and distinct potential ranges by linking changes in their heme redox state to structural alterations that are transmitted to the cytoplasmatic regulatory domains. The unveiling of the key features of these proteins opens new routes for the comprehension of the functional role of these novel heme-containing sensor proteins.

8. REFERENCES

[1] D.R. Zusman, A.E. Scott, Z. Yang, J.R. Kirby, Chemosensory pathways, motility and development in *Myxococcus xanthus*, Nat Rev Microbiol, 5 (2007) 862-872.

[2] J.J. Bijlsma, E.A. Groisman, Making informed decisions: regulatory interactions between two-component systems, Trends Microbiol, 11 (2003) 359-366.

[3] A.M. Stock, V.L. Robinson, P.N. Goudreau, Two-component signal transduction, Annu Rev Biochem, 69 (2000) 183-215.

[4] T. Mizuno, Compilation of all genes encoding two-component phosphotransfer signal transducers in the genome of *Escherichia coli*, DNA Res, 4 (1997) 161-168.

[5] J.S. Parkinson, E.C. Kofoid, Communication modules in bacterial signaling proteins, Annu Rev Genet, 26 (1992) 71-112.

[6] J.A. Hoch, Two-component and phosphorelay signal transduction, Curr Opin Microbiol, 3 (2000) 165-170.

[7] S.M. Wurgler-Murphy, H. Saito, Two-component signal transducers and MAPK cascades, Trends Biochem Sci, 22 (1997) 172-176.

[8] S. Li, A. Ault, C.L. Malone, D. Raitt, S. Dean, L.H. Johnston, R.J. Deschenes, J.S. Fassler, The yeast histidine protein kinase, Sln1p, mediates phosphotransfer to two response regulators, Ssk1p and Skn7p, EMBO J, 17 (1998) 6952-6962.

[9] J.A. Calera, X.J. Zhao, R. Calderone, Defective hyphal development and avirulence caused by a deletion of the SSK1 response regulator gene in *Candida albicans*, Infect Immun, 68 (2000) 518-525.

[10] J.A. Calera, R. Calderone, Flocculation of hyphae is associated with a deletion in the putative CaHK1 two-component histidine kinase gene from *Candida albicans*, Microbiology, 145 (1999) 1431-1442.

[11] T. Srikantha, L. Tsai, K. Daniels, L. Enger, K. Highley, D.R. Soll, The two-component hybrid kinase regulator CaNIK1 of *Candida albicans*, Microbiology, 144 (1998) 2715-2729.

[12] P. Thomason, D. Traynor, R. Kay, Taking the plunge. Terminal differentiation in *Dictyostelium*, Trends Genet, 15 (1999) 15-19.

[13] T. Urao, K. Yamaguchi-Shinozaki, K. Shinozaki, Two-component systems in plant signal transduction, Trends Plant Sci, 5 (2000) 67-74.

[14] P.M. Wolanin, P.A. Thomason, J.B. Stock, Histidine protein kinases: key signal transducers outside the animal kingdom, Genome Biol, 3 (2002) S3013.

[15] K. Wuichet, B.J. Cantwell, I.B. Zhulin, Evolution and phyletic distribution of two-component signal transduction systems, Curr Opin Microbiol, 13 (2010) 219-225.

[16] A.H. West, A.M. Stock, Histidine kinases and response regulator proteins in two-component signaling systems, Trends Biochem Sci, 26 (2001) 369-376.

[17] M.B. Miller, K. Skorupski, D.H. Lenz, R.K. Taylor, B.L. Bassler, Parallel quorum sensing systems converge to regulate virulence in *Vibrio cholerae*, Cell, 110 (2002) 303-314.

[18] M. Jiang, W. Shao, M. Perego, J.A. Hoch, Multiple histidine kinases regulate entry into stationary phase and sporulation in *Bacillus subtilis*, Mol Microbiol, 38 (2000) 535-542.

[19] R. Paul, S. Weiser, N.C. Amiot, C. Chan, T. Schirmer, B. Giese, U. Jenal, Cell cycle-dependent dynamic localization of a bacterial response regulator with a novel di-guanylate cyclase output domain, Genes Dev, 18 (2004) 715-727.

[20] J.J. Falke, R.B. Bass, S.L. Butler, S.A. Chervitz, M.A. Danielson, The two-component signaling pathway of bacterial chemotaxis: a molecular view of signal transduction by receptors, kinases, and adaptation enzymes, Annu Rev Cell Dev Biol, 13 (1997) 457-512.

[21] S. Iuchi, L. Weiner, Cellular and molecular physiology of *Escherichia coli* in the adaptation to aerobic environments, J Biochem, 120 (1996) 1055-1063.

[22] G. Unden, J. Bongaerts, Alternative respiratory pathways of *Escherichia coli*: energetics and transcriptional regulation in response to electron acceptors, Biochim Biophys Acta, 1320 (1997) 217-234.

[23] J.A. Hoch, Regulation of the phosphorelay and the initiation of sporulation in *Bacillus subtilis*, Annu Rev Microbiol, 47 (1993) 441-465.
[24] M. Perego, Kinase-phosphatase competition regulates *Bacillus subtilis* development, Trends Microbiol, 6 (1998) 366-370.
[25] I.J. Domian, K.C. Quon, L. Shapiro, The control of temporal and spatial organization during the *Caulobacter* cell cycle, Curr Opin Genet Dev, 6 (1996) 538-544.
[26] L. Shapiro, R. Losick, Protein localization and cell fate in bacteria, Science, 276 (1997) 712-718.
[27] J. Wu, A. Newton, Regulation of the *Caulobacter flagellar* gene hierarchy; not just for motility, Mol Microbiol, 24 (1997) 233-239.
[28] H.B. Kaplan, L. Plamann, A *Myxococcus xanthus* cell density-sensing system required for multicellular development, FEMS Microbiol Lett, 139 (1996) 89-95.
[29] M.J. Ward, D.R. Zusman, Regulation of directed motility in *Myxococcus xanthus*, Mol Microbiol, 24 (1997) 885-893.
[30] T. Krell, J. Lacal, A. Busch, H. Silva-Jimenez, M.E. Guazzaroni, J.L. Ramos, Bacterial sensor kinases: diversity in the recognition of environmental signals, Annu Rev Microbiol, 64 (2010) 539-559.
[31] J.T. Henry, S. Crosson, Ligand-binding PAS domains in a genomic, cellular, and structural context, Annu Rev Microbiol, 65 (2011) 261-286.
[32] V. Sourjik, H.C. Berg, Receptor sensitivity in bacterial chemotaxis, Proc Natl Acad Sci USA, 99 (2002) 123-127.
[33] C. Kim, M. Jackson, R. Lux, S. Khan, Determinants of chemotactic signal amplification in *Escherichia coli*, J Mol Biol, 307 (2001) 119-135.
[34] D.M. Faguy, K.F. Jarrell, A twisted tale: the origin and evolution of motility and chemotaxis in prokaryotes, Microbiology, 145 (1999) 279-281.
[35] J.R. Kirby, Chemotaxis-like regulatory systems: unique roles in diverse bacteria, Annu Rev Microbiol, 63 (2009) 45-59.
[36] J. Adler, M.M. Dahl, A method for measuring the motility of bacteria and for comparing random and non-random motility, J Gen Microbiol, 46 (1967) 161-173.
[37] E.N. Kort, M.F. Goy, S.H. Larsen, J. Adler, Methylation of a membrane protein involved in bacterial chemotaxis, Proc Natl Acad Sci USA, 72 (1975) 3939-3943.
[38] S.I. Bibikov, R. Biran, K.E. Rudd, J.S. Parkinson, A signal transducer for aerotaxis in *Escherichia coli*, J Bacteriol, 179 (1997) 4075-4079.
[39] A. Rebbapragada, M.S. Johnson, G.P. Harding, A.J. Zuccarelli, H.M. Fletcher, I.B. Zhulin, B.L. Taylor, The Aer protein and the serine chemoreceptor Tsr independently sense intracellular energy levels and transduce oxygen, redox, and energy signals for *Escherichia coli* behavior, Proc Natl Acad Sci USA, 94 (1997) 10541-10546.
[40] S.J. Kleene, M.L. Toews, J. Adler, Isolation of glutamic acid methyl ester from an *Escherichia coli* membrane protein involved in chemotaxis, J Biol Chem, 252 (1977) 3214-3218.
[41] S.J. Kleene, A.C. Hobson, J. Adler, Attractants and repellents influence methylation and demethylation of methyl-accepting chemotaxis proteins in an extract of *Escherichia coli*, Proc Natl Acad Sci USA, 76 (1979) 6309-6313.
[42] R.P. Alexander, I.B. Zhulin, Evolutionary genomics reveals conserved structural determinants of signaling and adaptation in microbial chemoreceptors, Proc Natl Acad Sci USA, 104 (2007) 2885-2890.
[43] B.A. Methe, K.E. Nelson, J.A. Eisen, I.T. Paulsen, W. Nelson, J.F. Heidelberg, D. Wu, M. Wu, N. Ward, M.J. Beanan, R.J. Dodson, R. Madupu, L.M. Brinkac, S.C. Daugherty, R.T. DeBoy, A.S. Durkin, M. Gwinn, J.F. Kolonay, S.A. Sullivan, D.H. Haft, J. Selengut, T.M. Davidsen, N. Zafar, O. White, B. Tran, C. Romero, H.A. Forberger, J. Weidman, H. Khouri, T.V. Feldblyum, T.R. Utterback, S.E. Van Aken, D.R. Lovley, C.M. Fraser, Genome of *Geobacter sulfurreducens*: metal reduction in subsurface environments, Science, 302 (2003) 1967-1969.
[44] G.L. Hazelbauer, J.J. Falke, J.S. Parkinson, Bacterial chemoreceptors: high-performance signaling in networked arrays, Trends Biochem Sci, 33 (2008) 9-19.

[45] C.M. Khursigara, X. Wu, P. Zhang, J. Lefman, S. Subramaniam, Role of HAMP domains in chemotaxis signaling by bacterial chemoreceptors, Proc Natl Acad Sci USA, 105 (2008) 16555-16560.
[46] I.B. Zhulin, The superfamily of chemotaxis transducers: from physiology to genomics and back, Adv Microb Physiol, 45 (2001) 157-198.
[47] K. Wuichet, R.P. Alexander, I.B. Zhulin, Comparative genomic and protein sequence analyses of a complex system controlling bacterial chemotaxis, Methods Enzymol, 422 (2007) 1-31.
[48] M. Hulko, F. Berndt, M. Gruber, J.U. Linder, V. Truffault, A. Schultz, J. Martin, J.E. Schultz, A.N. Lupas, M. Coles, The HAMP domain structure implies helix rotation in transmembrane signaling, Cell, 126 (2006) 929-940.
[49] G.S. Anand, P.N. Goudreau, A.M. Stock, Activation of methylesterase CheB: evidence of a dual role for the regulatory domain, Biochemistry, 37 (1998) 14038-14047.
[50] J.F. Hess, K. Oosawa, N. Kaplan, M.I. Simon, Phosphorylation of three proteins in the signaling pathway of bacterial chemotaxis, Cell, 53 (1988) 79-87.
[51] M.M. McEvoy, F.W. Dahlquist, Phosphohistidines in bacterial signaling, Curr Opin Struct Biol, 7 (1997) 793-797.
[52] J. Kato, T. Nakamura, A. Kuroda, H. Ohtake, Cloning and characterization of chemotaxis genes in *Pseudomonas aeruginosa*, Biosci, Biotechnol, Biochem, 63 (1999) 155-161.
[53] M.D. Manson, The tie that binds the dynamic duo: the connector between AS1 and AS2 in the HAMP domain of the *Escherichia coli* Tsr chemoreceptor, J Bacteriol, 190 (2008) 6544-6547.
[54] M. Welch, K. Oosawa, S. Aizawa, M. Eisenbach, Phosphorylation-dependent binding of a signal molecule to the flagellar switch of bacteria, Proc Natl Acad Sci USA, 90 (1993) 8787-8791.
[55] A.S. Toker, R.M. Macnab, Distinct regions of bacterial flagellar switch protein FliM interact with FliG, FliN and CheY, J Mol Biol, 273 (1997) 623-634.
[56] M.M. McEvoy, A. Bren, M. Eisenbach, F.W. Dahlquist, Identification of the binding interfaces on CheY for two of its targets, the phosphatase CheZ and the flagellar switch protein fliM, J Mol Biol, 289 (1999) 1423-1433.
[57] J. Adler, My life with nature, Annu Rev Biochem, 80 (2011) 42-70.
[58] M.Y. Galperin, Structural classification of bacterial response regulators: diversity of output domains and domain combinations, J Bacteriol, 188 (2006) 4169-4182.
[59] H. Saito, Histidine phosphorylation and two-component signaling in eukaryotic cells, Chem Rev, 101 (2001) 2497-2509.
[60] E. Martinez-Hackert, A.M. Stock, Structural relationships in the OmpR family of winged-helix transcription factors, J Mol Biol, 269 (1997) 301-312.
[61] M. Milani, L. Leoni, G. Rampioni, E. Zennaro, P. Ascenzi, M. Bolognesi, An active-like structure in the unphosphorylated StyR response regulator suggests a phosphorylation-dependent allosteric activation mechanism, Structure, 13 (2005) 1289-1297.
[62] J.D. Batchelor, M. Doucleff, C.J. Lee, K. Matsubara, S. De Carlo, J. Heideker, M.H. Lamers, J.G. Pelton, D.E. Wemmer, Structure and regulatory mechanism of *Aquifex aeolicus* NtrC4: variability and evolution in bacterial transcriptional regulation, J Mol Biol, 384 (2008) 1058-1075.
[63] D.J. Sidote, C.M. Barbieri, T. Wu, A.M. Stock, Structure of the *Staphylococcus aureus* AgrA LytTR domain bound to DNA reveals a beta fold with an unusual mode of binding, Structure, 16 (2008) 727-735.
[64] B.P. O'Hara, R.A. Norman, P.T. Wan, S.M. Roe, T.E. Barrett, R.E. Drew, L.H. Pearl, Crystal structure and induction mechanism of AmiC-AmiR: a ligand-regulated transcription antitermination complex, EMBO J, 18 (1999) 5175-5186.
[65] U. Romling, M. Gomelsky, M.Y. Galperin, C-di-GMP: the dawning of a novel bacterial signalling system, Mol Microbiol, 57 (2005) 629-639.
[66] T. Mascher, J.D. Helmann, G. Unden, Stimulus perception in bacterial signal-transducing histidine kinases, Microbiol Mol Biol Rev, 70 (2006) 910-938.
[67] B.L. Taylor, I.B. Zhulin, PAS domains: internal sensors of oxygen, redox potential, and light, Microbiol Mol Biol Rev, 63 (1999) 479-506.

[68] R.D. Finn, J. Mistry, J. Tate, P. Coggill, A. Heger, J.E. Pollington, O.L. Gavin, P. Gunasekaran, G. Ceric, K. Forslund, L. Holm, E.L. Sonnhammer, S.R. Eddy, A. Bateman, The Pfam protein families database, Nucleic Acids Res, 38 (2010) D211-222.

[69] M.H. Hefti, K.J. Francoijs, S.C. de Vries, R. Dixon, J. Vervoort, The PAS fold. A redefinition of the PAS domain based upon structural prediction, Eur J Biochem, 271 (2004) 1198-1208.

[70] P.D. Scheu, O.B. Kim, C. Griesinger, G. Unden, Sensing by the membrane-bound sensor kinase DcuS: exogenous versus endogenous sensing of C_4-dicarboxylates in bacteria, Future Microbiol, 5 (2010) 1383-1402.

[71] C. Chang, C. Tesar, M. Gu, G. Babnigg, A. Joachimiak, P.R. Pokkuluri, H. Szurmant, M. Schiffer, Extracytoplasmic PAS-like domains are common in signal transduction proteins, J Bacteriol, 192 (2010) 1156-1159.

[72] A. Moglich, R.A. Ayers, K. Moffat, Structure and signaling mechanism of Per-ARNT-Sim domains, Structure, 17 (2009) 1282-1294.

[73] J. Cheung, W.A. Hendrickson, Crystal structures of C_4-dicarboxylate ligand complexes with sensor domains of histidine kinases DcuS and DctB, J Biol Chem, 283 (2008) 30256-30265.

[74] T.D. Goddard, C.C. Huang, T.E. Ferrin, Visualizing density maps with UCSF Chimera, J Struct Biol, 157 (2007) 281-287.

[75] N. Shah, R. Gaupp, H. Moriyama, K.M. Eskridge, E.N. Moriyama, G.A. Somerville, Reductive evolution and the loss of PDC/PAS domains from the genus *Staphylococcus*, BMC Genomics, 14 (2013) 524.

[76] R.A. Ayers, K. Moffat, Changes in quaternary structure in the signaling mechanisms of PAS domains, Biochemistry, 47 (2008) 12078-12086.

[77] C.M. Dunham, E.M. Dioum, J.R. Tuckerman, G. Gonzalez, W.G. Scott, M.A. Gilles-Gonzalez, A distal arginine in oxygen-sensing heme-PAS domains is essential to ligand binding, signal transduction, and structure, Biochemistry, 42 (2003) 7701-7708.

[78] M.A. Gilles-Gonzalez, A.I. Caceres, E.H. Sousa, D.R. Tomchick, C. Brautigam, C. Gonzalez, M. Machius, A proximal arginine R206 participates in switching of the *Bradyrhizobium japonicum* FixL oxygen sensor, J Mol Biol, 360 (2006) 80-89.

[79] W. Gong, B. Hao, S.S. Mansy, G. Gonzalez, M.A. Gilles-Gonzalez, M.K. Chan, Structure of a biological oxygen sensor: a new mechanism for heme-driven signal transduction, Proc Natl Acad Sci USA, 95 (1998) 15177-15182.

[80] W. Gong, B. Hao, M.K. Chan, New mechanistic insights from structural studies of the oxygen-sensing domain of *Bradyrhizobium japonicum* FixL, Biochemistry, 39 (2000) 3955-3962.

[81] B. Hao, C. Isaza, J. Arndt, M. Soltis, M.K. Chan, Structure-based mechanism of O_2 sensing and ligand discrimination by the FixL heme domain of *Bradyrhizobium japonicum*, Biochemistry, 41 (2002) 12952-12958.

[82] J. Key, K. Moffat, Crystal structures of deoxy and CO-bound bjFixLH reveal details of ligand recognition and signaling, Biochemistry, 44 (2005) 4627-4635.

[83] J. Key, V. Srajer, R. Pahl, K. Moffat, Time-resolved crystallographic studies of the heme domain of the oxygen sensor FixL: structural dynamics of ligand rebinding and their relation to signal transduction, Biochemistry, 46 (2007) 4706-4715.

[84] H. Miyatake, M. Mukai, S.Y. Park, S. Adachi, K. Tamura, H. Nakamura, K. Nakamura, T. Tsuchiya, T. Iizuka, Y. Shiro, Sensory mechanism of oxygen sensor FixL from *Rhizobium meliloti*: crystallographic, mutagenesis and resonance Raman spectroscopic studies, J Mol Biol, 301 (2000) 415-431.

[85] M. Mullner, O. Hammel, B. Mienert, S. Schlag, E. Bill, G. Unden, A PAS domain with an oxygen labile $[4Fe\text{-}4S]^{2+}$ cluster in the oxygen sensor kinase NreB of *Staphylococcus carnosus*, Biochemistry, 47 (2008) 13921-13932.

[86] E.B. Purcell, D. Siegal-Gaskins, D.C. Rawling, A. Fiebig, S. Crosson, A photosensory two-component system regulates bacterial cell attachment, Proc Natl Acad Sci USA, 104 (2007) 18241-18246.

[87] U.E. Ukaegbu, A.C. Rosenzweig, Structure of the redox sensor domain of *Methylococcus capsulatus* (Bath) MmoS, Biochemistry, 48 (2009) 2207-2215.

[88] M. Bekker, S. Alexeeva, W. Laan, G. Sawers, J. Teixeira de Mattos, K. Hellingwerf, The ArcBA two-component system of *Escherichia coli* is regulated by the redox state of both the ubiquinone and the menaquinone pool, J Bacteriol, 192 (2010) 746-754.

[89] R. Malpica, B. Franco, C. Rodriguez, O. Kwon, D. Georgellis, Identification of a quinone-sensitive redox switch in the ArcB sensor kinase, Proc Natl Acad Sci USA, 101 (2004) 13318-13323.

[90] Y.S. Ho, L.M. Burden, J.H. Hurley, Structure of the GAF domain, a ubiquitous signaling motif and a new class of cyclic GMP receptor, EMBO J, 19 (2000) 5288-5299.

[91] X. Yang, J. Kuk, K. Moffat, Crystal structure of *Pseudomonas aeruginosa* bacteriophytochrome: photoconversion and signal transduction, Proc Natl Acad Sci USA, 105 (2008) 14715-14720.

[92] X. Yang, J. Kuk, K. Moffat, Conformational differences between the Pfr and Pr states in *Pseudomonas aeruginosa* bacteriophytochrome, Proc Natl Acad Sci USA, 106 (2009) 15639-15644.

[93] L.O. Essen, J. Mailliet, J. Hughes, The structure of a complete phytochrome sensory module in the Pr ground state, Proc Natl Acad Sci USA, 105 (2008) 14709-14714.

[94] J.R. Wagner, J. Zhang, J.S. Brunzelle, R.D. Vierstra, K.T. Forest, High resolution structure of *Deinococcus bacteriophytochrome* yields new insights into phytochrome architecture and evolution, J Biol Chem, 282 (2007) 12298-12309.

[95] X. Yang, E.A. Stojkovic, J. Kuk, K. Moffat, Crystal structure of the chromophore binding domain of an unusual bacteriophytochrome, RpBphP3, reveals residues that modulate photoconversion, Proc Natl Acad Sci USA, 104 (2007) 12571-12576.

[96] D. Albanesi, M. Martin, F. Trajtenberg, M.C. Mansilla, A. Haouz, P.M. Alzari, D. de Mendoza, A. Buschiazzo, Structural plasticity and catalysis regulation of a thermosensor histidine kinase, Proc Natl Acad Sci USA, 106 (2009) 16185-16190.

[97] M. Martin, D. Albanesi, P.M. Alzari, D. de Mendoza, Functional in vitro assembly of the integral membrane bacterial thermosensor DesK, Protein Expr Purif, 66 (2009) 39-45.

[98] G. Bogel, H. Schrempf, D. Ortiz de Orue Lucana, The heme-binding protein HbpS regulates the activity of the *Streptomyces reticuli* iron-sensing histidine kinase SenS in a redox-dependent manner, Amino Acids, 37 (2009) 681-691.

[99] J. Voet-van-Vormizeele, G. Groth, Ethylene controls autophosphorylation of the histidine kinase domain in ethylene receptor ETR1, Mol Plant, 1 (2008) 380-387.

[100] E. Geisinger, E.A. George, T.W. Muir, R.P. Novick, Identification of ligand specificity determinants in AgrC, the *Staphylococcus aureus* quorum-sensing receptor, J Biol Chem, 283 (2008) 8930-8938.

[101] R.O. Jensen, K. Winzer, S.R. Clarke, W.C. Chan, P. Williams, Differential recognition of *Staphylococcus aureus* quorum-sensing signals depends on both extracellular loops 1 and 2 of the transmembrane sensor AgrC, J Mol Biol, 381 (2008) 300-309.

[102] V.I. Gordeliy, J. Labahn, R. Moukhametzianov, R. Efremov, J. Granzin, R. Schlesinger, G. Buldt, T. Savopol, A.J. Scheidig, J.P. Klare, M. Engelhard, Molecular basis of transmembrane signalling by sensory rhodopsin II-transducer complex, Nature, 419 (2002) 484-487.

[103] M.V. Milburn, G.G. Prive, D.L. Milligan, W.G. Scott, J. Yeh, J. Jancarik, D.E. Koshland, Jr., S.H. Kim, Three-dimensional structures of the ligand-binding domain of the bacterial aspartate receptor with and without a ligand, Science, 254 (1991) 1342-1347.

[104] U.S. Cho, M.W. Bader, M.F. Amaya, M.E. Daley, R.E. Klevit, S.I. Miller, W. Xu, Metal bridges between the PhoQ sensor domain and the membrane regulate transmembrane signaling, J Mol Biol, 356 (2006) 1193-1206.

[105] M.B. Neiditch, M.J. Federle, S.T. Miller, B.L. Bassler, F.M. Hughson, Regulation of LuxPQ receptor activity by the quorum-sensing signal autoinducer-2, Mol Cell, 18 (2005) 507-518.

[106] M.B. Neiditch, M.J. Federle, A.J. Pompeani, R.C. Kelly, D.L. Swem, P.D. Jeffrey, B.L. Bassler, F.M. Hughson, Ligand-induced asymmetry in histidine sensor kinase complex regulates quorum sensing, Cell, 126 (2006) 1095-1108.

[107] S. Reinelt, E. Hofmann, T. Gerharz, M. Bott, D.R. Madden, The structure of the periplasmic ligand-binding domain of the sensor kinase CitA reveals the first extracellular PAS domain, J Biol Chem, 278 (2003) 39189-39196.

[108] L. Pappalardo, I.G. Janausch, V. Vijayan, E. Zientz, J. Junker, W. Peti, M. Zweckstetter, G. Unden, C. Griesinger, The NMR structure of the sensory domain of the membranous two-component fumarate sensor (histidine protein kinase) DcuS of *Escherichia coli*, J Biol Chem, 278 (2003) 39185-39188.

[109] J. Cheung, W.A. Hendrickson, Sensor domains of two-component regulatory systems, Curr Opin Microbiol, 13 (2010) 116-123.

[110] K. Emami, E. Topakas, T. Nagy, J. Henshaw, K.A. Jackson, K.E. Nelson, E.F. Mongodin, J.W. Murray, R.J. Lewis, H.J. Gilbert, Regulation of the xylan-degrading apparatus of *Cellvibrio japonicus* by a novel two-component system, J Biol Chem, 284 (2009) 1086-1096.

[111] Y.F. Zhou, B. Nan, J. Nan, Q. Ma, S. Panjikar, Y.H. Liang, Y. Wang, X.D. Su, C4-dicarboxylates sensing mechanism revealed by the crystal structures of DctB sensor domain, J Mol Biol, 383 (2008) 49-61.

[112] J.I. Yeh, H.P. Biemann, G.G. Prive, J. Pandit, D.E. Koshland, Jr., S.H. Kim, High-resolution structures of the ligand binding domain of the wild-type bacterial aspartate receptor, J Mol Biol, 262 (1996) 186-201.

[113] V. Anantharaman, L. Aravind, Cache - a signaling domain common to animal Ca^{2+}-channel subunits and a class of prokaryotic chemotaxis receptors, Trends Biochem Sci, 25 (2000) 535-537.

[114] H.T. Tran, J. Krushkal, F.M. Antommattei, D.R. Lovley, R.M. Weis, Comparative genomics of *Geobacter* chemotaxis genes reveals diverse signaling function, BMC Genomics, 9 (2008) 471.

[115] P.R. Pokkuluri, M. Pessanha, Y.Y. Londer, S.J. Wood, N.E. Duke, R. Wilton, T. Catarino, C.A. Salgueiro, M. Schiffer, Structures and solution properties of two novel periplasmic sensor domains with *c*-type heme from chemotaxis proteins of *Geobacter sulfurreducens*: implications for signal transduction, J Mol Biol, 377 (2008) 1498-1517.

[116] P.J. Bonner, Q. Xu, W.P. Black, Z. Li, Z. Yang, L.J. Shimkets, The Dif chemosensory pathway is directly involved in phosphatidylethanolamine sensory transduction in *Myxococcus xanthus*, Mol Microbiol, 57 (2005) 1499-1508.

[117] P.J. Bonner, W.P. Black, Z. Yang, L.J. Shimkets, FibA and PilA act cooperatively during fruiting body formation of *Myxococcus xanthus*, Mol Microbiol, 61 (2006) 1283-1293.

[118] G.H. Wadhams, J.P. Armitage, Making sense of it all: bacterial chemotaxis, Nat Rev Mol Cell Biol, 5 (2004) 1024-1037.

[119] Q. Xu, W.P. Black, S.M. Ward, Z. Yang, Nitrate-dependent activation of the Dif signaling pathway of *Myxococcus xanthus* mediated by a NarX-DifA interspecies chimera, J Bacteriol, 187 (2005) 6410-6418.

[120] M. Sevvana, V. Vijayan, M. Zweckstetter, S. Reinelt, D.R. Madden, R. Herbst-Irmer, G.M. Sheldrick, M. Bott, C. Griesinger, S. Becker, A ligand-induced switch in the periplasmic domain of sensor histidine kinase CitA, J Mol Biol, 377 (2008) 512-523.

[121] J. Cheung, W.A. Hendrickson, Structural analysis of ligand stimulation of the histidine kinase NarX, Structure, 17 (2009) 190-201.

[122] J. Cheung, M. Le-Khac, W.A. Hendrickson, Crystal structure of a histidine kinase sensor domain with similarity to periplasmic binding proteins, Proteins, 77 (2009) 235-241.

[123] J.O. Moore, W.A. Hendrickson, Structural analysis of sensor domains from the TMAO-responsive histidine kinase receptor TorS, Structure, 17 (2009) 1195-1204.

[124] S.M. Ward, A. Delgado, R.P. Gunsalus, M.D. Manson, A NarX-Tar chimera mediates repellent chemotaxis to nitrate and nitrite, Mol Microbiol, 44 (2002) 709-719.

[125] T. Yoshida, S. Phadtare, M. Inouye, The design and development of Tar-EnvZ chimeric receptors, Methods Enzymol, 423 (2007) 166-183.

[126] J. Cheung, C.A. Bingman, M. Reyngold, W.A. Hendrickson, C.D. Waldburger, Crystal structure of a functional dimer of the PhoQ sensor domain, J Biol Chem, 283 (2008) 13762-13770.

[127] S.D. Goldberg, C.S. Soto, C.D. Waldburger, W.F. Degrado, Determination of the physiological dimer interface of the PhoQ sensor domain, J Mol Biol, 379 (2008) 656-665.

[128] J. Lee, D.R. Tomchick, C.A. Brautigam, M. Machius, R. Kort, K.J. Hellingwerf, K.H. Gardner, Changes at the KinA PAS-A dimerization interface influence histidine kinase function, Biochemistry, 47 (2008) 4051-4064.
[129] J.M. Lee, H.Y. Cho, H.J. Cho, I.J. Ko, S.W. Park, H.S. Baik, J.H. Oh, C.Y. Eom, Y.M. Kim, B.S. Kang, J.I. Oh, O_2- and NO-sensing mechanism through the DevSR two-component system in *Mycobacterium smegmatis*, J Bacteriol, 190 (2008) 6795-6804.
[130] L.M. Podust, A. Ioanoviciu, P.R. Ortiz de Montellano, 2.3 A X-ray structure of the heme-bound GAF domain of sensory histidine kinase DosT of *Mycobacterium tuberculosis*, Biochemistry, 47 (2008) 12523-12531.
[131] V. Anantharaman, S. Balaji, L. Aravind, The signaling helix: a common functional theme in diverse signaling proteins, Biol Direct, 1 (2006) 25.
[132] M.A. Gilles-Gonzalez, G. Gonzalez, Signal transduction by heme-containing PAS-domain proteins, J Appl Physiol, 96 (2004) 774-783.
[133] T.A. Freitas, S. Hou, M. Alam, The diversity of globin-coupled sensors, FEBS Lett, 552 (2003) 99-104.
[134] L.M. Iyer, V. Anantharaman, L. Aravind, Ancient conserved domains shared by animal soluble guanylyl cyclases and bacterial signaling proteins, BMC Genomics, 4 (2003) 5.
[135] D. Shelver, R.L. Kerby, Y. He, G.P. Roberts, CooA, a CO-sensing transcription factor from *Rhodospirillum rubrum*, is a CO-binding heme protein, Proc Natl Acad Sci USA, 94 (1997) 11216-11220.
[136] M.A. Gilles-Gonzalez, G. Gonzalez, M.F. Perutz, L. Kiger, M.C. Marden, C. Poyart, Heme-based sensors, exemplified by the kinase FixL, are a new class of heme protein with distinctive ligand binding and autoxidation, Biochemistry, 33 (1994) 8067-8073.
[137] M.A. Gilles-Gonzalez, G.S. Ditta, D.R. Helinski, A haemoprotein with kinase activity encoded by the oxygen sensor of *Rhizobium meliloti*, Nature, 350 (1991) 170-172.
[138] V.M. Delgado-Nixon, G. Gonzalez, M.A. Gilles-Gonzalez, Dos, a heme-binding PAS protein from *Escherichia coli*, is a direct oxygen sensor, Biochemistry, 39 (2000) 2685-2691.
[139] A.L. Chang, J.R. Tuckerman, G. Gonzalez, R. Mayer, H. Weinhouse, G. Volman, D. Amikam, M. Benziman, M.A. Gilles-Gonzalez, Phosphodiesterase A1, a regulator of cellulose synthesis in *Acetobacter xylinum*, is a heme-based sensor, Biochemistry, 40 (2001) 3420-3426.
[140] E.M. Dioum, J. Rutter, J.R. Tuckerman, G. Gonzalez, M.A. Gilles-Gonzalez, S.L. McKnight, NPAS2: a gas-responsive transcription factor, Science, 298 (2002) 2385-2387.
[141] T. Tomita, G. Gonzalez, A.L. Chang, M. Ikeda-Saito, M.A. Gilles-Gonzalez, A comparative resonance Raman analysis of heme-binding PAS domains: heme iron coordination structures of the BjFixL, AxPDEA1, EcDos, and MtDos proteins, Biochemistry, 41 (2002) 4819-4826.
[142] S. Crosson, P.T. McGrath, C. Stephens, H.H. McAdams, L. Shapiro, Conserved modular design of an oxygen sensory/signaling network with species-specific output, Proc Natl Acad Sci USA, 102 (2005) 8018-8023.
[143] M. David, M.L. Daveran, J. Batut, A. Dedieu, O. Domergue, J. Ghai, C. Hertig, P. Boistard, D. Kahn, Cascade regulation of nif gene expression in *Rhizobium meliloti*, Cell, 54 (1988) 671-683.
[144] H.M. Fischer, Genetic regulation of nitrogen fixation in rhizobia, Microbiol Rev, 58 (1994) 352-386.
[145] F.E. Rey, C.S. Harwood, FixK, a global regulator of microaerobic growth, controls photosynthesis in *Rhodopseudomonas palustris*, Mol Microbiol, 75 (2010) 1007-1020.
[146] A. Tanaka, H. Takahashi, T. Shimizu, Critical role of the heme axial ligand, Met^{95}, in locking catalysis of the phosphodiesterase from *Escherichia coli* (Ec DOS) toward Cyclic diGMP, J Biol Chem, 282 (2007) 21301-21307.
[147] J.R. Tuckerman, G. Gonzalez, E.H. Sousa, X. Wan, J.A. Saito, M. Alam, M.A. Gilles-Gonzalez, An oxygen-sensing diguanylate cyclase and phosphodiesterase couple for c-di-GMP control, Biochemistry, 48 (2009) 9764-9774.
[148] H.Y. Cho, H.J. Cho, Y.M. Kim, J.I. Oh, B.S. Kang, Structural insight into the heme-based redox sensing by DosS from *Mycobacterium tuberculosis*, J Biol Chem, 284 (2009) 13057-13067.

[149] S. Yoshioka, K. Kobayashi, H. Yoshimura, T. Uchida, T. Kitagawa, S. Aono, Biophysical properties of a *c*-type heme in chemotaxis signal transducer protein DcrA, Biochemistry, 44 (2005) 15406-15413.
[150] Y.Y. Londer, I.S. Dementieva, C.A. D'Ausilio, P.R. Pokkuluri, M. Schiffer, Characterization of a *c*-type heme-containing PAS sensor domain from *Geobacter sulfurreducens* representing a novel family of periplasmic sensors in *Geobacteraceae* and other bacteria, FEMS Microbiol Lett, 258 (2006) 173-181.
[151] D.R. Lovley, D.E. Holmes, K.P. Nevin, Dissimilatory Fe(III) and Mn(IV) reduction, Adv Microb Physiol, 49 (2004) 219-286.
[152] K.P. Nevin, B.C. Kim, R.H. Glaven, J.P. Johnson, T.L. Woodard, B.A. Methe, R.J. Didonato, S.F. Covalla, A.E. Franks, A. Liu, D.R. Lovley, Anode biofilm transcriptomics reveals outer surface components essential for high density current production in *Geobacter sulfurreducens* fuel cells, PLoS One, 4 (2009) e5628.
[153] D.R. Lovley, Bug juice: harvesting electricity with microorganisms, Nat Rev Microbiol, 4 (2006) 497-508.
[154] D.R. Lovley, Cleaning up with genomics: applying molecular biology to bioremediation, Nat Rev Microbiol, 1 (2003) 35-44.
[155] D.R. Lovley, T. Ueki, T. Zhang, N.S. Malvankar, P.M. Shrestha, K.A. Flanagan, M. Aklujkar, J.E. Butler, L. Giloteaux, A.E. Rotaru, D.E. Holmes, A.E. Franks, R. Orellana, C. Risso, K.P. Nevin, *Geobacter*: the microbe electric's physiology, ecology, and practical applications, Adv Microb Physiol, 59 (2011) 1-100.
[156] D.K. Newman, R. Kolter, A role for excreted quinones in extracellular electron transfer, Nature, 405 (2000) 94-97.
[157] G. Reguera, K.D. McCarthy, T. Mehta, J.S. Nicoll, M.T. Tuominen, D.R. Lovley, Extracellular electron transfer via microbial nanowires, Nature, 435 (2005) 1098-1101.
[158] S.E. Childers, S. Ciufo, D.R. Lovley, *Geobacter metallireducens* accesses insoluble Fe(III) oxide by chemotaxis, Nature, 416 (2002) 767-769.
[159] Y.A. Gorby, S. Yanina, J.S. McLean, K.M. Rosso, D. Moyles, A. Dohnalkova, T.J. Beveridge, I.S. Chang, B.H. Kim, K.S. Kim, D.E. Culley, S.B. Reed, M.F. Romine, D.A. Saffarini, E.A. Hill, L. Shi, D.A. Elias, D.W. Kennedy, G. Pinchuk, K. Watanabe, S. Ishii, B. Logan, K.H. Nealson, J.K. Fredrickson, Electrically conductive bacterial nanowires produced by *Shewanella oneidensis* strain MR-1 and other microorganisms, Proc Natl Acad Sci USA, 103 (2006) 11358-11363.
[160] K.P. Nevin, T.L. Woodard, A.E. Franks, Z.M. Summers, D.R. Lovley, Microbial electrosynthesis: feeding microbes electricity to convert carbon dioxide and water to multicarbon extracellular organic compounds, MBio, 1 (2010) e00103-10.
[161] D.R. Lovley, Powering microbes with electricity: direct electron transfer from electrodes to microbes, Environ Microbiol Rep, 3 (2011) 27-35.
[162] D.R. Lovley, K.P. Nevin, A shift in the current: new applications and concepts for microbe-electrode electron exchange, Curr Opin Biotechnol, 22 (2011) 441-448.
[163] J. Yun, T. Ueki, M. Miletto, D.R. Lovley, Monitoring the metabolic status of *Geobacter* species in contaminated groundwater by quantifying key metabolic proteins with *Geobacter*-specific antibodies, Appl Environ Microbiol, 77 (2011) 4597-4602.
[164] J. Zhao, Y. Fang, T.D. Scheibe, D.R. Lovley, R. Mahadevan, Modeling and sensitivity analysis of electron capacitance for *Geobacter* in sedimentary environments, J Contam Hydrol, 112 (2010) 30-44.
[165] M.V. Coppi, C. Leang, S.J. Sandler, D.R. Lovley, Development of a genetic system for *Geobacter sulfurreducens*, Appl Environ Microbiol, 67 (2001) 3180-3187.
[166] S.F. Altschul, T.L. Madden, A.A. Schaffer, J. Zhang, Z. Zhang, W. Miller, D.J. Lipman, Gapped BLAST and PSI-BLAST: a new generation of protein database search programs, Nucleic Acids Res, 25 (1997) 3389-3402.
[167] L.A. Kelley, M.J. Sternberg, Protein structure prediction on the Web: a case study using the Phyre server, Nat Protoc, 4 (2009) 363-371.
[168] T. Catarino, M. Pessanha, A.G. De Candia, Z. Gouveia, A.P. Fernandes, P.R. Pokkuluri, D. Murgida, M.A. Marti, S. Todorovic, C.A. Salgueiro, Probing the chemotaxis periplasmic sensor domains from *Geobacter sulfurreducens* by combined resonance Raman and

molecular dynamic approaches: NO and CO sensing, J Phys Chem B, 114 (2010) 11251-11260.
[169] J. Mao, K. Hauser, M.R. Gunner, How cytochromes with different folds control heme redox potentials, Biochemistry, 42 (2003) 9829-9840.
[170] D.W. Urry, Free energy transduction in polypeptides and proteins based on inverse temperature transitions, Prog Biophys Mol Biol, 57 (1992) 23-57.
[171] B. Li, D.O. Alonso, V. Daggett, The molecular basis for the inverse temperature transition of elastin, J Mol Biol, 305 (2001) 581-592.
[172] B. Li, V. Daggett, The molecular basis of the temperature- and pH-induced conformational transitions in elastin-based peptides, Biopolymers, 68 (2003) 121-129.
[173] D.W. Urry, T.L. Trapane, K.U. Prasad, Phase-structure transitions of the elastin polypentapeptide-water system within the framework of composition-temperature studies, Biopolymers, 24 (1985) 2345-2356.
[174] A.P. Fernandes, I. Couto, L. Morgado, Y.Y. Londer, C.A. Salgueiro, Isotopic labeling of *c*-type multiheme cytochromes overexpressed in *E. coli*, Protein Expr Purif, 59 (2008) 182-188.
[175] G.P. Moss, Nomenclature of tetrapyrroles. Recommendations 1986 IUPAC-IUB Joint Commission on Biochemical Nomenclature (JCBN), Eur J Biochem, 178 (1988) 277-328.
[176] A.K. Dunker, I. Silman, V.N. Uversky, J.L. Sussman, Function and structure of inherently disordered proteins, Curr Opin Struct Biol, 18 (2008) 756-764.
[177] D.L. Turner, C.A. Salgueiro, J. LeGall, A.V. Xavier, Structural studies of *Desulfovibrio vulgaris* ferrocytochrome c_3 by two-dimensional NMR, Eur J Biochem, 210 (1992) 931-936.
[178] G.S. Rule, T.K. Hitchens, Fundamentals of protein NMR spectroscopy, Springer, Netherlands, 2006.
[179] K. Wuthrich, NMR of proteins and nucleic acids, John Wiley & Son, New York, 1986.
[180] E.D. Becker, High Resolution NMR - Theory and Chemical Applications, Academic Press, New York, 2000.
[181] P. Atkins, J. Paula, Atkins' Physical Chemistry, Oxford University Press, Oxford, 2014.
[182] D.S. Wishart, C.G. Bigam, J. Yao, F. Abildgaard, H.J. Dyson, E. Oldfield, J.L. Markley, B.D. Sykes, ^{1}H, ^{13}C and ^{15}N chemical shift referencing in biomolecular NMR, J Biomol NMR, 6 (1995) 135-140.
[183] T.D. Goddard, D.G. Kneller, Sparky 3.114, In: University of California, San Francisco, 2007.
[184] R.M. Keller, K. Wüthrich, Assignment of the heme *c* resonances in the 360 MHz H NMR spectra of cytochrome *c*, Biochim Biophys Acta, 533 (1978) 195-208.
[185] M.Y. Galperin, A census of membrane-bound and intracellular signal transduction proteins in bacteria: bacterial IQ, extroverts and introverts, BMC Microbiol, 5 (2005) 35.
[186] M.K. Chan, Recent advances in heme-protein sensors, Curr Opin Chem Biol, 5 (2001) 216-222.
[187] S. Aono, Biochemical and biophysical properties of the CO-sensing transcriptional activator CooA, Acc Chem Res, 36 (2003) 825-831.
[188] G.P. Roberts, M.V. Thorsteinsson, R.L. Kerby, W.N. Lanzilotta, T. Poulos, CooA: a heme-containing regulatory protein that serves as a specific sensor of both carbon monoxide and redox state, Prog Nucleic Acid Res Mol Biol, 67 (2001) 35-63.
[189] K.R. Rodgers, Heme-based sensors in biological systems, Curr Opin Chem Biol, 3 (1999) 158-167.
[190] R. Fu, J.D. Wall, G. Voordouw, DcrA, a *c*-type heme-containing methyl-accepting protein from *Desulfovibrio vulgaris* Hildenborough, senses the oxygen concentration or redox potential of the environment, J Bacteriol, 176 (1994) 344-350.
[191] M.A. Gilles-Gonzalez, G. Gonzalez, Heme-based sensors: defining characteristics, recent developments, and regulatory hypotheses, J Inorg Biochem, 99 (2005) 1-22.
[192] S.M. Kelly, N.C. Price, Circular Dichroism: Studies of Proteins, In: Encyclopedia of Life, John Wiley & Sons, 2009.
[193] S.M. Kelly, T.J. Jess, N.C. Price, How to study proteins by circular dichroism, Biochim Biophys Acta, 1751 (2005) 119-139.
[194] N.J. Greenfield, Using circular dichroism spectra to estimate protein secondary structure, Nat Protoc, 1 (2006) 2876-2890.

[195] N. Berova, K. Nakanishi, R.W. Woody, Circular Dichroism: Principles and Applications, Wiley-VCH, New York, 2000.
[196] G. Holzwarth, P. Doty, The ultraviolet circular dichroism of polypeptides, J Am Chem Soc, 87 (1965) 218-228.
[197] N. Greenfield, G.D. Fasman, Computed circular dichroism spectra for the evaluation of protein conformation, Biochemistry, 8 (1969) 4108-4116.
[198] S. Venyaminov, I.A. Baikalov, Z.M. Shen, C.S. Wu, J.T. Yang, Circular dichroic analysis of denatured proteins: inclusion of denatured proteins in the reference set, Anal Biochem, 214 (1993) 17-24.
[199] F.A. Bovey, F.P. Hood, The circular dichroism spectrum of poly-L-acetoxyproline, Biopolymers, 5 (1967) 915-919.
[200] Z. Obradovic, K. Peng, S. Vucetic, P. Radivojac, C.J. Brown, A.K. Dunker, Predicting intrinsic disorder from amino acid sequence, Proteins, 53 (2003) 566-572.
[201] C.N. Pace, Determination and analysis of urea and guanidine hydrochloride denaturation curves, Methods Enzymol, 131 (1986) 266-280.
[202] J.K. Myers, C.N. Pace, J.M. Scholtz, Denaturant *m* values and heat capacity changes: relation to changes in accessible surface areas of protein unfolding, Protein Sci, 4 (1995) 2138-48.
[203] C.N. Pace, D.V. Laurents, J.A. Thomson, pH dependence of the urea and guanidine hydrochloride denaturation of ribonuclease A and ribonuclease T1, Biochemistry, 29 (1990) 2564-72.
[204] G. Tsaprailis, D.W. Chan, A.M. English, Conformational states in denaturants of cytochrome *c* and horseradish peroxidases examined by fluorescence and circular dichroism, Biochemistry, 37 (1998) 2004-2016.
[205] C.M. Gomes, A. Faria, J.C. Carita, J. Mendes, M. Regalla, P. Chicau, H. Huber, K.O. Stetter, M. Teixeira, Di-cluster, seven-iron ferredoxins from hyperthermophilic *Sulfolobales*, J Biol Inorg Chem, 3 (1998) 499-507.
[206] S.S. Leal, M. Teixeira, C.M. Gomes, Studies on the degradation pathway of iron-sulfur centers during unfolding of a hyperstable ferredoxin: cluster dissociation, iron release and protein stability, J Biol Inorg Chem, 9 (2004) 987-996.
[207] B. Boscolo, S.S. Leal, E.M. Ghibaudi, C.M. Gomes, Lactoperoxidase folding and catalysis relies on the stabilization of the alpha-helix rich core domain: a thermal unfolding study, Biochim Biophys Acta, 1774 (2007) 1164-1172.
[208] B. Boscolo, S.S. Leal, C.A. Salgueiro, E.M. Ghibaudi, C.M. Gomes, The prominent conformational plasticity of lactoperoxidase: a chemical and pH stability analysis, Biochim Biophys Acta, 1794 (2009) 1041-1048.
[209] S.S. Leal, C.M. Gomes, Iron-sulfur clusters, protein folds, and ferredoxin stability, In: Protein folding and metal ions: mechanisms, biology and disease, C.M. Gomes, P. Wittung-Stafshede, CRC Press, Florida, 2010.
[210] M. Brunori, M.G. Bigotti, F. Cutruzzola, S. Gianni, C. Travaglini-Allocatelli, Cytochrome c_{551} as a model system for protein folding, Biophys Chem, 100 (2003) 409-419.
[211] S.K. Grant, I.C. Deckman, J.S. Culp, M.D. Minnich, I.S. Brooks, P. Hensley, C. Debouck, T.D. Meek, Use of protein unfolding studies to determine the conformational and dimeric stabilities of HIV-1 and SIV proteases, Biochemistry, 31 (1992) 9491-9501.
[212] P.L. Ferguson, G.S. Shaw, Role of the N-terminal helix I for dimerization and stability of the calcium-binding protein S100B, Biochemistry, 41 (2002) 3637-3646.
[213] S. Kumar, C.J. Tsai, R. Nussinov, Factors enhancing protein thermostability, Protein Eng, 13 (2000) 179-191.
[214] W. Pfeil, U. Gesierich, G.R. Kleemann, R. Sterner, Ferredoxin from the hyperthermophile *Thermotoga maritima* is stable beyond the boiling point of water, J Mol Biol, 272 (1997) 591-596.
[215] A. Chakrabartty, T. Kortemme, R.L. Baldwin RL, Helix propensities of the amino acids measured in alanine-based peptides without helix-stabilizing side-chain interactions, Protein Sci, 3 (1994) 843-52.
[216] A. Chakrabartty, J.A. Schellman, R.L. Baldwin, Large differences in the helix propensities of alanine and glycine, Nature, 351 (1991) 586-8.

[217] M. Etzkorn, H. Kneuper, P. Dunnwald, V. Vijayan, J. Kramer, C. Griesinger, S. Becker, G. Unden, M. Baldus, Plasticity of the PAS domain and a potential role for signal transduction in the histidine kinase DcuS, Nat Struct Mol Biol, 15 (2008) 1031-1039.
[218] P. Tompa, A. Fersht, Structure and function of intrinsically disordered proteins, CRC Press, Boca Raton, 2010.
[219] E.M. Boon, M.A. Marletta, Ligand discrimination in soluble guanylate cyclase and the H-NOX family of heme sensor proteins, Curr Opin Chem Biol, 9 (2005) 441-446.
[220] Y. Sasakura, T. Yoshimura-Suzuki, H. Kurokawa, T. Shimizu, Structure-function relationships of EcDOS, a heme-regulated phosphodiesterase from *Escherichia coli*, Acc Chem Res, 39 (2006) 37-43.
[221] S. Aono, Metal-containing sensor proteins sensing diatomic gas molecules, Dalton Trans, (2008) 3137-3146.
[222] G.P. Roberts, R.L. Kerby, H. Youn, M. Conrad, CooA, a paradigm for gas sensing regulatory proteins, J Inorg Biochem, 99 (2005) 280-292.
[223] D.R. Lovley, Environmental Microbe-Metal Interactions, ASM Press, Washington, D.C., 2000.
[224] C.A. Salgueiro, L. Morgado, B. Fonseca, P. Lamosa, T. Catarino, D.L. Turner, R.O. Louro, Binding of ligands originates small perturbations on the microscopic thermodynamic properties of a multicentre redox protein, FEBS J, 272 (2005) 2251-2260.
[225] R.O. Louro, T. Catarino, J. LeGall, D.L. Turner, A.V. Xavier, Cooperativity between electrons and protons in a monomeric cytochrome c_3: the importance of mechano-chemical coupling for energy transduction, ChemBiochem, 2 (2001) 831-837.
[226] M. Pessanha, L. Morgado, R.O. Louro, Y.Y. Londer, P.R. Pokkuluri, M. Schiffer, C.A. Salgueiro, Thermodynamic characterization of triheme cytochrome PpcA from *Geobacter sulfurreducens*: Evidence for a role played in e^-/H^+ energy transduction, Biochemistry, 45 (2006) 13910-13917.
[227] M. Pessanha, Y.Y. Londer, W.C. Long, J. Erickson, P.R. Pokkuluri, M. Schiffer, C.A. Salgueiro, Redox characterization of *Geobacter sulfurreducens* cytochrome c_7: Physiological relevance of the conserved residue F15 probed by site-specific mutagenesis, Biochemistry, 43 (2004) 9909-9917.
[228] P.O. Quintas, A.P. Cepeda, N. Borges, T. Catarino, D.L. Turner, Relative importance of driving force and electrostatic interactions in the reduction of multihaem cytochromes by
[229] R.J. Balahura, J. M.D., Outer-sphere dithionite reductions of metal complexes, Inorg Chem, 26 (1987) 3860-3863.
[230] M. Dixon, The acceptor specificity of flavins and flavoproteins. I. Techniques for anaerobic spectrophotometry, Biochim Biophys Acta, 226 (1971) 241-258.
[231] D.O. Lambeth, G. Palmer, The kinetics and mechanism of reduction of electron transfer proteins and other compounds of biological interest by dithionite, J Biol Chem, 248 (1973) 6095-6103.
[232] R.N. Thorneley, D.J. Lowe, Nitrogenase of *Klebsiella pneumoniae*. Kinetics of the dissociation of oxidized iron protein from molybdenum-iron protein: identification of the rate-limiting step for substrate reduction, Biochem J, 215 (1983) 393-403.
[233] S. Wherland, H.B. Gray, Metalloprotein electron transfer reactions: analysis of reactivity of horse heart cytochrome *c* with inorganic complexes, Proc Natl Acad Sc USA, 73 (1976) 2950-2954.
[234] F. Caccavo, Jr., D.J. Lonergan, D.R. Lovley, M. Davis, J.F. Stolz, M.J. McInerney, *Geobacter sulfurreducens* sp. nov., a hydrogen- and acetate-oxidizing dissimilatory metal-reducing microorganism, Appl Environ Microbiol, 60 (1994) 3752-3759.
[235] D.R. Lovley, Dissimilatory metal reduction, Annu Rev Microbiol, 47 (1993) 263-290.
[236] D.R. Lovley, D.E. Holmes, K.P. Nevin, Dissimilatory Fe(III) and Mn(IV) reduction, Adv Microb Physiol, 49 (2004) 219-286.
[237] D.R. Lovley, E.J.P. Phillips, Y.A. Gorby, E.R. Landa, Microbial reduction of uranium, Nature, 350 (1991) 413-416.
[238] D.R. Lovley, M.J. Baedecker, D.J. Lonergan, I.M. Cozzarelli, E.J.P. Phillips, D.I. Siegel, Oxidation of aromatic contaminants coupled to microbial iron reduction, Nature, 339 (1989) 297 - 300

[239] P.L. Dutton, Redox potentiometry: determination of midpoint potentials of oxidation-reduction components of biological electron-transfer systems, Methods Enzymol, 54 (1978) 411-435.
[240] P. Neta, R.E. Huie, A. Harriman, One-electron-transfer reactions of the couple SO_2/SO_2^- in aqueous solutions. Pulse radiolytic and cyclic voltammetric studies, J Phys Chem, 91 (1987) 1606-1611.
[241] R.A. Marcus, N. Sutin, Electron transfers in chemistry and biology, Biochimi Biophys Acta, 811 (1985) 265-322.
[242] M. Sulpizi, S. Raugei, J. VandeVondele, P. Carloni, M. Sprik, Calculation of redox properties: understanding short- and long-range effects in rubredoxin, J Phys Chem B, 111 (2007) 3969-3976.
[243] M.A. Silva, T.G. Lucas, C.A. Salgueiro, C.M. Gomes, Protein folding modulates the swapped dimerization mechanism of methyl-accepting chemotaxis heme sensors, PLoS One, 7 (2012) e46328.
[244] R. Koradi, M. Billeter, K. Wuthrich, MOLMOL: a program for display and analysis of macromolecular structures, J Mol Graph 14 (1996) 51–55, 29–32.
[245] C.M. Paquete, D.L. Turner, R.O. Louro, A.V. Xavier, T. Catarino, Thermodynamic and kinetic characterisation of individual haems in multicentre cytochromes c_3, Biochim Biophys Acta, 1767 (2007) 1169-1179.
[246] B. Lee, F.M. Richards, The interpretation of protein structures: estimation of static accessibility, J Mol Biol, 55 (1971) 379-400.
[247] E. Marsili, J.B. Rollefson, D.B. Baron, R.M. Hozalski, D.R. Bond, Microbial biofilm voltammetry: direct electrochemical characterization of catalytic electrode-attached biofilms, Appl Environ Microbiol, 74 (2008) 7329-7337.
[248] E. Marsili, J. Sun, D.R. Bond, Voltammetry and growth physiology of *Geobacter sulfurreducens* biofilms as a function of growth stage and imposed electrode potential, Electroanal, 22 (2010) 865-874.
[249] J.S. Parkinson, Bacterial chemotaxis: a new player in response regulator dephosphorylation, J Bacteriol, 185 (2003) 1492-1494.
[250] L.K. Keefer, R.W. Nims, K.M. Davies, D.A. Wink, "NONOates" (1-substituted diazen-1-ium-1,2-diolates) as nitric oxide donors: convenient nitric oxide dosage forms, Methods Enzymol, 268 (1996) 281-293.
[251] W.R. Taylor, The classification of amino acid conservation, J Theor Biol, 119 (1986) 205-218.

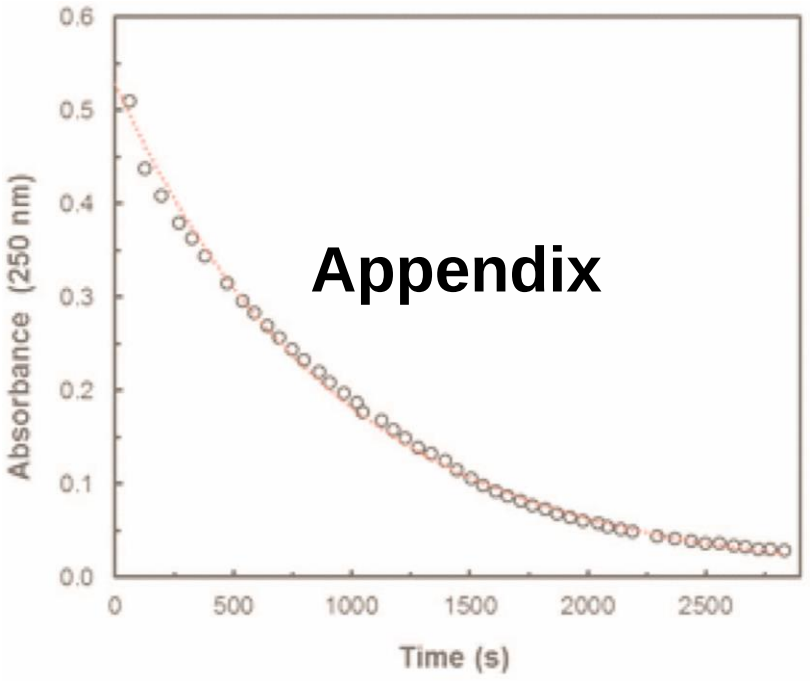
Absorbance (250 nm)
0.0
0.1
0.2
0.3
0.4
0.5
0.6
0
500
1000
1500
2000
2500
Time (s)

Appendix

A. APPENDIX

A.1 Mutated forms of GSU0582 and GSU0935 sensor domains

A.1.1 Selection of the mutants and site-directed mutagenesis

The Venn diagram describe by Taylor W.R. [251] and illustrated in Figure A.1 was used to select the mutations of the sensor domains GSU0582 and GSU0935.

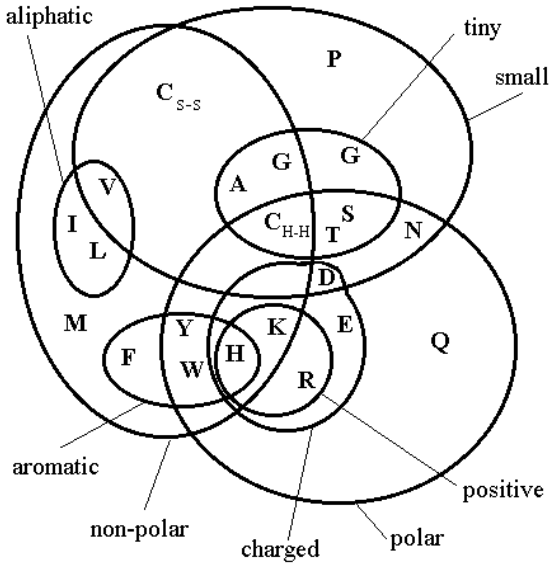

Figure A.1 – Venn diagram showing the relationship of the 20 naturally occurring amino acids to a selection of physio-chemical properties thought to be important in the determination of protein structure. Reproduced from [251].

The QuikChange Site-Directed Mutagenesis kit (Stratagene) was used to prepare the sensor domain mutants with the primers shown in Table A.1.

Table A.1 – **Primers used for site-directed mutagenesis to prepare the sensor domains mutants.** Capital letters highlight the mutated base pairs.

	GSU0582		GSU0935	
Mutant	**Forward primer sequence (5'->3')**	**Reverse primer sequence (5'->3')**	**Forward primer sequence (5'->3')**	**Reverse primer sequence (5'->3')**
Met^{60}A	tgacatcggcgaactcG Cgatggcgggtgacatg	catgtcacccgccatcG Cgagttcgccgatgtca	cacgacattgacggctatG Cgatgaagggcgactcct	aggagtcgcccttcatcGC atagccgtcaatgtcgtg
Asp^{57}Lys	-	-	cgggctcatcattcacgacat tAaGggctatatgatgaag	cttcatcatatagccCtTaat gtcgtgaatgatgagcccg
Asp^{57}Asn	-	-	ccgggctcatcattcacgac attaAcggctatatga	tcatatagccgtTaatgtcgt gaatgatgagcccgg
Glu^{89}Lys	-	-	ctcagggttttcgacAagca ggccaaagagg	cctctttggcctgctTgtcga aaaccctgag
Glu^{89}Gln	-	-	ctcagggttttcgacCagca ggccaaagagg	cctctttggcctgctGgtcga aaaccctgag

The GSU0935 double mutants Asp^{57}Lys/Glu^{89}Lys, Asp^{57}Lys/Glu^{89}Gln, Asp^{57}Ans/Glu^{89}Lys and Asp^{57}Asn/Glu^{89}Gln were prepared with the primers indicated in the Table A.1.

A.1.2 Heterologous expression and purification

The methodology used to express and purify the sensor domain mutants was the same described for the native proteins in the Chapter 2.

A.1.3 Equilibrium unfolding experiments

The conformational stability of the mutantes obtained was assessed by performing temperature denaturations, monitored by far-UV CD at 222 nm, which reports on the stability of the secondary structural elements (α-helices and β-sheets). Protein solutions (0.2 mg.mL^{-1}) were prepared in a 20 mM sodium phosphate buffer at pH 8.0. For thermal-induced denaturation, a heating rate of 1.0 ºC.min^{-1} was used, and temperature was increased from 10 ºC to 90 ºC.

A.1.4 Determination of reduction potentials

The redox titrations of the mutant sensor domain GSU0935 followed by visible spectroscopy in the 100 mM Tris-maleto pH 8.0 are shown in Figure 6.2.

A.2 Kinetic characterization of the nitric oxide binding to the GSU0582 and GSU0935 sensor domains from G. sulfurreducens

Stopped-flow kinetic experiments were performed at constant temperature of 20 °C using a SF-61 DX2 stopped-flow apparatus (Hi-Tech Scientific) placed inside an anaerobic chamber (< 2 ppm of O_2). To reduce the proteins, sodium dithionite was used with precausion to minimize its excess because it may react with the NO releasing compound or NO itself. The protein samples were prepared in 20 mM sodium phosphate buffer, 100 mM NaCl (pH 7.6) at final concentration of 9 μM. NO solutions were prepared by adding concentrated NONOate in 10 mM NaOH, to the same buffer as the protein in 6 mL flasks with no head-space. The solutions were then left for at least one hour so that the NO was fully released, resulting in known final NO concentrations in the range 3.5 μM to 295 μM. At this pH, each NONOate molecule releases 1.5 molecules of NO. The amount of NO present in solution at each time was obtained by monitoring the decay of the NONOate peak under the same conditions (ε_{250} = 6.5 $mM^{-1}cm^{-1}$) [250].

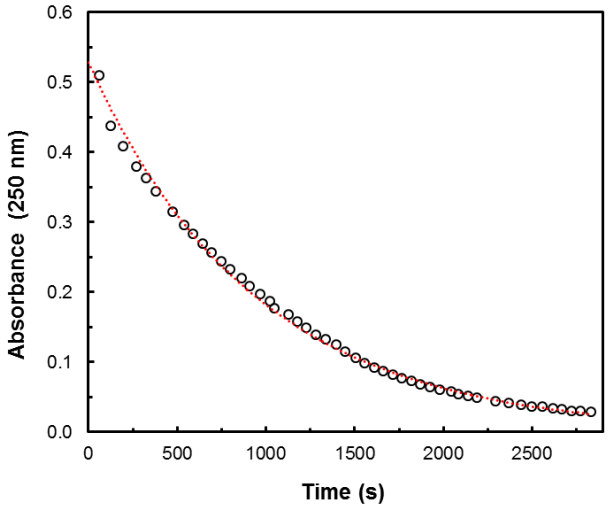

Figure A.2 – NONOate peak decay. The red line represents the data fitted with one exponential. After 45 min was observed that the NONOate peak height was reduced and the release of NO completed [250].

Solutions of both proteins and NO were mixed and the variation in absorbance in the UV-visible was followed. The reaction was followed by irradiating the sample with light from a xenon lamp and detecting the transmitted light with a photodiode array (512 diodes, 350-700 nm range). All reactions were performed under pseudo-first order conditions ([NO] >> [protein]) and traces were fitted with exponentials, or biexponentials when two processes were observed. Second order rate constants were obtained by measuring pseudo-first order rate constants as a function of [NO].